ABSTRACT

Title of Document:	DIFFUSION KURTOSIS MAGNETIC RESONANCE IMAGING AND ITS APPLICATION TO TRAUMATIC BRAIN INJURY
	Jiachen Zhuo, Doctor of Philosophy, 2011
Directed By:	Professor Jonathan Z. Simon Department of Electrical and Computer Engineering

Diffusion tensor imaging (DTI) is a popular magnetic resonance imaging technique that provides *in vivo* information about tissue microstructure, based on the local water diffusion environment. DTI models the diffusion displacement of water molecules in tissue as a Gaussian distribution. In this dissertation, to mimic the complex nature of water diffusion in brain tissues, a diffusion kurtosis model is used, to incorporate important non-Gaussian diffusion properties. This diffusion kurtosis imaging (DKI) is applied in an experimental traumatic brain injury in a rat model, to study whether it provides more information on microstructural changes than standard DTI. Our results indicate changes in ordinary DTI parameters, in various brain regions following injury, normalize to the baseline by the sub-acute stage. However, DKI parameters continue to show abnormalities at this sub-acute stage, as confirmed by immunohistochemical examination. Specifically, increased mean kurtosis (*MK*) was found to associate with increased reactive astrogliosis, a hallmark for

inflammation, even in regions far removed from the injury foci. Findings suggest that monitoring changes in *MK* enhances the investigation of molecular and morphological changes *in vivo*.

Extending DKI to clinical usage, however, poses several challenges: (a) long image acquisition time (~20 min) due to the augmented measurements required to fit the more complex model, (b) slow image reconstruction (~90 min) due to required nonlinear fitting and, (c) errors associated with fitting the inherently low signal-to-noise ratio (SNR) images from higher diffusion weighting. The second portion of this dissertation is devoted to developing imaging schemes and image reconstruction methods that facilitate clinical DKI applications. A fast and efficient DKI reconstruction method is developed with a reconstruction time of 2-3 seconds, with improved accuracy and reduced variability in DKI estimation over conventional methods. Further analysis of diffusion weighted imaging schemes and their affect on DKI estimation leads to the identification of two clinically practical optimal imaging schemes (needing 7-10 min) that perform comparably to traditional schemes. The effect of SNR and reconstruction methods on DKI estimation is also studied, to provide a foundation for interpreting DKI results and optimizing DKI protocols.

DIFFUSION KURTOSIS MAGNETIC RESONANCE IMAGING AND ITS APPLICATION TO TRAUMATIC BRAIN INJURY

By

Jiachen Zhuo

Dissertation submitted to the Faculty of the Graduate School of the
University of Maryland, College Park, in partial fulfillment
of the requirements for the degree of
Doctor of Philosophy
2011

Advisory Committee:
Professor Jonathan Z. Simon, Chair
Professor Rao P. Gullapalli, Co-chair
Professor Pamela A. Abshire
Professor Carol Y. Espy-Wilson
Professor Reuben S. Mezrich
Professor Benjamin Shapiro, Dean’s Representative

Dedication

To my family for their unconditional love and support.

Acknowledgements

I owe my sincere gratitude to all the people who have made this dissertation possible and my graduate school experience a cherishable one.

First of all, I would like to thank my advisor Professor Jonanthan Z. Simon for giving me the opportunity to pursue my Ph.D under his guidance. I have learned so much from him, from how to do good research, how to multi-task, how to write well, to how to balance work and life. He has always been patient and has always had faith in me, even during the time when I was hardly making any progress. His dedication to research and students will always be a great source of inspiration and motivation for me throughout the rest of my career.

I am deeply in debt to my co-advisor also my supervisor at work, Professor Rao P. Gullapalli of the Dept. of Radiology at the University of Maryland School of Medicine, for providing me with great opportunities to work on really interesting research topics, as well as offering valuable guidance for reaching fruitful results. Throughout the long journey of pursuing my doctorate degree while working, Dr. Gullapalli has always been extremely supportive, from providing me flexible working hours, to getting me involved with projects that may benefit my doctorate research. Thanks to him for all the encouragement and the strong belief in me that has uncovered my greater potential and has kept me moving forward toward a higher level.

I would also like to thank Professor Reuben Mezrich of the Dept. of Radiology at the University of Maryland School of Medicine, for his strong support and continuing encouragement for me to pursue a doctorate degree. As the former chairman of a clinical department, his continuing interest and dedication to research, and all his effort to support research has made a difference for researchers in the department. His own life experience, being persistent, always ready to take on new challenges, and continuously pursing higher career goals has also been a great inspiration to me.

Many thanks to all my other committee members. Thanks to Professor Christopher Davis and Professor Carol Espy-Wilson for their helpful comments and stimulating discussions about my dissertation. Thanks to Professor Benjamin Shapiro for being willing to make time to be my Dean's Representative. Thanks to Professor Pamela Abshire who graciously agreed to be on my committee on a very short notice.

I would also like to thank my previous master's research advisor, Professor Fernando E. Boada, at the MR Research Center at the University of Pittsburgh, who introduced me to the fascinating magnetic resonance imaging research field and equipped me with a solid imaging background. Thanks to my master's academic advisor, Professor Ching-Chung Li, in the Dept. of Electrical Engineering at the University of Pittsburgh, who has always encouraged me in pursuing a doctorate degree.

Special thanks to all my colleagues in the MR Research Center at the University of Maryland School of Medicine, who have made my work environment such a pleasant one. Thanks to Professor Su Xu, Da shi and Jake Mullins for all the help with animal imaging, animal preparation, tissue histology and all the helpful and intriguing discussions. Thanks to Professor Alan McMillan, Steven Roys, George Makris, Kim Taylor for all the help with imaging, data analysis, computers, networks, paper works ... everything. Thanks to all the students in our lab, Josh Betz, Chandler Sours, Albert Kir and George Elijah, who provided me with some great ideas through insightful discussion.

Many thanks to my fellow graduate students in Dr. Simon's Computational Sensorimotor Systems Lab, Nai Ding, Dan Hertz, Kai Sum Li and Juanjuan Xiang, who are always willing to help. Among them, I especially want to thank Nai for tons of help as an "insider" at school for these many years.

I would also like to thank many collaborators across the campus who have helped and supported me all along. Thanks to Professor Gary Fiskum, Jennifer Racz and Julie Proctor at the Dept. of Anesthesiology and the Center for Shock Trauma and Anesthesiology Research for providing us with well-controlled injured animals and tissue histology, as well as many sessions of helpful discussions. Thanks to Professor Joel Greenspan at the Dept. of Neural and Pain Sciences, and Professor Maureen Stone at the Vocal Tract Visualization Lab, at the University of Maryland Baltimore, for being highly supportive for my study and willing to work around my schedule.

I am also really grateful to many people from other Universities. Thanks to Professor Angelos Barmpoutis at the University of Florida for his generous help and great effort in helping me solve fitting errors in DKI reconstruction. Although our collaborative work did not make it into this dissertation, the knowledge I learned from Angelos about higher order tensor made up for the foundations of reconstruction algorithms I developed in the dissertation research. Thanks to Professor Lily Wang at the University of Georgia, who was so willing to help and solved our critical statistical problem after many late night discussions.

I am fortunate to have many good friends who have always been there and really cheered me up in my most stressful days: Dr. Bao Zhang, Dr. Xinhui Zhou, Dr. Xiaofeng Liu, Dr. Minjie Wu, Professor Shaolin Yang, Dr. Weiying Dai, Jian Yang, Dr. Jie Liu, Dr. Yan Sun, Professor Emi Murano and many others.

My deepest gratitude goes to my family for their unconditional love, encouragement and support. I am thankful to my husband, Jiehua Li, who has endured all my stressful days, who always cheered me up and helped me regain my confidence. I am thankful to my parents, Yongping Zhuo and Xiaomei Shen, and my parents-in-law, Shuwang Li and Xiaowen Wang, for taking turns to come to the United States and help us around the house, while I was busy with work and study. I am thankful to my two lovely children, Zhuoxun and Zhuoxuan, who brought so much joy to my life and gave me the ultimate motivation to finish my dissertation. I am also thankful to my uncle, Dr. Gary Shen, for guiding me into the graduate study in United States.

Finally, I would like to thank the Department of Defense for supporting a majority of this work through their grants (# W81XWH-07-2-0118, # W81XWH-08-1-0725, PT 075827). I would also like to thank staffs in the Dept. of Electrical and Computer Engineering, Dr. Tracy Chung, Ms. Melanie Prange and Ms. Maria Hoo, for their help in guiding me through the whole Ph.D process.

It is impossible to remember all, and I apologize to those I have inadvertently left out.

Table of Contents

List of Tables

List of Figures

List of Abbreviations

ADC	Apparent Diffusion Coefficient
CC	Corpus Callosum
CLS	Constrained Linear Least Squares
CNS	Central Nervous System
CSF	Cerebrospinal Fluid
CTX	Cortex
CV	Coefficient of Variation
DAI	Diffusion Axonal Injury
DTI	Diffusion Tensor Imaging
DKI	Diffusion Kurtosis Imaging
DW	Diffusion Weighted
DWI	Diffusion Weighted MRI
EC	External Capsule
EPI	Echo Planar Imaging
FA	Fractional Anisotropy
FOV	Field of View
GM	Grey Matter
HC	Hippocampus
IQP	Interquantile range
K_a	Axial Kurtosis
K_r	Radial Kurtosis
LS	Linear Least Squares
MCPW	Monte Carlo pair-wise
MD	Mean Diffusivity
MK	Mean Kurtosis
MRI	Magnetic Resonance Imaging
PD	Proton Density
RF	Radio Frequency
ROI	Region of Interest
SNR	Signal-to-noise Ratio
STD	Standard Deviation
TBI	Traumatic Brain Injury
TE	Echo Time
TR	Repetition Time
WM	White Matter
λ_a	Axial Diffusivity
λ_r	Radial Diffusivity

Chapter 1. Introduction

A significant fraction of the human body is water. Water molecules in the human body are constantly undergoing Brownian motion or Random Walk. The diffusion of water molecules within the tissue is affected by a variety of factors including cellular structures, membranes, viscosity of different compartments, etc. (Basser et al., 2009). When there is change to the tissue microstructure, e.g., post-traumatic brain injury, the properties of the water diffusion will also change. For example, if brain injury causes cellular destruction (cells die or shrink, or cell membranes are damaged), there will be more free space for water molecules to move, leading to increased water diffusion. On the other hand, if there is cell swelling, as commonly observed acutely post injury, then there will be reduced extracellular space for water molecules to move, leading to reduced water diffusion. Therefore, by measuring the water diffusion change *in vivo*, we can monitor the patho-morphological changes in tissues.

Diffusion of water molecules in tissue can be measured *in vivo* using diffusion weighted Magnetic Resonance Imaging (MRI). MRI is a non-invasive imaging method that measures signals from protons within water molecules. Moving water molecules result in reduced MRI signal intensity compared to the static case, but such signal attenuation is usually neglected in conventional MRI because diffusion movement is small. In diffusion weighted MRI, a diffusion "weighting" is used to magnify the amount of signal attenuation caused by diffusion (Stejskal et al., 1965). The diffusion coefficient of tissue, D, can then be derived by comparing the diffusion weighted signal $S(b)$ at certain diffusion weighting, b (s/mm^2), to the non-diffusion weighted signal S_0 using a linear equation: $\ln S(b) = \ln S_0 - bD$. To characterize the anisotropic diffusion in tissues, we can further measure the diffusion coefficient along different directions and then model it by a diffusion ellipsoid (a 3×3 tensor), with its principle axis pointing along the direction for which diffusion is least restricted (with the highest diffusion coefficient, e.g., along white matter axons). Diffusion MRI using this tensor model is called Diffusion Tensor Imaging (DTI). DTI is a popular imaging method in studying white matter abnormality. White matter brain tissue (as opposed to gray matter), is primarily made up of bundles of neuronal axons that are highly directional. The diffusion coefficient is very high along the length of the axon bundle and very low in directions perpendicular to it. Fractional Anisotropy (*FA*), which measures the anisotropy of water diffusion, has been shown to be very sensitive in detecting subtle white matter microstructure changes (Bozzali et al., 2002; Karagulle Kendi et al., 2008; Schmierer et al., 2004).

Despite the great advantages of DTI in studying white matter abnormality, the use of DTI to study grey matter changes in brain injury has unfortunately received very little interest. This is mainly because diffusion in grey matter is largely isotropic and DTI has limited sensitivity to complex cellular structure changes in isotropic media. DTI, based on a largely simplified model, assumes that the diffusion displacement follows a Gaussian distribution, which is rarely the case in a real tissue environment. Indeed, when higher diffusion weightings are used (b = 2000 or 2500 s/mm^2, compared to b = 1000 s/mm^2 in DTI), the diffusion weighted signal deviate significantly from the mono-exponential decay predicted by the diffusion tensor model. This is because at high diffusion weighting, the proton signal becomes increasingly sensitive to heterogeneous diffusion distances arising from complex cellular structures. In order to characterize the more complex tissue microstructure changes, we then look into more extended models for diffusion MRI.

Among the many extended diffusion models, the diffusion kurtosis model (Jensen et al., 2005; Lu et al., 2006) stands out because it is relatively simple, does not impose more assumptions (e.g., tissue compartmentalization), and has a clinically feasible acquisition time. In Diffusion Kurtosis Imaging (DKI), the diffusion weighted signal equation is extended to include a quadratic term: $\ln S(b) = \ln S_0 - bD + 1/6b^2D^2K$, with K being the kurtosis parameter that captures the non-Gaussian diffusion property. As a relatively new imaging technique, there have only been limited studies on DKI, among which diffusion kurtosis is described as an imaging marker that captures brain tissue complexity (Jensen et al., 2010; Shaw, 2010) and has great potential as a more sensitive marker for tissue microstructure change (Falangola et al., 2008; Farrell et al., 2010; Jiang et al., 2011; Raab et al., 2010).

In this dissertation, DKI is applied in Traumatic Brain Injury (TBI) in a rat model, to study whether it can provide information above and beyond the widely-used DTI method. DKI does require more measurements and longer image acquisition time than typical DTI, due to the increased number of model parameters. Diffusion weighted images in DKI are also more susceptible to noise because stronger diffusion weightings (higher b-values) have to be used, which cause more signal attenuation. Thus, how different imaging schemes and levels of noise affect the DKI derived parameters are also studied, in addition to the search for a fast and reliable DKI reconstruction method. The goal of this dissertation is to introduce DKI as a more sensitive imaging method for studying brain injury. The methodology developed here is designed to facilitate the application of DKI in a clinical setting, namely, limited acquisition time, limited image signal-to-noise ratio (SNR) level and realtime data reconstruction and visualization.

The dissertation is organized as follows:

Chapter 2 provides background information about the principles of DTI and its values in studying diseased brain tissue, mainly, TBI. The chapter then continues to introduce the new DKI model and its potential value in revealing tissue microstructure changes.

Chapter 3 examines whether DKI provides any additional information about damaged brain tissue post experimental TBI in the rat model. This is a collaborative work. Animal preparation and tissue histology were provided by colleagues from the Dept of Anesthesiology and Center for Shock Trauma and Anesthesiology Research, at the University of Maryland School of Medicine. This work led to a paper published in NeuroImage in 2012 (Zhuo et al., 2012).

Chapter 4 describes an improved fast DKI reconstruction method that enables more reliable realtime data reconstruction and visualization for clinical DKI studies. This work led to a conference abstract at the Proceedings of the 19th annual meeting of the International Society of Magnetic Resonance in Medicine (ISMRM) in 2011 (Zhuo et al., 2011), and a conference paper at the Proceedings of IEEE International Symposium on Biomedical Imaging (ISBI) in 2011 (Barmpoutis and Zhuo, 2011).

Chapter 5 analyzes how diffusion weighted imaging schemes, image noise and reconstruction methods affect the accuracy and variability in DKI derived parameters.

The study was carried out on both real imaging data and Monte Carlo simulated data. Optimized imaging schemes and reconstruction methods, within a clinically feasible setting, are determined. The manuscript for this work is in preparation to be submitted to NeuroImage.

Chapter 6 is a summary of the main findings of this dissertation as well as future directions.

Chapter 2. Background

2.1 Diffusion MRI – the Gaussian Model

2.1.1 Diffusion of Water and the Basic Mathematics

Water molecules in the human body are constantly undergoing Brownian motion or Random Walk. Imagine dropping ink into a tub of water; the drop's size will become bigger as time goes on, with the center unchanged. As illustrated in Figure 2.1, an individual molecule would go through a random trajectory and move a distance of *s* after certain time *t*.

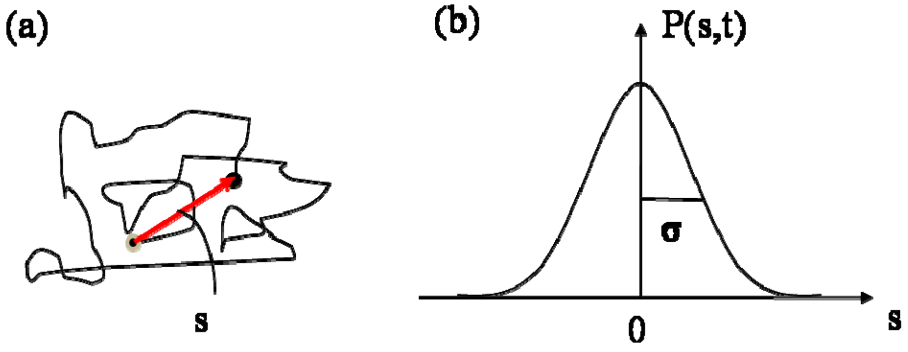

Figure 2.1. Schematic representation of random walk of a water molecule that has a displacement of *s* (red arrow) (a). The distribution of its displacement *s* after time *t* is shown in (b).

When water diffusion is free without any restriction, the probability of diffusion displacement *s* follows a Gaussian distribution with zero mean and a standard deviation σ that characterizes the average diffusion distance. If *D* is the diffusion coefficient of water molecules in the medium, *t* the diffusion time, then the typical diffusion distance (σ) is represented by $\sqrt{2Dt}$ according to Einstein's equation in 1905 (Einstein, 1956). The diffusion displacement distribution can then be written as:

$$P(s,t) = \frac{1}{\sqrt{4\pi Dt}} e^{-s^2/4Dt} \tag{2.1}$$

In a homogeneous environment, like in a tub of water, diffusion is isotropic and the displacement distribution is the same in all directions.

Water diffusion is not always isotropic, however. If a stalk of celery is immersed in the water tub, then you would imagine that the water molecules will diffuse more easily along the direction of the celery fibers than perpendicular to it. The diffusion distribution after some time will then be more oval than spherical, with the oval pointing along the direction of the celery fibers. In this case, diffusion would still follow a multivariate Gaussian distribution as initially indicated by Eq. 2.1, but instead with different diffusion coefficients along different directions, like an ellipsoid (See illustration in Figure 2.2).

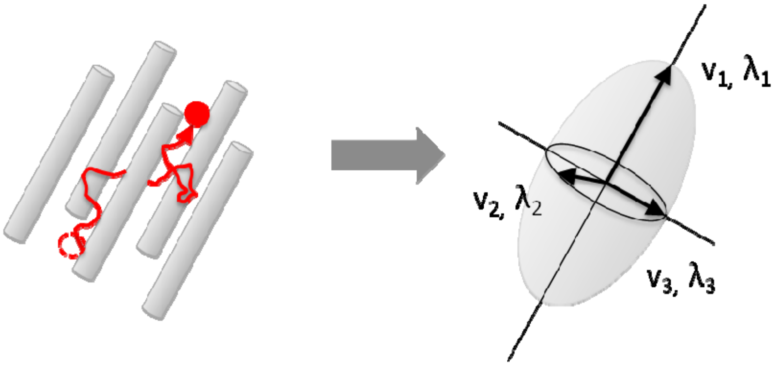

Figure 2.2. Water diffusion in an environment contains densely packed long fibers. Due to collisions with the fibers, water molecules would travel less distance perpendicular to the fiber direction than along the fiber. It can be modeled as an ellipsoid with preferred direction pointing toward the fiber direction.

To determine the shape and orientation of the diffusion ellipsoid, we need to know the diffusion coefficient along different directions. The diffusion ellipsoid can be characterized by a seond-order tensor called the diffusion tensor **D**. Since the Gaussian distribution is symmetric along each of the *x*, *y*, *z* directions, **D** is a fully symmetric 3×3 tensor with six independent elements. It can be uniquely determined if diffusion coefficients along a minimum of six non-collinear directions (e.g., *xx*, *yy*, *zz*, *xy*, *xz*, *yz* or a rotation of the directions) are known. By eigen-decomposition (Eq 2.2), three eigenvectors $\mathbf{v_1}$, $\mathbf{v_2}$, $\mathbf{v_3}$ and corresponding eigenvalues λ_1, λ_2, λ_3 can be derived. The eigenvectors represent the three principle axes of the diffusion ellipsoid and the eigenvalues represent diffusion coefficients along each principle axis. The eigenvalues are typically ordered as $\lambda_1 > \lambda_2 \geq \lambda_3$ and $\mathbf{v_1}$ is the direction of the preferred diffusion direction.

$$\mathbf{D} = \begin{bmatrix} D_{xx} & D_{xy} & D_{xz} \\ D_{xy} & D_{yy} & D_{yz} \\ D_{xz} & D_{yz} & D_{zz} \end{bmatrix} \Rightarrow \begin{bmatrix} \lambda_1 & 0 & 0 \\ 0 & \lambda_2 & 0 \\ 0 & 0 & \lambda_3 \end{bmatrix} \cdot \begin{bmatrix} \mathbf{v}_1 & \mathbf{v}_2 & \mathbf{v}_3 \end{bmatrix} \tag{2.2}$$

Water diffusion in biological tissue is affected by a variety of factors, including cellular structures, membranes, viscosity of different compartments, etc. (Basser et al., 2009). When there is a change in the tissue microstructure due to disease, the diffusion properties will also change. So measuring water diffusion *in vivo* can be a very useful tool to detect underlying tissue abnormality.

2.1.2 How to Measure Diffusion using MRI

Magnetic Resonance Imaging (MRI) is a non-invasive imaging technique that measures proton signal (^{1}H) in a strong magnetic field (typically, 1-3 Tesla). Figure 2.3 shows a typical diagram for the spin echo imaging scheme introduced by Hahn (Hahn, 1950). When placed in the magnetic field B_0, protons precess at an angular speed of $\omega = \gamma B_0$ along the main magnetic field. γ is the gyromagnetic ratio, a constant specific to the nucleus under examination (for the proton, γ = 42.58 MHz/T). A typical MRI scan starts with an excitation radio frequency (RF) pulse and ends with an echo signal at the receiver. The time between the center of the excitation RF pulse and the center of the echo signal is called echo time (TE). At time $t = 0$, a 90° RF pulse rotates the spins 90° to the transverse plane, laying along the x-axis and the phases of spins are in perfect coherence (Figure 2.3 (a)). As time goes, spins start to lose their phase coherence (dephase) due to spin-spin relaxation and magnetic field inhomogeneity (Figure 2.3 (b)). The spin-spin relaxation causes MR signal to decay at a time constant T_2 (~80-100ms in brain tissues) and T_2 is the intrinsic MRI property of a specific tissue type. The magnetic field inhomogeneity causes spins to precess at different frequencies depending on their spatial locations. At t = TE/2, a 180° refocusing RF pulse is applied that flips all the spins to the negative x-axis (Figure 2.3 (c)). Spins that precess at different speeds continue to do so, with faster spins still precessing faster and slower spins still precessing slower, so they are regaining phase coherence (rephase) (Figure 2.3 (d)). After a same period of time TE/2 (*i.e.* at t = TE), all spins precess back to the $-x$ position and form an echo (Figure 2.3 (e)). Note that for moving spins, since they see a different magnetic field during the dephase and rephase stages, they will not return to full phase coherence at TE, leading to phase dispersion and hence a reduced echo signal.

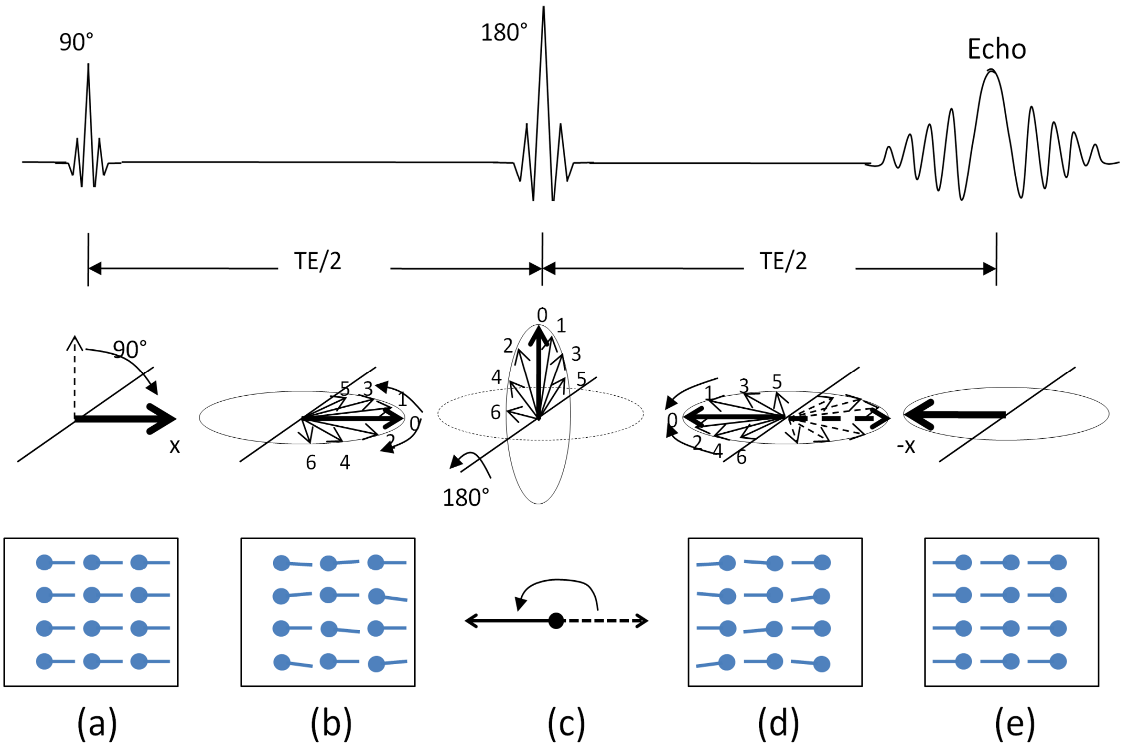

Figure 2.3. A typical pulse diagram for spin echo imaging scheme, with illustration of phase evolution of spins at different stages of the image acquisition: (a) excitation (t = 0); (b) dephasing; (c) refocusing (t = TE/2); (d) rephrasing and (e) echo (t = TE). TE is the echo time.

The signal attenuation due to diffusion movement of spins is negligible in regular MRI imaging because the movement is very small. But this effect can also be magnified by introducing diffusion weighted gradients at both side of the refocusing pulse as shown in Figure 2.4 in red (Stejskal, 1965). When strong magnetic gradients G (mT/mm) are applied along a particular imaging direction (e.g., the x direction), the magnetic fields then vary along the x-direction, producing a location-dependent magnetic field $B(x) = B_0+Gx$. After a duration of δ, each spin will also have a location dependent phase accrual $\phi(x) = \gamma G\delta$ (Figure 2.4(b)). For stationary spins/molecules (blue spins), their accumulated phase from the 1st diffusion gradient is negated after the application of the 2nd diffusion gradient of the same strength and duration, so they regain their phase coherence at TE. However, for spins/molecules that are undergoing random walk (red spins), since they have traveled a distance by the time they experience the 2nd diffusion gradient, they will have phase dispersion at TE, leading to an attenuated echo signal.

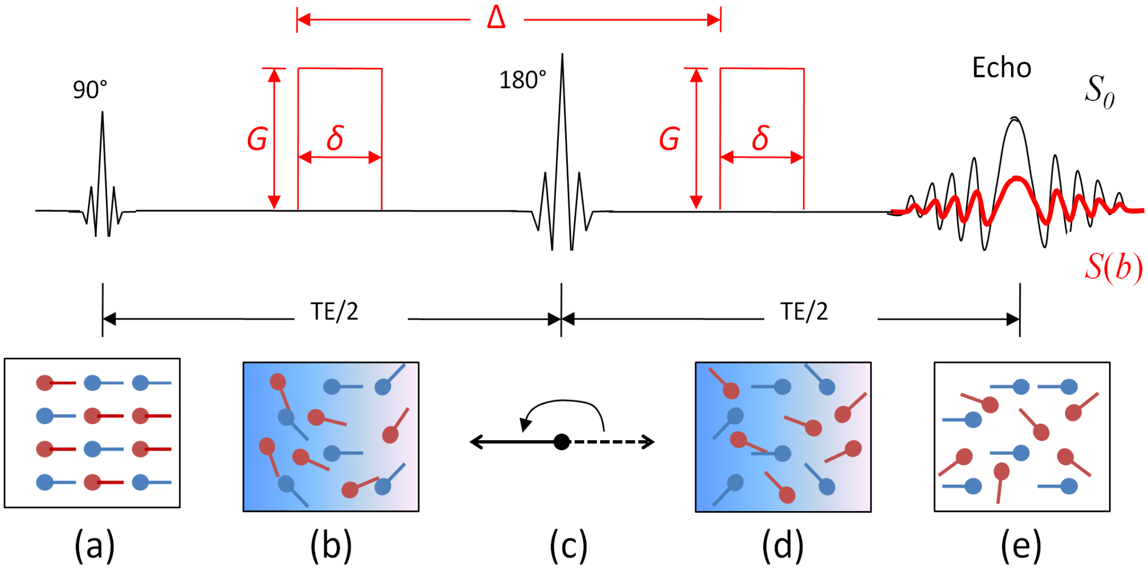

Figure 2.4. A typical pulse diagram for diffusion weighted spin echo imaging scheme with illustrations of spin phase evolution. Shown in red is the added diffusion gradients compared to Figure 2.3.

Several factors of the diffusion weighting gradients control the extent of the phase dispersion, where more phase dispersion is reflected in a more attenuated signal. Specifically, the strength of the diffusion gradients, G, controls how much the magnetic field varies spatially. Since the spin precession depends on the local magnetic field, a strongly varying magnetic field will cause more phase dispersion of the spins. The duration of the diffusion gradient, δ, determines the time over which the spins experience a position-dependent phase accrual. The time interval between the two diffusion gradient applications, Δ, is typically referred to as the "diffusion time" and is directly related to the diffusion distance of water molecules that we are measuring, with longer diffusion time leading to longer diffusion distances. The combination of these diffusion weighting factors is usually represented by a b-value (s/mm^2) and is calculated as:

$$b = \gamma^2 G^2 \delta^2 (\Delta - \delta / 3) \tag{2.3}$$

where γ is the gyromagnetic ratio. Stronger diffusion weighting (higher b-value), higher G or longer Δ, δ, will lead to a more attenuated signal.

If the echo signal at t = TE without any diffusion weighted gradients (b = 0 s/mm^2) is S_0, then the diffusion weighted signal can be written as:

$$S(b) = S_0 e^{-bD} \tag{2.4}$$

The diffusion coefficient D in the tissue can be measured through MRI by acquiring a minimum of two datasets. One is without any diffusion weighting (b = 0 s/mm^2) and one is with diffusion weighting (some particular b-value). The diffusion coefficient for each voxel can then be calculated according to Eq. 2.4. Sometimes more than two b-values are acquired in order to improve the estimation accuracy. In that case, D can be estimated through a linear least squares fitting of equation as:

$$\ln\left(S(b) / S_0\right) = -bD \tag{2.5}$$

2.1.3 Diffusion Weighted MRI (DWI)

A typical Diffusion Weighted MRI (DWI) acquisition collects images with several b-values along 3 directions (x, y and z) (Le Bihan et al., 1986). A diffusion coefficient can be fitted using Eq. 2.5 for each direction and an apparent diffusion coefficient (*ADC*) can then be calculated by averaging the diffusion coefficient along all three directions.

$$ADC = (D_x + D_y + D_z)/3 \tag{2.6}$$

Due to the inherent low signal-to-noise ratio (SNR) in diffusion weighted images, typically several repetitions of data are acquired and then averaged to improve SNR. Figure 2.5 shows a typical set of diffusion weighted images of a brain slice with different b-values and the calculated *ADC* map. Notice the heterogeneous signal decay pattern in the brain corresponding to different brain tissue structures. Although the initial signal intensities are similar, the diffusion weighted signal attenuation of the red voxel is much faster than the blue voxel (Figure 2.5), resulting in a much lower signal intensity at b = 1500 s/mm^2 and a higher ADC value for the red voxel than for the blue one.

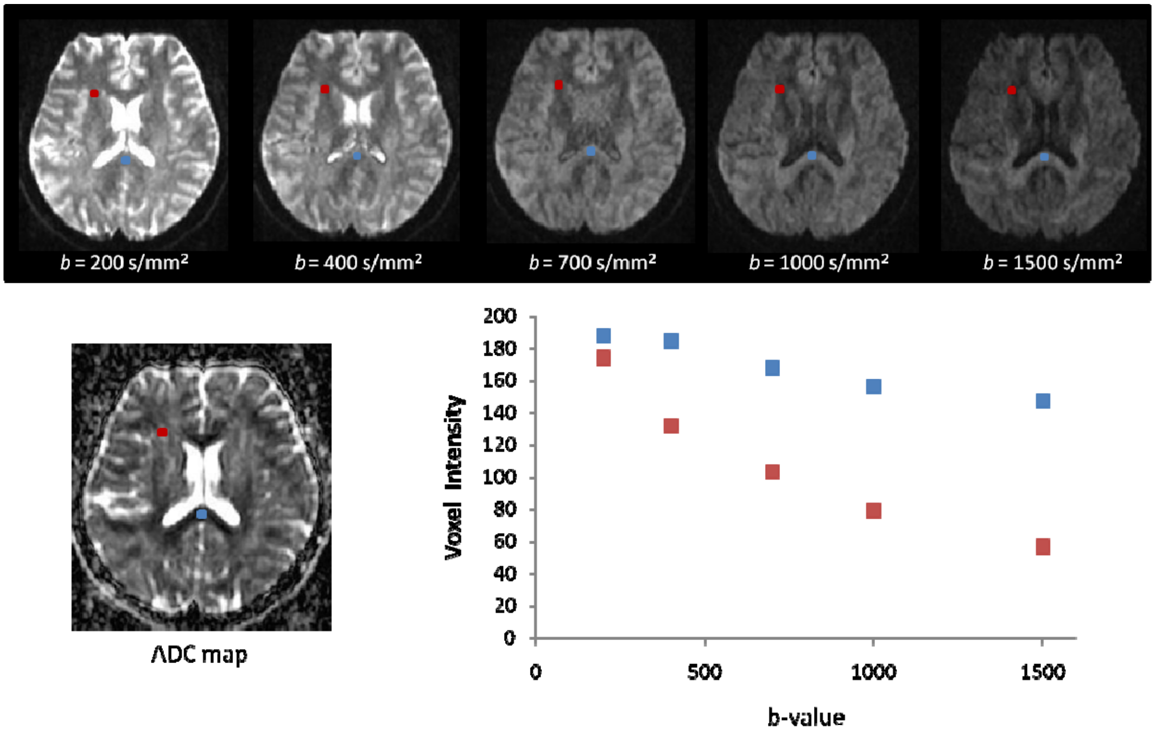

Figure 2.5. Diffusion weighted images at different b-values. In this example, the red voxel has a large amount of signal loss, suggesting fast diffusion compared to the blue voxel.

2.1.4 Diffusion Tensor Imaging (DTI)

DWI can only measure the average diffusion. In order to characterize anisotropic diffusion in the tissue, we will need to know the diffusion tensor **D**.. This can be done by applying diffusion gradients in at least 6 co-linear directions, measuring the corresponding diffusion coefficients and then fitting for the diffusion tensor **D** (Basser et al., 1994). This imaging technique is called Diffusion Tensor Imaging (DTI). Figure 2.6 shows diffusion weighted images in the brain at b = 0 s/mm^2 (S_0) and b = 1000 s/mm^2 measured from 6 diffusion directions (x, y, z): (0.707, 0, 0.707), (-0.707, 0, 0.707), (0, 0.707, 0.707), (0, 0.707, -0.707), (0.707, 0.707, 0), (0.707, -0.707, 0). Notice the highly heterogeneous signal attenuation pattern with different diffusion directions due to the complexity of tissue microstructure in the brain.

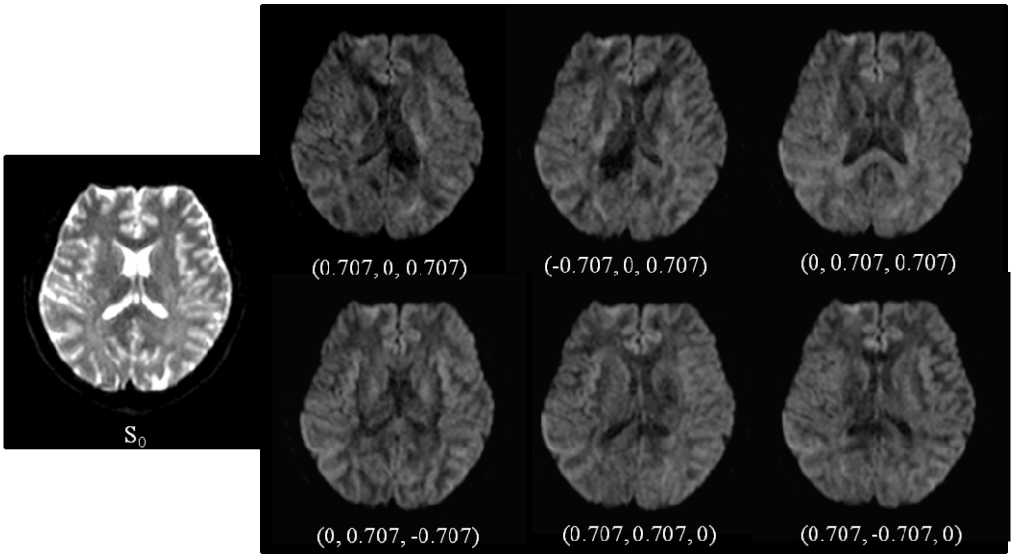

Figure 2.6. Diffusion weighted images at b = 0 s/mm^2 (S_0) and b = 1000 s/mm^2 from 6 diffusion directions: (0.707, 0, 0.707), (-0.707, 0, 0.707), (0, 0.707, 0.707), (0, 0.707, -0.707), (0.707, 0.707, 0), (0.707, -0.707, 0).

The DTI signal $S(\mathbf{g},b)$ can be written as an extension of the DWI signal (Eq. 2.4):

$$S(\mathbf{g},b) = S_0 e^{-b \cdot \mathbf{g}^T \cdot \mathbf{D} \cdot \mathbf{g}} \tag{2.7}$$

where $\mathbf{g} = [g_x, g_y, g_z]$ is a unit vector that describes the direction of applied diffusion gradients, **D** is the diffusion tensor, *b* is the applied b-value, and S_0 is the signal without any diffusion weighting. Equation (2.7) can be solved as a linear equation after taking the natural log of both sides and explicitly writing out elements in **D** and **g** in vector form. Let $\overline{\mathbf{D}} = [D_{xx}, D_{yy}, D_{zz}, D_{xy}, D_{xz}, D_{yz}]^T$, $\overline{\mathbf{g}} = [g_x^2, g_y^2, g_z^2, 2g_x g_y, 2g_x g_z, 2g_y g_z]$, then Eq. 2.7 can be written as:

$$\ln(S(\mathbf{g},b)/S_0) = -b \cdot \overline{\mathbf{g}} \cdot \overline{\mathbf{D}} \tag{2.8}$$

After eigen-decomposition of the diffusion tensor **D**, eigenvalues $\lambda_1, \lambda_2, \lambda_3$ ($\lambda_1 > \lambda_2 \geq \lambda_3$) can be estimated. Shown below are several DTI parameters that are of the most interest (Basser and Pierpaoli, 1996):

1. Mean Diffusivity (*MD*) (also referred to as *ADC*))

$$MD = \frac{\lambda_1 + \lambda_2 + \lambda_3}{3} \tag{2.9}$$

   MD characterizes the average diffusivity.

2. Fractional Anisotropy (*FA*)

$$FA = \frac{\sqrt{3[(\lambda_1 - MD)^2 + (\lambda_2 - MD)^2 + (\lambda_3 - MD)^2]}}{\sqrt{2(\lambda_1^2 + \lambda_2^2 + \lambda_3^2)}} \tag{2.10}$$

   FA characterizes how anisotropic the diffusion is. *FA* is always within the range of [0, 1], with *FA*=0 representing completely isotropic diffusion ($\lambda_1 = \lambda_2 = \lambda_3$) and *FA*=1 representing highly anisotropic diffusion ($\lambda_1 >> \lambda_2 \approx \lambda_3$).

3. Axial Diffusivity (λ_a) and Radial Diffusivity (λ_r)

$$\lambda_a = \lambda_1, \qquad \lambda_r = \frac{\lambda_2 + \lambda_3}{2} \tag{2.11}$$

In regions of high FA, λ_a and λ_r are usually calculated to characterize the diffusivity along and perpendicular to the fiber, respectively.

2.2 Applications of Diffusion MRI in Traumatic Brain Injury (TBI)

2.2.1 Structures in the Brain

The major types of cells in the central nervous system (CNS) are: neurons, axons, myelin sheath and glial cells (Edgar et al., 2009). An understanding of the basic functions of these cellular structures is crucial for understanding brain injury mechanisms.

Figure 2.7 shows a schematic representation of these cellular elements. Neurons are the core components of the CNS. Neurons process and transmit information by electrical and chemical signaling through axons and synapses. A typical neuron possesses a cell body, some dendrites and an axon. Axons are the primary transmission lines of the CNS. Axons connect neurons in different parts of the brain regions and conduct electrical impulses. Axonal diameters range from less than 0.2μm to up to 10μm. A majority of axons with diameters greater than 0.2μm are myelinated, that is, the axons are wrapped with an electrically insulating layer called a myelin sheath, which helps to increase the propagation speed of impulses along the axons (Hirano and Llena, 1995). Glia cells are a broad category of non-neuronal cells that surround and ensheath neuronal cell bodies, axons and synapses throughout the CNS. They make up most of the cells in the brain. They can further be separated to: Astrocytes, which maintain homeostasis in the brain by providing neurons with energy and substrates for neurotransmission; Oligodendrocytes, which form a myelin sheath around axons in the CNS; and Microglia cells, which keep the brain under surveillance for damage or infection (Allen and Barres, 2009).

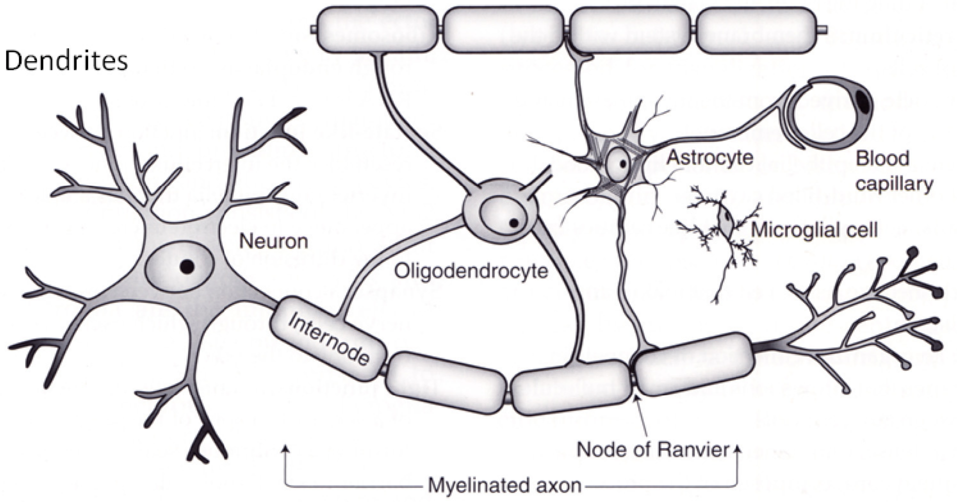

Figure 2.7. Schematic representation of the major cellular elements in the central nervous system (CNS), which include: neurons, axons, myelin sheath and glial cells (Oligodendrocytes, Astrocytes, Microglia cells). Figure is adapted from (Edgar and Griffiths, 2009) with copyright obtained from Elsevier.

In a macrostructure view, the brain has three main components: grey matter, white matter and cerebrospinal fluid (CSF) (Fig. 2.8). Grey matter is distributed at the surface of the cerebral hemispheres as well as in the depth of the cerebrum and is composed mostly of neurons, glial cells and capillaries. White matter is composed of mostly myelinated axons. The name ‘white’ is used because fresh white matter tissue appears lighter in color due to the fatty myelin sheath. Within a white matter tract, the majority of axons lie parallel to each other (Morell, 1984). CSF is clear bodily fluid that occupies the ventricular system and appears around the brain cortex surface.

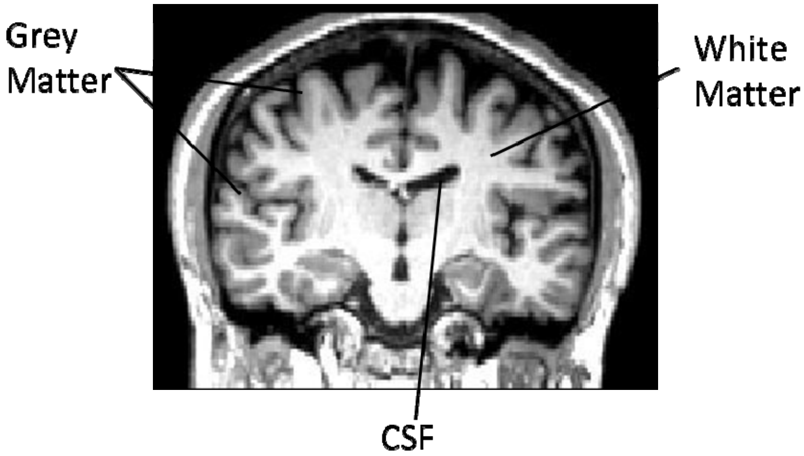

Figure 2.8. A MRI image of brain showing regions of grey matter, white matter and cerebrospinal fluid (CSF).

2.2.2 Traumatic Brain Injury (TBI)

Traumatic brain injury (TBI) is the primary cause of death and disability in the U.S. population under 45 years of age and represents a significant economic and social burden to the families and the society at large (Sosin et al., 1996). TBI is the result of an external mechanical force applied to the brain, leading to temporal or permanent impairments, functional disability, or psychosocial maladjustment (Steyerberg et al., 2008). TBI can manifest clinically from concussion to coma and death. Patients with TBI follow a highly variable clinical course, with initial status frequently discrepant from long-term neurological outcome (Cordobes et al., 1986). No objective biological measure has been established to accurately predict long-term neurological outcome in these patients.

The primary injury to the brain is a result of sudden acceleration, deceleration and/or rotational forces. These forces cause cortical contusions (bruises of the brain tissue) and hemorrhages (bleeding) when the brain hits the skull (Thibault and

Gennarelli, 1990), and deeper cerebral lesions when white matter axons are stretched and damaged, as well as shearing injuries at the grey matter and white matter interface (Blumbergs et al., 1994). Following the initial trauma, injury is propagated through various biomolecular and cellular changes, which causes widespread degeneration of neurons, glial cells and axons. These secondary injuries are ultimately the deciding factors in patient recovery (Gentry, 1994). Therefore it is critical to be able to characterize these changes through *in vivo* imaging markers to help patient management and recovery. In this dissertation, more emphasis will be on the cellular structure changes following TBI, as these are the changes that are detectable through tissue diffusion property changes captured by diffusion MRI.

Pathophysiology results from experimental TBI models in rat/mice suggest that injury to the brain tissues is characterized by early neuronal loss together with a transient increase in numbers of astrocytes and microglial cells (Cheng et al., 2003). Such an abnormal increase in the number of astrocytes due to destruction of nearby neurons is called astrogliosis and the reactive astrogliosis are believed to play essential roles in preserving neurons and restricting inflammation (Myer et al., 2006).

The time course of axonal pathology is that the axons will swell up initially in response to injury. Some swelling will resolve and some will result in broken axons with terminal axon bulbs. Damage may also involve loss of the myelin sheath (also called demyelination), which can progressively get worse in a delayed post injury stage.

Cerebral edema, which is an excess accumulation of water in the intracellular and/or extracellular space of the brain, also typically occurs following TBI. Intracellular edema (also called cytotoxic edema) or cell swelling typically happens immediately following traumatic injury due to a change in the cellular metabolism resulting in inadequate functioning of the sodium and potassium pump in the cell membrane. Extracellular edema (also called vasogenic edema) develops more slowly over time as a result of failure of the Blood-brain barrier (a barrier that separates circulating blood and CSF and maintains the integrity of CSF). The development of cerebral edema can also cause compressive forces toward other brain tissue, elevate intracranial pressure and reduce cerebral blood flow, which may cause further damage to the brain (Greve and Zinc, 2009).

2.2.3 Diffusion MRI in the Brain and their Clinical Indications

Diffusion MRI has long been used as a powerful tool in studying neurological disease as it provides *in vivo* measurements of tissue microstructure change that cannot otherwise be easily detected through conventional imaging. Diffusion properties of different brain tissues namely grey matter, white matter and CSF, exhibits very different features. Diffusion in grey matter is largely non-directional (isotropic) as it is mostly composed of neurons and glial cells ($FA < 0.2$). Diffusion in white matter is highly anisotropic due to the myelinated axons, which restrict water diffusion in such a way that the axial diffusivity can be as much as seven times the radial diffusivity ($FA \sim 0.45$ to 0.8) (Song et al., 2002). Developmental and aging studies in both human and animal models have reported increase in *FA* throughout the early stages of brain development (to adolescence), due to the myelin formation process. The *FA* value plateaus in adulthood and starts to decline after age 60, due to the loss of myelin integrity associated with aging (Zhang et al., 2007; Lebel et al., 2008; Pfefferbaum et al., 2005). Diffusion in CSF is similar to free diffusion in water, so *MD* is extremely high (~3×10^{-3} mm^2/s) and *FA* is almost 0.

Figure 2.9 shows a structure MRI brain image indicating grey matter, white matter and CSF regions. Together also shown are the *MD*, *FA,* λ_a and λ_r maps, as well as a color-coded *FA* map indicating the principle diffusion directions (eigenvector corresponding to the largest eigenvalue of the diffusion tensor **D**). Notice the high *FA* values in white matter regions associated with high λ_a and low λ_r, and low *FA* in grey matter regions and CSF. On the other hand, *MD* does not show any contrast between grey and white matter, while CSF shows extremely high diffusivity.

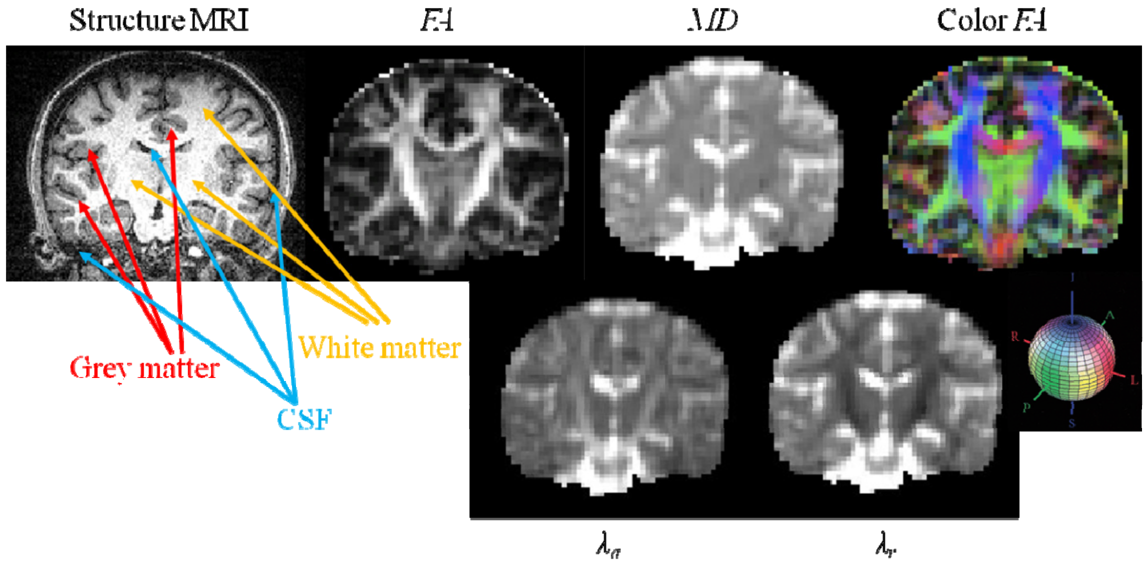

Figure 2.9. Brain structure MRI image and DTI maps (*FA*, *MD*, Color *FA*, λ_a and λ_r). Indicated in the structure MRI image are grey matter (grey regions as pointed using red arrows), white matter (white regions as pointed using yellow arrows) and CSF (dark regions as pointed using blue arrows). Color FA shows the principle diffusion direction, color-coded. Blue: Inferior-Superior; Red: Left-Right; Green: Anterior-Posterior.

In brain injury studies, reduced *MD* and/or increased *FA* are commonly observed in stroke (Armitage et al., 1998), acute traumatic brain injuries (Shanmuganathan et al., 2004) or brain tumor (Guo et al., 2002). These DTI changes are typically associated with cellular swelling, cytotoxic edema or increased cellularity, leading to reduced extra-cellular space. Increased *MD* and/or reduced *FA* are more often observed in many kinds of chronic brain injury (zelaya et al., 1999; Cercignanti et al., 2001; Shanmuganathan et al., 2004) and may indicate cellular membrane disruption, cell death, tissue cavitation, vasogenic edema, etc., which leads to increased extra-cellular space and reduced tissue structure.

DTI is used widely to study white matter abnormalities because *FA* has been shown to be very sensitive in detecting subtle white matter microstructure changes. Damage to white matter axons can also cause decreased neuro-transmission in the brain, leading to decreased cognitive function. So changes in *FA* often correlates with clinical presentation and cognitive functions in many neurological disorders such as Alzheimer's Dementia (Bozzali et al., 2002), Multiple Sclerosis (Schmierer et al., 2004), Parkinsons's Disease (Karagulle Kendi et al., 2008), etc.. More specifically, the axial diffusivity (λ_a) is believed to reveal axonal integrity, and the radial diffusivity (λ_r) is believed to reveal myelin integrity (MacDonald et al., 2007; Sidaros et al., 2008; Song et al., 2003).

2.2.4 Diffusion MRI Applications in TBI

Diffusion Axonal Injury (DAI) represents the most common form of TBI, comprising approximately half of all such injuries (Arfanakis et al., 2002). Axonal injury is also a powerful predictor of morbidity and mortality (Greve et al., 2009). However, both computed tomography (CT) and traditional MRI have limited sensitivity in detecting and characterizing DAI in the acute trauma setting (Wilson et al., 1988; Parizel et al., 1998). Diffusion MRI is quickly gaining interest in the TBI community and diffusion parameters are evolving as new imaging biomarkers that have potential prognostic values. Early DWI studies in TBI show an increased sensitivity in detecting DAI related lesions (Ezaki et al., 2006). Whole brain ADC was also shown to be able to independently indicate TBI in spite of normal conventional MRI findings (Shanmuganathan et al., 2004).

More recent studies using DTI focus more on the white matter microstructure change associated with DAI thanks to the sensitivity of *FA* and axial/radial diffusivity in detecting axonal injury. As explained previously, TBI is an evolving and dynamically changing injury rather than a terminal disease, so the diffusion properties are also changing through the different injury phases. At the acute stage (0-6 days), an elevated *FA*, reduced *MD* and reduced λ_r are typically observed, indicating an inflammatory response such as axonal swelling or cytotoxic edema (Bazarian et al., 2007; Wilde et al., 2008; Chu et al., 2009). Increased *FA* and decreased λ_r are also found to correlate with severity of post-concussion symptoms (Wilde et al., 2008). Such patterns of DTI value change are found to persist to the semi-acute phase (12 days post-injury), with subsequent partial normalization at a delayed stage (3-5 months post injury). Moreover, normalization of *FA* is associated with reduction of TBI symptoms, matching a typical recovery timeframe (Mayer et al., 2010). At chronic stages (6 months or longer), most studies report a reduced *FA* and increased *MD* as a result of increased λ_a, which is consistent with axonal damage. Changes in *FA* are also shown to correlate with injury severity (Benson et al., 2007), cognitive deficits (Kraus et al., 2007; Niogi et al., 2008) and functional outcome (Wilde et al., 2006). Increased λ_r, as an indication of irreversible myelin damage, is also observed in severely injured but not mildly injured TBI patients (Kraus et al., 2007).

2.3 Diffusion Kurtosis Imaging (DKI) – Beyond the Gaussian Model

2.3.1 Non-Gaussian Behavior in Water Diffusion

Despite the great advantages of DTI, the assumption of diffusion displacement distribution being Gaussian and diffusion weighted signal *S* following a mono-exponential decay is a largely simplified model. A typical DTI imaging voxel size of 2×2×2 mm^3 is much bigger than any of the cell structures, which are in the μm size range. Within an imaging voxel there are numerous cell membranes, with various thicknesses and different viscosities. Water diffusion measured by MRI is an averaged process of millions of water molecules encountering a variety of obstacles, so its deviation from the Gaussian model is well expected. In routine DTI, b-values of 1000 s/mm^2 are typically used with a diffusion time around 50 ms. With such a setting, DTI is sensitive to a minimum diffusion distances of 5-10 μm, where approximately 23% to 63% of diffusion weighted signal attenuation can be measured. Water molecules that move greater distances dominate the diffusion weighted signal decay such that restricted diffusion within smaller tissue compartments is largely invisible in DTI. In this range of diffusion distances, the Gaussian model is still a fairly good estimate of the diffusion weighted signal attenuation in MRI (Figure 2.10). When larger b-values are used, diffusion weighted imaging becomes increasingly sensitive to more restricted diffusion and the heterogeneous diffusion distances arise from the underlying complex cellular structures. Therefore the diffusion weighted signal deviates from the mono-exponential decay predicted by the Gaussian model (Niendorf et al., 1996; Assaf et al., 1998). This is evident in the measured diffusion weighted signal attenuation $S(b)/S_0$ (blue circles) shown in Figure 2.10: a clear deviation from the mono-exponential decay (green line) is observed for b-values beyond 1000 s/mm^2.

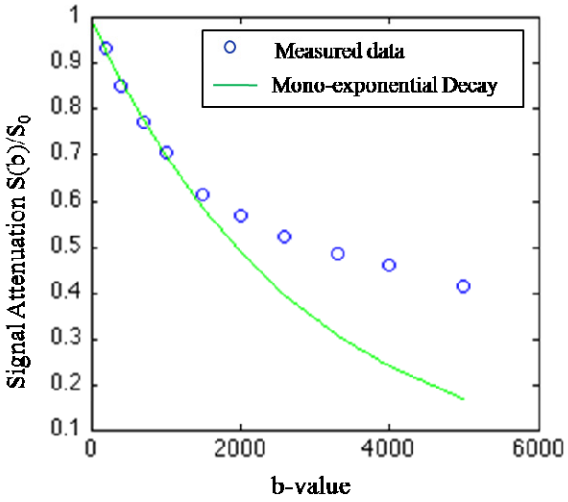

Figure 2.10. Measured diffusion weighted signal attenuation $S(b)/S_0$ (blue dots) at b-values ranging from 0 to 5000 s/mm^2.

2.3.2 Other non-Gaussian Diffusion Models

1) Bi-exponential model

There have been several models being proposed to investigate non-monoexponential diffusion behavior. The bi-exponential model is a natural choice considering there are two main compartments within the tissue: intra-cellular and extra-cellular (Mulkern et al., 1999; Maier et al., 2004). In the bi-exponential model, there are assumed to be two compartments in the tissue: a fast diffusing component and a slow diffusing component. If their respective volume fractions are A_f and A_s, and their diffusion coefficient within the components are D_f and D_s, then the diffusion weighted signal attenuation $S(b)/S_0$ can be written as:

$$S(b)/S_0 = A_f e^{-bD_f} + A_s e^{-bD_s} \tag{2.12}$$

Although the bi-exponential model fits the DW signal attenuation well, it is difficult to associate physical meaning to the two compartments, since the volume fractions of the fast and slow diffusing components are inconsistent with the known ratio between the intra-cellular and extra-cellular compartments (Niendorf et al., 1996). Furthermore, multi-exponential signal decay is also observed in a single compartment (Kiselev and Ilyasov, 2007).

2) q-space method

A more general and thorough approach is the q-space theory, which directly relates the diffusion signal decay to the displacement distribution function of the water molecules (Cohen and Assaf, 2002). Instead of a b-value that characterizes the diffusion weighting, a parameter q is defined as $\gamma\delta G/2\pi$ (γ is the gyromagnetic ratio, δ is the duration of the diffusion gradient, G is the amplitude of the diffusion gradient) by separating the diffusion time Δ (the separation between the two diffusion gradients as explained in section 2.1.2) out as an independent parameter. The theory is based on the Fourier relationship between the signal decay and the displacement distribution profile:

$$E_\Delta(\mathbf{q}) = \int \overline{P}_s(\mathbf{R},\Delta)\exp(i2\pi\mathbf{q}\cdot\mathbf{R})d\mathbf{R} \tag{2.13}$$

where $E_{\Delta}(\mathbf{q})$ represents the signal decay as a function of $\mathbf{q}$, R is the net displacement vector ($R = r - r_0$), and $\overline{P}_s(\mathbf{R},\Delta)$ is the displacement property. Figure 2.11 shows an illustration of the distribution profile for water in different tissue environments. In a free diffusion environment (Figure 2.11 (a)), the displacement distribution profile follows a Gaussian distribution. The distribution becomes increasingly broader with increasing diffusion time, as expected since water molecules should diffuse a longer distance given longer diffusion time. In brain tissues (Figure 2.11 (b)), the diffusion displacement is non-Gaussian, although a broad peak can still be observed at longer diffusion times. In a diffusion direction radial to white matter axons (Figure 2.11 (c)), the diffusion displacement profile is a very narrow peak that does not change with increasing diffusion time, indicating restricted diffusion that is directly associated with cell size (Cohen and Assaf, 2002).

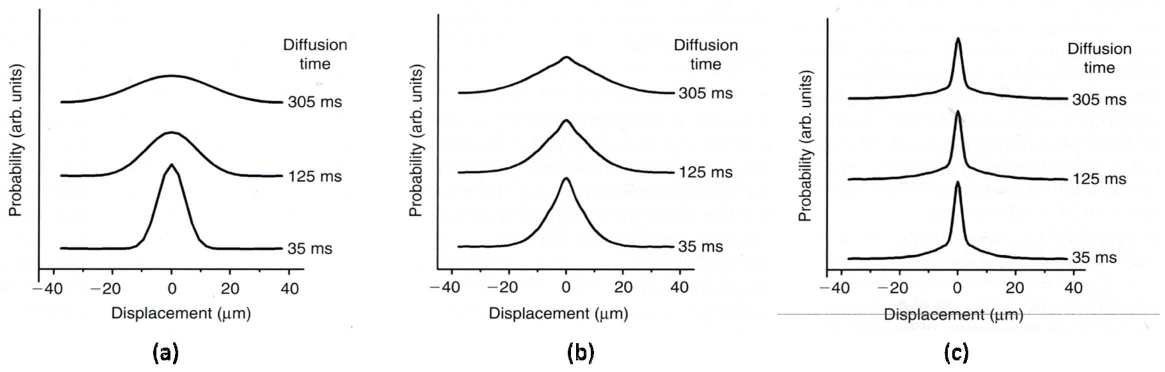

Figure 2.11. Diffusion displacement profiles for water in different tissue environments: (a) free diffusion environment, (b) excised rat brain tissue and (c) the radial direction of excised bovine optic nerve. Figure is adapted from Cohen and Assaf (2002) with copyright from John Wiley & Sons, Ltd..

Although the q-space method can fully describe the diffusion profile and provide detailed information about tissue microstructure, the disadvantage is much longer acquisition times (in order to sample the whole q-space), and high demands on imaging hardware in order to provide extremely strong diffusion gradients (the maximum q needed is equivalent to a b-value of approximately to 30000 s/mm^2). Therefore, it is rarely used in clinical practice.

3) Other models

Other models proposed to solve the non-Gaussian behavior of water diffusion include the stretched exponential model (Bennett et al., 2003) and the generalized DTI model (Ozarslan and Mareci, 2003). Since they are less popular and less indicated in clinical studies, they will not be discussed in any further detail here.

2.3.3 Diffusion Kurtosis Model

The diffusion kurtosis model was first introduced by Jensen in 2005 (Jensen et al., 2005) and later extended by Lu to a full kurtosis tensor expression (Lu et al., 2006). The diffusion kurtosis model includes an excess kurtosis into the diffusion model to describe the deviation of diffusion displacement from the Gaussian distribution. It is a simpler approach than the q-space method to describe the non-Gaussianity in the diffusion distribution function. It has been shown to fit data well up to a moderately large b-value ($b \sim 2500$ s/mm^2) (Jensen et al., 2005; Lu et al., 2006).

Mathematically, excess kurtosis (K) is a dimensionless statistical metric for quantifying non-Gaussianity of a probability distribution and is defined as:

$$K = \frac{\mu_4}{\mu_2^2} - 3 \tag{2.14}$$

where μ_2 and μ_4 are the 2^{nd} and 4^{th} order central moment of the distribution. If the distribution is Gaussian, then $K = 0$. A more sharply peaked distribution will have $K > 0$ and a more broad peaked distribution will have $K < 0$. Figure 2.12 (a) shows an illustration of diffusion displacement probability distribution with different kurtosis and figure 2.12 (b) shows the diffusion weighted signal fitted by the diffusion and the kurtosis model.

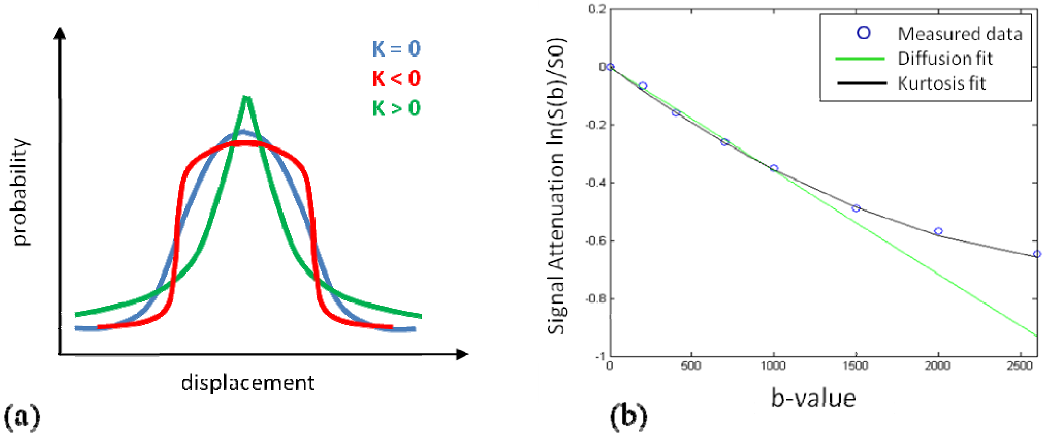

Figure 2.12. Diffusion displacement probability distribution with different kurtosis values (a). (b) Measured diffusion weighted signal attenuation $\ln(S(b)/S_0)$ (blue circle) shows clear deviation from the linear function (green line) and is well fit by the Kurtosis model (black line).

Compared to the Gaussian diffusion model in Eq. 2.5, the diffusion kurtosis model includes a b^2 term from the cumulant expansion of diffusion weighted signal attenuation $\ln(S(b)/S_0)$:

$$\ln(S(b)/S_0) = -bD + \frac{1}{6}b^2 D^2 K + O(b^3) \qquad (2.15)$$

where $S(b)$ is the diffusion weighted signal and S_0 is the non-diffusion weighted signal. D is the diffusion coefficient and K is the diffusion kurtosis. Figure 2.12 (b) shows measured diffusion weighted signal attenuation $\ln(S(b)/S_0)$ that clearly deviates from the linear equation corresponding to the Gaussian model (green line) and is well fit by the diffusion kurtosis model (black line).

As diffusion is directional, the diffusion kurtosis also varies across directions being measured. Recall that directional diffusion can be captured by a 2nd order symmetric 3×3 diffusion tensor **D** with 6 independent components. Directional diffusion kurtosis can be captured by a 4th order 3×3×3×3 tensor **W**. Being fully symmetric, the 81-element kurtosis tensor **W** has 15 independent elements. So, in order to fully estimate **D** and **W**, a minimum of two b-values beyond $b = 0$ s/mm^2 and a minimum of 15 diffusion directions must be acquired (Lu et al., 2006).

The apparent diffusion coefficient and apparent diffusion kurtosis measured along a specific diffusion direction $\mathbf{g} = [g_1, g_2, g_3]$ are usually referred to as $D_{app}(\mathbf{g})$ and $K_{app}(\mathbf{g})$. Their relationships to the diffusion tensor **D** and kurtosis tensor **W** are:

$$D_{app}(\mathbf{g}) = \sum_{i=1}^{3}\sum_{j=1}^{3} g_i g_j D_{ij} \tag{2.16}$$

$$K_{app}(\mathbf{g}) = \frac{MD^2}{D_{app}(\mathbf{g})^2}\sum_{i=1}^{3}\sum_{j=1}^{3}\sum_{k=1}^{3}\sum_{l=1}^{3} g_i g_j g_k g_l W_{ijkl} \tag{2.17}$$

where D_{ij} are elements in **D**, and W_{ijkl} are elements in **W**. MD is the mean diffusivity and can be calculated from:

$$MD = \frac{1}{3}\sum_{i=1}^{3} D_{ii} \tag{2.18}$$

2.3.4 Diffusion Kurtosis Derived Parameters

As the kurtosis tensor **W** is a 4th order tensor, there are many eigenvalues and eigenvectors associated with it, corresponding to the full 3D characteristics of **W** (Qi et al., 2008). An interpretation of these parameters has yet to be explored. More commonly used diffusion kurtosis imaging (DKI) parameters are those that have more direct physical relevance to the diffusion tensor (Cheung et al., 2009; Hui et al., 2008; Wu and Cheung, 2010):

1) Mean Kurtosis (MK)

Mean kurtosis (*MK*) is computed as the average kurtosis along all diffusion directions. If there are *N* uniformly distributed diffusion directions, then *MK* is commonly estimated as:

$$MK = \frac{1}{N}\sum_{i=1}^{N}(K_{app})_i \tag{2.19}$$

2) Axial Kurtosis (K_a) and Radial Kurtosis (K_r)

Directional diffusion kurtosis can also be examined along the axial and radial directions of the diffusion tensor. To compute it, the kurtosis tensor **W** is first transformed to the co-ordinate system defined by the three eigenvectors ($\mathbf{v_1}$, $\mathbf{v_2}$, $\mathbf{v_3}$) of the diffusion tensor **D**.

$$\hat{W}_{ijkl} = \sum_{i'=1}^{3}\sum_{j'=1}^{3}\sum_{k'=1}^{3}\sum_{l'=1}^{3} e_{i'i}e_{j'j}e_{k'k}e_{l'l}W_{i'j'k'l'} \tag{2.20}$$

Where e_{ij} are elements of the 3D rotation matrix P ($P = (\mathbf{v_1}, \mathbf{v_2}, \mathbf{v_3})$). The diffusion kurtosis along each of the eigenvectors is related to the eigenvalues $\lambda_1, \lambda_2, \lambda_3$ of the diffusion tensor and the mean diffusivity MD as:

$$K_i = \frac{MD^2}{\lambda_i^2} \hat{W}_{iiii}, \quad i = 1,2,3 \tag{2.21}$$

The axial and radial kurtosis is then calculated analogously to the axial and radial diffusivity as:

$$K_a = K_1 \tag{2.22}$$

$$K_r = \frac{K_2 + K_3}{2} \tag{2.23}$$

<u>3) Anisotropy of Kurtosis (FA_k)</u>

As a similar measure to FA in DTI, a measure of anisotropy of diffusion kurtosis can be defined as:

$$FA_k = \frac{\sqrt{3[(K_1 - \overline{K})^2 + (K_2 - \overline{K})^2 + (K_3 - \overline{K})^2]}}{\sqrt{2(K_1^2 + K_2^2 + K_3^2)}} \tag{2.24}$$

where $\overline{K} = \frac{1}{3}\sum_{i=1}^{3} K_i$. Note that $\overline{K} \neq MK$ because the 3D kurtosis distribution cannot be represented by a simple ellipsoid.

Equations (2.19) to (2.23) are commonly used formulas to calculate the kurtosis-related parameters. They are derived analogous to DTI parameters. As the diffusion kurtosis represent a more complex 3D structure, a more rigorous formula has been derived that takes a surface integral when calculating MK and K_r (Jensen and Helpern, 2010; Tabesh et al., 2010). For example, *MK* can be expressed as a surface integral of K_{app}s over a unit sphere $\Omega_{\mathbf{g}}$:

$$MK = \frac{1}{4\pi}\int K_{app}(\mathbf{g})d\Omega_{\mathbf{g}} \ . \tag{2.25}$$

Explicit formulas for *MK* and K_r in terms of surface integral are given by Jensen (Jensen and Helpern, 2010). They are referred to as MK_s and K_{rs} here so as to be differentiated from Eq. 2.19 and 2.23.

$$\begin{aligned} MK_s &= F_1(\lambda_1,\lambda_2,\lambda_3)\hat{W}_{1111} + F_1(\lambda_2,\lambda_1,\lambda_3)\hat{W}_{2222} + F_1(\lambda_3,\lambda_2,\lambda_1)\hat{W}_{3333} \\ &+ F_2(\lambda_1,\lambda_2,\lambda_3)\hat{W}_{2233} + F_2(\lambda_2,\lambda_1,\lambda_3)\hat{W}_{1133} + F_2(\lambda_3,\lambda_2,\lambda_1)\hat{W}_{1122} \end{aligned} \tag{2.26}$$

where $\hat{W}_{ijkl}$ are components of the kurtosis tensor **W** in a coordinate system defined by the eigenvectors of the diffusion tensor **D** as explained before. We have:

$$F_1(\lambda_1,\lambda_2,\lambda_3) = \frac{(\lambda_1+\lambda_2+\lambda_3)^2}{18(\lambda_1-\lambda_2)(\lambda_1-\lambda_3)}\left[\frac{\sqrt{\lambda_2\lambda_3}}{\lambda_1}R_F\left(\frac{\lambda_1}{\lambda_2},\frac{\lambda_1}{\lambda_3},1\right) + \frac{3\lambda_1^2-\lambda_1\lambda_2-\lambda_2\lambda_3-\lambda_1\lambda_3}{3\lambda_1\sqrt{\lambda_2\lambda_3}}R_D\left(\frac{\lambda_1}{\lambda_2},\frac{\lambda_1}{\lambda_3},1\right)-1\right] \tag{2.27}$$

$$F_2(\lambda_1,\lambda_2,\lambda_3) = \frac{(\lambda_1+\lambda_2+\lambda_3)^2}{3(\lambda_2-\lambda_3)^2}\left[\frac{\lambda_2+\lambda_3}{\sqrt{\lambda_2\lambda_3}}R_F\left(\frac{\lambda_1}{\lambda_2},\frac{\lambda_1}{\lambda_3},1\right) + \frac{2\lambda_1-\lambda_2-\lambda_3}{3\sqrt{\lambda_2\lambda_3}}R_D\left(\frac{\lambda_1}{\lambda_2},\frac{\lambda_1}{\lambda_3},1\right)-2\right] \tag{2.28}$$

where R_f and R_d represent Carlson's elliptic integrals (Carlson, 1979).

The radial kurtosis is calculated as:

$$K_{rs} = G_1(\lambda_1,\lambda_2,\lambda_3)\hat{W}_{2222} + G_1(\lambda_1,\lambda_3,\lambda_2)\hat{W}_{3333} + G_2(\lambda_1,\lambda_2,\lambda_3)\hat{W}_{2233} \tag{2.29}$$

where

$$G_1(\lambda_1,\lambda_2,\lambda_3) = \frac{(\lambda_1+\lambda_2+\lambda_3)^2}{18\lambda_2(\lambda_2-\lambda_3)^2}\left[2\lambda_2 + \frac{\lambda_3^2-3\lambda_2\lambda_3}{\sqrt{\lambda_2\lambda_3}}\right] \tag{2.30}$$

$$G_2(\lambda_1,\lambda_2,\lambda_3) = \frac{(\lambda_1+\lambda_2+\lambda_3)^2}{3(\lambda_2-\lambda_3)^2}\left[\frac{\lambda_2+\lambda_3}{\sqrt{\lambda_2\lambda_3}} - 2\right] \tag{2.31}$$

2.3.5 What Does Diffusion Kurtosis Mean?

Diffusion kurtosis has been described as a measure for tissue complexity or tissue heterogeneity (Jensen and Helpern, 2010). Consider a voxel that contains multiple compartments: each has their own volume fraction f_m and diffusion coefficient D_m, as shown in Figure 2.13. Then the diffusion coefficient D of the whole voxel is a weighted averaged of the compartmental diffusion coefficient, while the kurtosis K is proportional to the variance of the diffusion coefficients (Jensen and Helpern, 2010). Higher complexity or heterogeneity in the tissue will cause a higher variability in diffusion coefficient and hence leads to higher kurtosis.

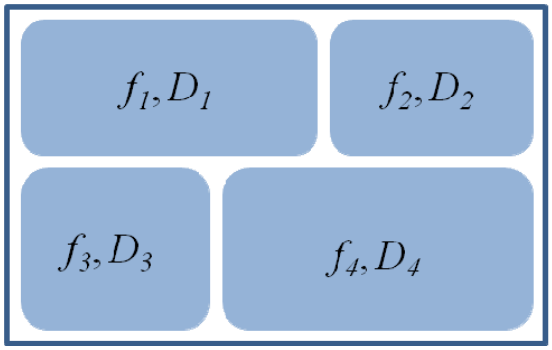

$$D = \sum_{m=1}^{4} f_m D_m$$

$$K = 3\frac{\sum_{m=1}^{4} f_m (D_m - D)^2}{D^2}$$

Figure 2.13. Diffusion coefficient and kurtosis in a multiple compartment model.

Figure 2.14 shows an illustration of the kurtosis distribution corresponding to the diffusion distribution in brain tissues. If diffusion is modeled as an ellipsoid with its principle direction (defined by $\mathbf{v}_1$) pointing along the white matter axons, then the kurtosis distribution will be like a pancake shaped ellipsoid. The kurtosis is low in the axial direction of the diffusion ellipsoid (defined by $\mathbf{v}_1$) because diffusion is most freely along the axons, resulting in a more Gaussian diffusion displacement distribution. The kurtosis is high in the radial direction of the diffusion ellipsoid (the plane spanned by $\mathbf{v}_2$ and $\mathbf{v}_3$) because movement of the water molecules is highly heterogeneous due to the myelin sheaths and cell membranes, etc., resulting in a highly non-Gaussian displacement distribution. Note, though, that the representation of kurtosis distribution by an ellipsoid is a simplified view of a more complex structure defined by the 4th order kurtosis tensor.

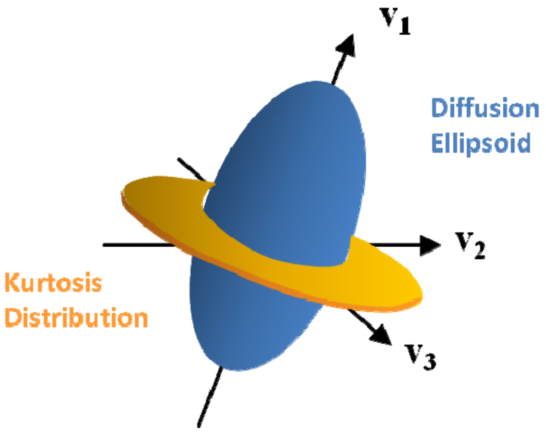

Figure 2.14. An illustration of the diffusion and kurtosis distribution in the 3D system defined by diffusion eigenvectors ($\mathbf{v}_1$, $\mathbf{v}_2$, $\mathbf{v}_3$). The diffusion distribution is an ellipsoid (blue) with the principle direction pointing at $\mathbf{v}_1$. The kurtosis distribution, from a simplified point of view, is like a pancake (yellow) with higher kurtosis along radial direction of the diffusion ellipsoid, indicating restricted diffusion.

The diffusion kurtosis properties in the brain can be inferred from DTI-related parameters. Figure 2.15 shows DTI and DKI derived parameter maps in human and rat brains. In white matter, MK is high, indicating a generally higher tissue complexity in an environment of densely packed axons. K_r is high (and λ_r is low), reflective of highly heterogeneous and restrictive diffusion perpendicular to the axon direction. In grey matter and CSF, due to the isotropic diffusion property, kurtosis is also non-directional. FA_k and

FA generally present the same information, as regions with highly anisotropic diffusion will also have a highly anisotropic kurtosis distribution (although FA_k is noisier than *FA* due to the more complex structure of the kurtosis tensor).

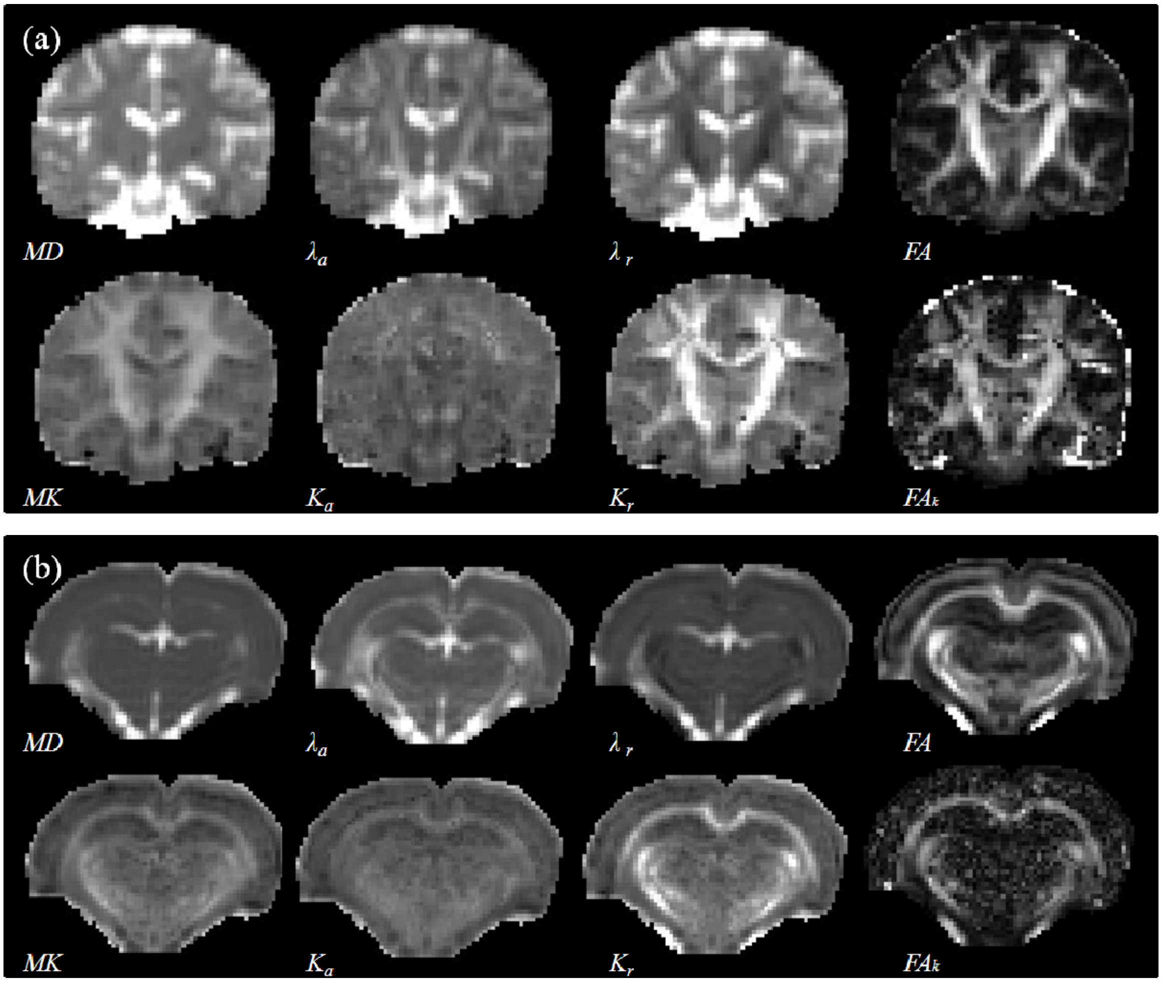

Figure 2.15. DTI and DKI related parameters in the human brain (a) and the rat brain (b).

2.3.6 DKI Applications in Neural Tissue Characterization

Although DKI is a relatively new imaging method and there have only been a limited number of studies utilizing DKI, kurtosis parameters have been shown to potentially have higher sensitivity in characterizing neural tissues than DTI. Cheung et al. found that DKI parameters were more sensitive to the developmental changes in the rat than conventional DTI parameters (Cheung et al., 2008). Falangola et al. reported age related *MK* changes in grey matter, which has never before been reported in DTI aging studies (Falangola et al., 2008). Grey matter *MK* values have also been shown to correlate with cognitive function in chronic TBI patients (Grossman et al., 2011) and adolescents with ADHD (Helpern et al., 2011). Furthermore, DKI has been applied in head and neck squamous cell carcinoma (Jansen et al., 2010) and cerebral gliomas (Raab et al., 2010), indicating a higher predictive value of kurtosis measures to patient outcome than conventional DTI measures.

Chapter 3. Diffusion Kurtosis as an *In Vivo* Imaging Marker for Reactive Astrogliosis in Traumatic Brain Injury

3.1 Introduction

Understanding tissue alterations at an early stage following traumatic brain injury (TBI) is critical for injury management and prevention of more severe secondary damage to the brain. Diffusion tensor imaging (DTI) is a powerful tool for studying neurological disease as it provides *in vivo* measurements of tissue microstructure change that could not otherwise be detected through conventional magnetic resonance imaging (MRI) techniques. Studies using DTI have focused on white matter abnormality because of the highly directional diffusion of water found in the white matter tracts. In acute brain injuries, a reduced *MD* and/or increased *FA* has been equated with cellular swelling (cytotoxic edema) or increased cell density, leading to a reduced extra-cellular space (Armitage et al., 2008; Bazarian et al., 2007; Shanmuganathan, 2004). At the same time, an increased *MD* and/or reduced *FA* has been equated with cellular membrane disruption, cell death, tissue cavitation, or vasogenic edema, which leads to an increased extra-cellular space as seen in patients with chronic brain injury (Cercignanti et al., 2001; Warring et al., 2000; Zelaya et al., 1999). Since the diffusion profile in the grey matter is considered to be largely isotropic (Pierpaoli et al., 1996), the use of DTI to study changes in the gray matter in brain injury has unfortunately received very little interest.

The diffusion of water in brain tissue, while complex, is largely simplified in the DTI model where the diffusion-weighted signal '*S*' is assumed to follow a mono-exponential decay. Typically for routine clinical evaluation, the b-values in DTI experiments are around 1000 s/mm^2 and can probe a minimum diffusion distances of about 5-10μm (Assaf and Cohen, 2000). While this model is routinely used in the clinic, the model breaks down when higher b-values are used and the diffusion gradients are sensitized to probe restricted diffusion over shorter molecular distances (Assaf and Cohen, 1998; Niendorf et al., 1996). At such short molecular distances, the signal decay seen from diffusion-weighted imaging may deviate from mono-exponential decay as the technique becomes sensitive to even shorter molecular distances and increasingly sensitive to heterogeneous cellular structures. This deviation from mono-exponential decay of the diffusion signal can potentially reveal more information about tissue microstructure changes, especially in structures such as the gray matter, tumor micro-environment (Raab et al., 2010), in regions of neurodegeneration (Farrell et al., 2010), and post traumatic tissue (Jiang et al., 2011), where heterogeneity may prevail.

The diffusion kurtosis model uses a cumulant expansion of ln(S) in a power series of b to fit the diffusion weighted signal. This model makes no presumption of compartmentalization and has shown to fit the diffusion-weighted signal well, up to moderately large b-values of around 2500 s/mm^2. Using this model, Diffusion Kurtosis Imaging (DKI) has shown great promise to better characterize grey matter microstructure change in rodent brain maturation (Cheung et al., 2008; Hui et al., 2008; Wu et al., 2010) and in human brain aging (Falangola et al., 2008). Diffusion kurtosis has also shown to have clinical value in detecting tissue microstructure abnormality such as in squamous cell carcinoma (Jansen et al., 2010), cerebral gliomas (Raab et al., 2010), and lung dysfunction (Trampel et al., 2006). More specifically, diffusion kurtosis has been described as an imaging marker that captures brain tissue complexity (Jensen et al., 2010; Shaw, 2010). Falangola et al., (2008) reported increased grey matter kurtosis with age, when moving from adolescence to adulthood, and attributed this increase to cortical cell-packing density, continuing myelination and an overall increase of the microstructural complexity in the brain. Earlier papers had determined the increased microstructural complexity with age to be related to increased activity of glial cells, which have a more complex cell structure than neurons (Terry et al., 1987). On the other hand, increased glial cell activity, or more specifically reactive astrogliosis, has long been used as reliable and sensitive pathology hallmark for diseased tissue in the central nervous system and for determining long-term clinical outcome from central nervous system injury (Chen et al., 2003; Sofroniew, 2009; Sofroniew and Vinters, 2010). Given the sensitivity of diffusion kurtosis to changes in tissue microstructure and possibly inflammation as a result of glial and astrocytic proliferation following brain injury we hypothesize that it may play an important role in detecting inflammatory changes following TBI. To test this hypothesis, we investigated the utility of diffusion kurtosis and compared its performance to standard diffusion tensor imaging parameters by monitoring changes in these parameters in a controlled compact injury (CCI) rat model at the acute (2 hours) stage and the sub-acute (7 days) stage and compared the findings with the tissue histopathology.

3.2 Material and methods

3.2.1 *CCI TBI Model*

Adult male Sprague-Dawley rats (n=12, 250-350 grams) were subjected to left parietal CCI injury. Brain injury was induced using the controlled cortical impact device

(Pittsburgh Precision Instruments, Pittsburgh, PA) as previously described (Dixon et al., 1991) with modified settings. Briefly, after being anesthetized initially with 4% isoflurane, the rats were maintained at 2% isoflurane throughout the procedure. The left parietal bone was exposed via a midline incision in a stereotactic frame. A high-speed dental drill (Henry Schein, Melville, NY) was used to perform a left-sided 5 mm craniotomy that was centered 3.5 mm posterior and 4 mm lateral to bregma. A 5 mm round impactor tip was accelerated to 5 m/sec for an impact duration of 50 ms, resulting in a vertical deformation depth of 1.5 mm. The bone flap was immediately replaced with dental acrylic and the scalp incision was closed with silk. At the completion of surgery, isoflurane was discontinued, and rats were awakened and returned to their cages. Two additional sham rats (blank implanted) underwent identical surgeries, with the exclusion of the CCI. The experimental protocol was approved by the University of Maryland, Baltimore Institutional Animal Care and Use Committee.

3.2.2 *Imaging*

All experiments were performed on a Bruker Biospec 7.0 Tesla 30 cm horizontal bore scanner (Bruker Biospin MRI GmbH, Germany) equipped with a BGA12S gradient system capable of producing pulse gradients of 400 mT/m in each of the three axes, with AVANCE III electronics and interfaced to a Bruker Paravision 5.0 console. A Bruker ^1H 4-channel surface coil array was used as the receiver and a Bruker 72 mm linear-volume coil as the transmitter. At all times during the experiment, the animal was under 1-2% isoflurane anesthesia and 1 L/min oxygen administration. Ear pins were used to reduce head motion and improve consistency in head positions for each animal. An MR compatible small-animal monitoring and gating system (SA Instruments, Inc., New York, USA) was used to monitor the animal respiration rate and body temperature. The animal body temperature was maintained at 36-37^{o}C using a warm water bath circulation. The total duration of the whole experiment was approximately 2 hours. Each rat was imaged 1 day before injury and 2 hour post-injury. Seven of the twelve rats were also imaged at 7 days post-injury while the other five rats were sacrificed at 48 hours for histology for a separate study.

A three-slice (axial, mid-sagittal, and coronal) scout using rapid acquisition with fast low angle shot (FLASH) was used to localize the rat brain. A fast shimming procedure (Fastmap) was used to improve the B_0 homogeneity within a region of the object. Both proton density (PD) and T_2-weighted images were obtained using a 2D rapid acquisition with relaxation enhancement (RARE) sequence in both the axial and coronal plane. Imaging was performed over a 3 cm field of view (FOV) in the coronal plane with an in-plane resolution of 117μm using 24 slices at 1 mm thickness with no gap, at an effective echo-time of 18.9 ms for the proton density weighted image and an effective echo-time of 56.8 ms for the T_2-weighted image. The echo-train length for each of the echoes was 4 and the repeat time (TR) was 5500 ms with two averages for a total acquisition time of ~12 minutes. Imaging was also performed in the axial plane using the same imaging parameter as above but over a FOV of 3.0 x 3.2 cm^2.

For the DKI acquisition, diffusion weighted images were acquired with single shot, spin-echo echo-planar imaging (EPI) sequence. An encoding scheme of 30 gradient directions was used with the duration of each of the diffusion gradients (δ) being 4 ms with a temporal spacing of 23 ms (Δ) between the two diffusion gradients. Two b-values (1000 s/mm^2 and 2000 s/mm^2) were acquired for each direction following the acquisition of five images acquired at $b = 0$ s/mm^2. The DKI images were obtained using two averages using the same FOV and slice positions as the axial PD/T_2 images but at an in-plane resolution of 234 μm at a TR/TE of 6000/50ms respectively for a total acquisition time of about 13 minutes.

3.2.3 Histology

At seven days post-surgery, and after all imaging was complete, the seven rats were anesthetized with ketamine and transcardially perfused with 4% formaldehyde and 2.5% acrolein. The brains were extracted from the skull and placed in 30% sucrose. A freezing sliding microtome was used to obtain 35 μm brain sections. Sections were held at -20^{o}C prior to the immunohistochemistry procedure.

Each of the 35 μm sections was labeled with antibodies against glial fibrillary acidic protein (GFAP). Sections were rinsed multiple times with a 0.05 M KPBS buffer and then subjected to a 20 minute wash in a 1% solution of sodium borohydride and incubated in the primary antibody (anti-GFAP, 1:150K; Dako North America, Inc., Carpenteria, CA) diluted in 0.05 M KPBS + 0.4% Triton-X for 48 hours. They were then incubated for the secondary antibody (1:600), also diluted in 0.05 M KPBS + 0.4% Triton-X, for one hour. Sections were incubated in A/B solution (1:222) for one hour, and then in a Ni-DAB solution with a 0.175 M sodium acetate buffer for 12 minutes. Resulting slices were then mounted on slides, dehydrated, and cover-slipped with DPX mounting media. The sections were examined with a Leica (Nussloch, Germany) DMRX microscope equipped with a Phase One (Copenhagen, Denmark) Power Phase digital camera. Histology was also obtained from the two rats subject to sham injury.

3.2.4 Diffusion Reconstruction

Diffusion weighted (DW) images from individual averages were corrected first for motion artifacts using the 3dvolreg command in AFNI (Analysis of Functional NeuroImages, http://afni.nimh.nih.gov/afni; Cox, 1996). The two averages of motion/eddy-current corrected DW images were then averaged and spatially smoothed using a Gaussian filter with a FWHM of 0.3mm to increase the signal-to-noise ratio (SNR). DW signals from all three b-values (b = 0, 1000, 2000 s/mm^2) and 30 directions were then fitted voxel-wise using non-linear least squares fit to the equation:

$$\ln S(\mathbf{g},b)=\ln S_0-b\sum_{i=1}^{3}\sum_{j=1}^{3}g_ig_jD_{ij}+\frac{1}{6}b^2\sum_{i=1}^{3}\sum_{j=1}^{3}\sum_{k=1}^{3}\sum_{l=1}^{3}g_ig_jg_kg_lK_{ijkl} \tag{3.1}$$

where,

$\mathbf{g}=(g_1,g_2,g_3)$ is the unit-vector direction of the diffusion gradient.

$S(\mathbf{g},b)$ is the diffusion-weighted signal at a particular b value with direction **g**.

S_0 is the MR signal with no diffusion weighting (b = 0 s/mm^2) and is the average of all the five b=0 volumes that were acquired.

D_{ij} is element of the 3x3 diffusion tensor **D**.

K_{ijkl} is element of a 3x3x3x3 4th order tensor. K_{ijkl} is related to elements W_{ijkl} of the diffusion kurtosis tensor **W** and the mean diffusivity MD (mm^2/s) by:

$$K_{ijkl}=MD^2\cdot W_{ijkl} \tag{3.2}$$

Since **D** and **W** are both totally symmetric matrices, with 6 independent elements of the diffusion tensor and 15 independent elements for kurtosis tensor, a total of 21 parameters were fitted using Eq. 3.1. The apparent diffusion coefficient $D_{app}(\mathbf{g})$ and apparent kurtosis $K_{app}(\mathbf{g})$ for each direction **g** were then calculated from:

$$D_{app}(\mathbf{g}) = \sum_{i=1}^{3}\sum_{j=1}^{3} g_i g_j D_{ij} \tag{3.3}$$

$$K_{app}(\mathbf{g}) = \frac{1}{D_{app}(\mathbf{g})^2}\sum_{i=1}^{3}\sum_{j=1}^{3}\sum_{k=1}^{3}\sum_{l=1}^{3} g_i g_j g_k g_l K_{ijkl} \tag{3.4}$$

It should be noted that this is a slightly different approach than what has been proposed in previous published literature where $D_{app}(\mathbf{g})$ and $K_{app}(\mathbf{g})$ are fit for each direction and then fit for the diffusion tensor, **D** and kurtosis tensor, **W** (Cheung, 2009; Hui, 2008; Jensen, 2005; Lu, 2006; Wu, 2010). Our initial testing of these two approaches (Zhuo et al., 2011) indicated that fitting the tensors first resulted in less fitting errors and resulted in parametric maps that were less noisy. The improved DKI reconstruction method was described in more detail in Chapter 4.

Diffusion tensor related parameters (*MD*, *FA*, λ_a and λ_r) were calculated using Eq. 2.9-2.11. Kurtosis related parameters (*MK*, K_a, K_r) were calculated using the Eq. 2.20, 2.24, 2.27. Note the surface integrated version of K_r (Jensen and Helpern, 2010) were used due to its low susceptibility to noise as would be shown in Chapter 4.

3.2.4 ROI Analysis

To assess the effectiveness of the DTI and DKI parameters, several brain regions were selected. Manually drawn regions of interest (ROI) were placed ipsilateral and contralateral to the injury in the cortex (CTX), hippocampus (HC), external capsule (EC) and the corpus callosum (CC) on 2-3 consecutive slices at around Bregma 2.12mm – 4.52mm (Paxinos and Watson, 1986) as shown in Figure 3.1. These regions were defined on the *FA* images while using the T_2-weighted image for anatomic reference. Mean and standard deviation values from each of the ROI's from the diffusion and kurtosis paramtetric maps were then computed. For all regions, mean *M*D, *FA*, *MK* values were measured. For white matter regions (bilateral EC and CC), the paramaters λ_a, λ_r, K_a, and K_r were also measured.

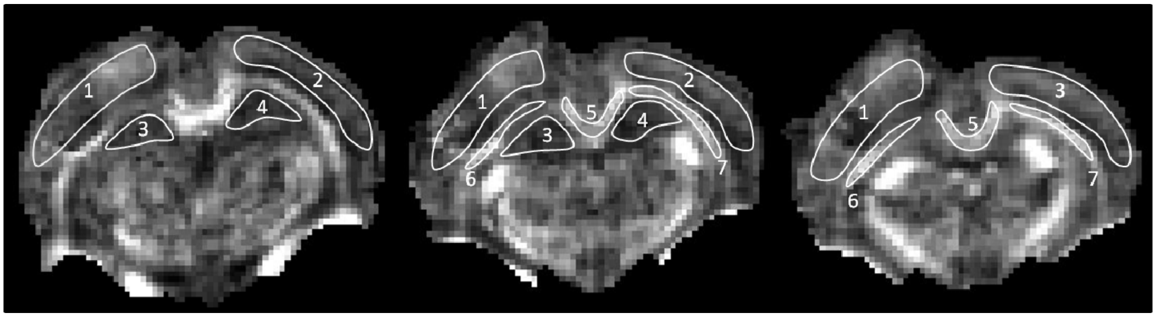

Figure 3.1. Illustration of ROIs on *FA* maps for a representative injured rat on three consecutive coronal slices. Regions shown are: ipsi- (1) and contra- (2) lateral cortex, ipsi- (3) and contra- (4) lateral hippocampus, corpus callosum (5), ipsi- (6) and contra- (7) lateral external capsule.

Note that voxels with $MK < 0$ or $MD > 1.5\times10^{-3}$ were excluded and did not contribute to the ROI. Negative *MK*s were dominantly observed in the cortex ipsilateral to the injury and were typically associated with extremely low diffusivities (or noise) or hemorrhage, leading to erroneous fit for K_{app} with a negative value. Rather than replacing the negative K_{app} values with zero, which does not accurately reflect the local water mobility environment, these pixels were ignored and did not contribute to the average value of any given ROI. Negative *MK*s were dominantly observed in the ipsilateral cortex region closer to the foci of the injury at the acute stage, leading to an exclusion of 2.2±2.8% of voxels (ranging from 0% to 11%) within the region. Similarly, because of our interest in the diffusion behavior of the surviving tissue, we used a *MD* threshold of $1.5\text{x}10^{-3}$ mm/s^2 to exclude very highly edematous regions given that the normal *MD* of the cortex is around $(0.82\pm0.04)\times10^{-3}$ mm/s^2. Visual observation of each rat showed that most of these voxels were only in the ipsilateral cortex at the sub-acute stage which resulted in the elimination of 22.8±20.7% of voxels (range of 0-60%) within the ROI.

3.2.5 Statistics Analysis

For each of the measured parameters (*FA, MD, MK,* λ_a, λ_r, K_a, and K_r depending on gray or white matter) and each ROI (CC and bilateral HC, CTX, EC), a mixed model ANOVA was performed with two degrees of freedom for time (fixed effect) and eleven degrees of freedom for subjects (rats) to test changes in the signal patterns with time for each of the measures using SAS 9.2. The significant P values from ANOVA were then corrected for multiple comparison across all parameters and ROIs using false discovery rate (FDR) (Benjamini and Hochberg, 1995) with a *q*(FDR) = 0.05. Following ANOVA, post-hoc tests with Tukey-Kramer correction were carried out to test for differences between the baseline and the different time points post-injury. All reported p values were corrected and statistical significance was deemed at $p < 0.05$.

3.3 Results

All the animals survived the seven day trial following the CCI injury. Parametric maps of diffusion tensor (*MD*, *FA*, λ_a, and λ_r) and kurtosis tensor (*MK*, K_a, K_r) were generated for each of the animals. Figure 3.2 shows *FA*, *MD* and *MK* maps from a representative rat before and after injury. All animals demonstrated a decreased *MD* and an increased *FA* at the site of injury at the initial time point which reversed by the sub-acute stage as seen by changes in *MD* and *FA* on their respective maps. Increased edema was also clearly observed in the *MD* maps, including the T_2-weighted images (not shown) on all animals by the sub-acute stage at the site of the injury. Increased *MK* was observed in and around the site of the injury in all animals at two hours post injury, followed by normalization by seven days but persisted diffusely surrounding the injury.

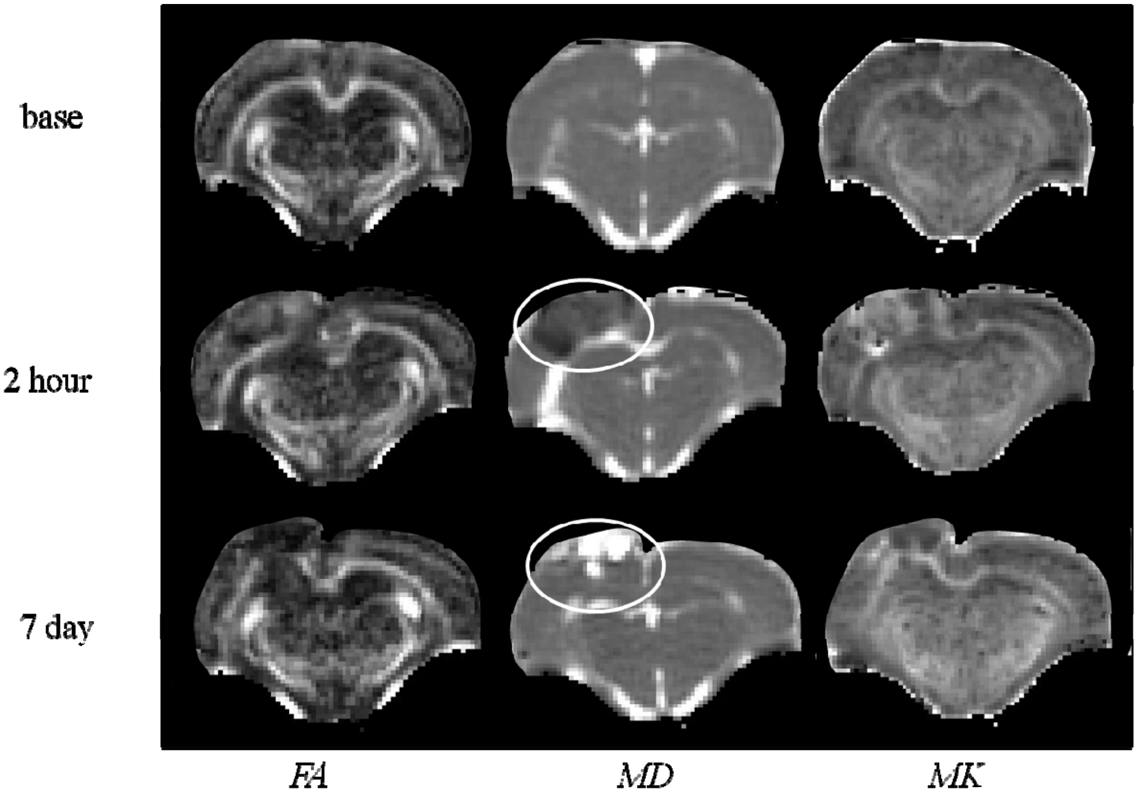

Figure 3.2. *FA*, *MD*, and *MK* maps of a representative rat in the coronal view at baseline (pre-injury), 2 hour and 7 days post injury. Circles indicate the site of injury.

3.3.1 DTI Changes Following CCI

Mixed model ANOVA revealed a significant temporal change in *MD* for bilateral hippocampus and cortex (HC_ips: $F_{2,11} = 50.31$, $p < 0.0001$; HC_con: $F_{2,11} = 16.69$, $p = 0.0007$; CTX_ips: $F_{2,11} = 70.98$, ; $p < 0.0001$; CTX_con: $F_{2,11} = 25.78$, $p < 0.0001$), where $F_{2,11}$ is the F-score using two degrees of freedom for the imaging time points and eleven degrees of freedom for subjects (rats). These regions experienced a significantly reduced *MD* ($p < 0.0005$) during the acute stage following CCI (Figure 3.3) that tended to return to baseline by the sub-acute stage. Only the CTX_ips demonstrated a significant increase in *MD* ($p = 0.031$) compared to the baseline suggesting significant edema in this region.

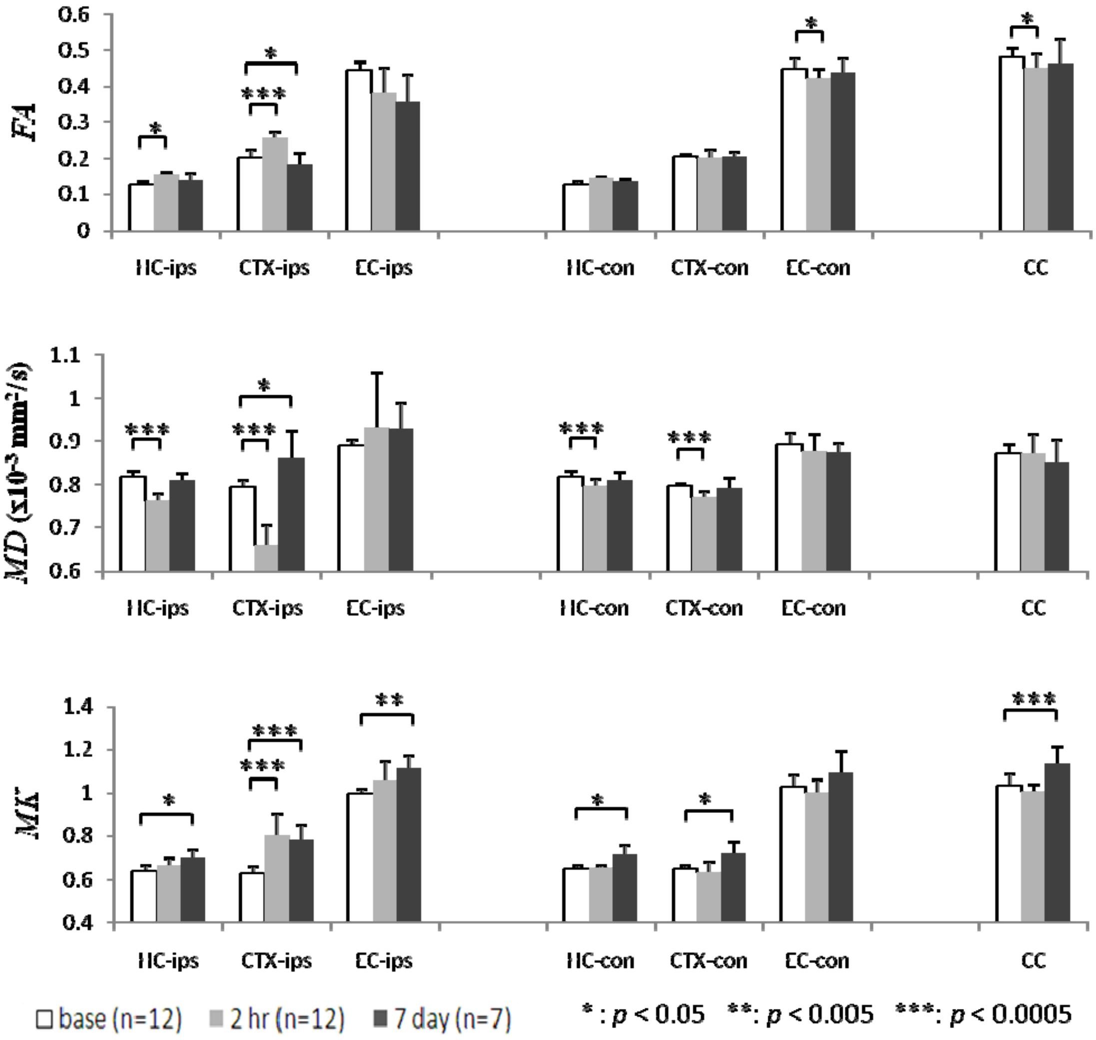

Figure 3.3. Changes in *MD*, *FA* and *MK* values for ipsilateral and contralateral hippocampus (HC-ips, HC-con), cortex (CTX-ips, CTX-con), external capsule (EC-ips, EC-con), and corpus callosum (CC) from baseline to 7 days post-injury. Statistical significance was based on comparison with baseline values. Error bars indicate standard deviation.

For *FA*, the time effect was significant for HC_ips ($F_{2,11} = 12.06$, $p = 0.0028$), CTX_ips ($F_{2,11} = 26.96$, $p < 0.0001$), EC_con ($F_{2,11} = 5.85$, $p = 0.03$) and CC ($F_{2,11} = 6.68$, $p = 0.02$). A significant increase in *FA* was observed in HC_ips ($p = 0.014$) and

CTX_ips ($p < 0.0001$), while a significant decrease in FA was observed in EC_con ($p = 0.011$) and CC ($p = 0.031$) at acute stage. These changes also returned to baseline levels by the sub-acute stage with the only exception being CTX_ips where a significant reduction of FA was observed compared to the acute stage ($p = 0.016$). The temporal change in FA within the EC_ips was near significant ($p = 0.08$) from ANOVA analysis but exhibited some variability probably due to the varying extent of injury between the rats at this site. Significant temporal changes for λ_a were observed in the EC_con ($F_{2,11} = 15.63$, $p = 0.001$) where λ_a was significantly reduced ($p = 0.0006$) at the acute stage which tended to return to the baseline by the sub-acute stage (Figure 3.4). Changes in λ_r were not significant in any region.

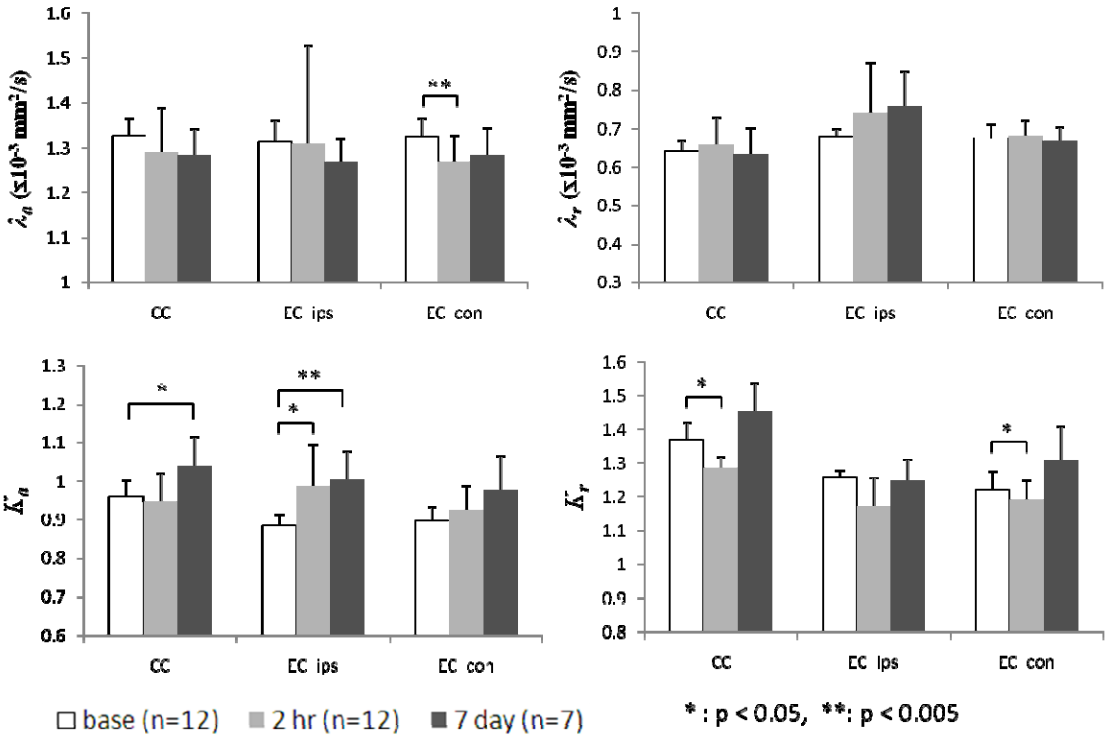

Figure 3.4. Changes in radial and axial diffusivity (λ_a, λ_r), and kurtosis (K_a, K_r) for white matter regions of corpus callosum (CC) and bi-lateral external capsule (EC_ips, EC_con) from baseline to 7 days post-injury. Statistical significance was based on comparison with baseline values. Error bars indicate standard deviation.

3.3.2 DKI changes following CCI

The ipsilateral regions of the hippocampus ($F_{2,11}$ = 6.27, *p* =0.025), cortex ($F_{2,11}$ = 31.72 *p* < 0.0001) and external capsule ($F_{2,11}$ = 8.66, *p* = 0.009) demonstrated a significant increase in *MK* over the seven days of observation. Only the contralateral hippocampus ($F_{2,11}$ = 11.47, *p* = 0.003) and the cortex ($F_{2,11}$ = 8.86, *p* = 0. 008) experienced significant increase in *MK* over seven days. Temporal *MK* changes in the CC were also significant ($F_{2,11}$ = 14.58, *p* = 0.02). Significant increase in *MK* was observed in the CTX_ips (*p* = 0.0002) at the acute stage, and trend towards an increase was also observed in the HC_ips (*p* = 0.09). The signal abnormality in different regions at the sub-acute stage appeared to scale inversely with the distance from the impacted site, where CTX-ips and CC showed the strongest increase in *MK* (p = 0.0002), followed by EC_ips (*p* = 0.003), HC_ips (*p* = 0.011), CTX_con (*p* = 0.032) and HC_con (*p* = 0.039).

Significant changes with time were observed for K_a, in the regions of EC_ips ($F_{2,11}$ = 12.11, *p* = 0.0028) and CC ($F_{2,11}$ = 6.66, *p* = 0.02). K_a was significantly increased in EC_ips (*p* = 0.013) at the acute stage and stayed elevated at sub-acute stage (*p* = 0.0032) as shown in Figure 3.4. The increase of K_a in CC on the other hand was significant only at the sub-acute stage (*p* = 0.0084).

The temporal changes in K_r were significant in all the three white matter regions (EC_ips: $F_{2,11}$ = 6.37, *p* = 0.024; CC: $F_{2,11}$ = 6.49, *p* = 0.023; EC_con: $F_{2,11}$ = 6.19, *p* = 0. 026). Significant reductions in K_r were observed in both the CC (p = 0.009) and EC_con (p = 0.01) at the acute stage which then returned to the baseline by the sub-acute stage (Figure 3.4). Similar trend was also observed in EC_ips (*p* = 0.07).

It should be noted that while *MD* was found to be a good discriminator of injury in the cortex and the hippocampus at the acute stage, it was unable to distinguish changes in these brain tissues at the sub-acute stage (HC_ips: p = 0.66; HC_con: p = 0.98; Cor_con: p = 0.97). However, *MK* was able to distinguish changes in the brain microstructure between the baseline and the sub-acute stage following injury, both in the gray and white matter regions. The increase in *MK* was also observed in the contralateral hippocampus and the cortex although to a lower extent.

3.3.3 Diffusion Kurtosis vs. Histology

Figure 3.5 shows histology using glial fibrillary acidic protein (GFAP) staining from two representative rats (Rat A and B) at the sub-acute stage post injury compared to a sham rat. Significantly increased GFAP immunoreactivity, indicated by increased number of astrocytes, is clearly present for both Rat A and B in the ipsilateral cortex and the hippocampus compared to the sham rat. For rat A, the contralateral side also showed an increased GFAP immunoreactivity, which was associated with increased *MK* values (not accompanied by *MD* values change), indicating that MK is sensitive to the changes associated with reactive astrogliosis. For rat B, the contralateral cortex had very low levels of GFAP staining that corresponded with low *MK* values.

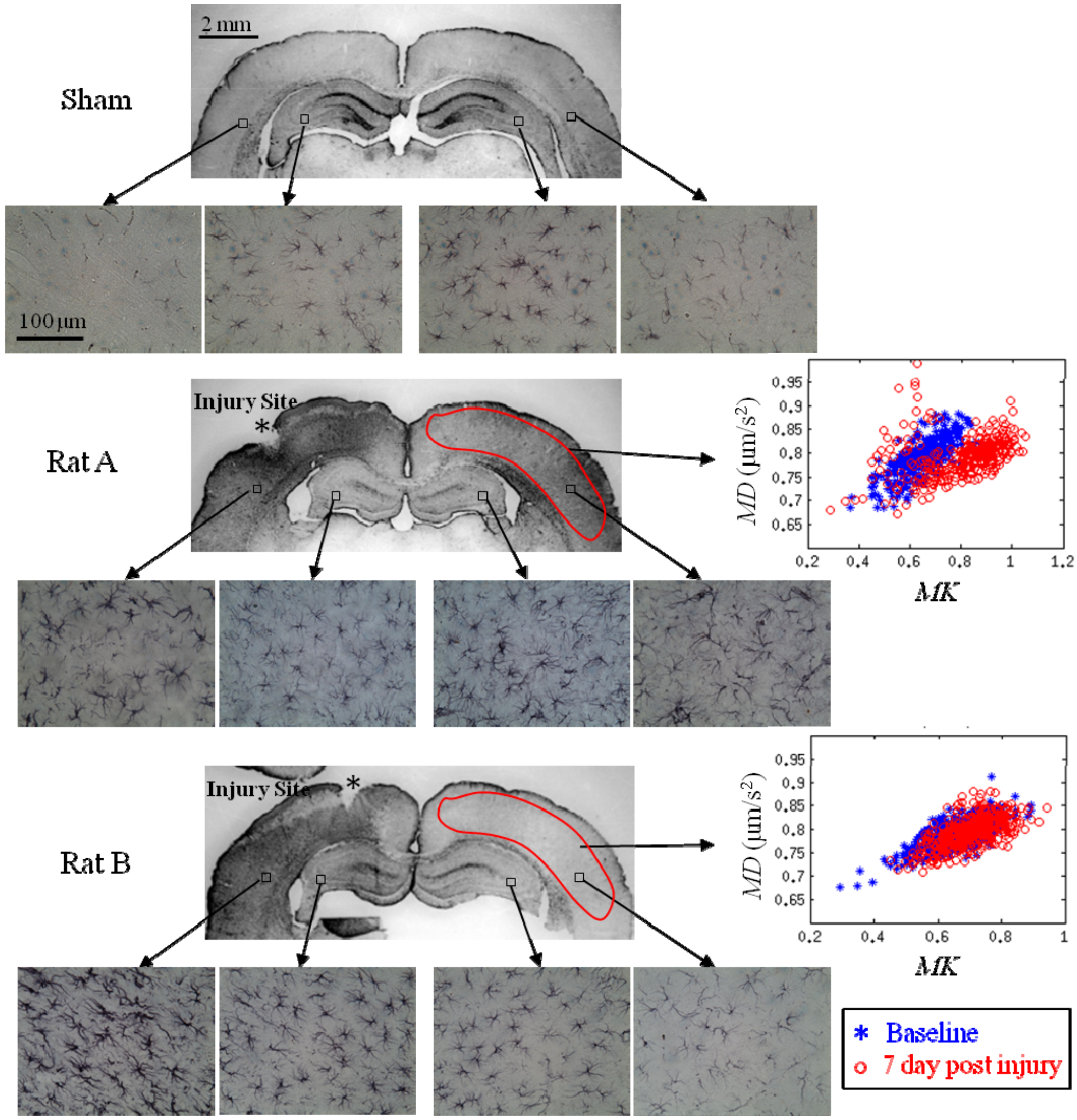

Figure 3.5. Comparison of immunohistochemical stains using glial fibrillary acidic protein (GFAP) two representative CCI exposed rats (Rat A and B) at 7 day post-injury and a sham rat. The GFAP stains (40× magnification) are shown from the ipsilateral cortex, hippocampus and contralateral hippocampus, cortex of each rat.

To assess the sensitivity of the various DTI/DKI parameters in detecting the abnormality far away from the foci of injury, the rats were divided into two groups based on the optical density in GFAP staining in the contralateral cortex. Two rats were found to have severe contralateral cortex staining (severe group, like rat A in Figure 3.5) and the other five were found to have mild staining in the contralateral cortex (mild group, like rat B in Figure 3.5). Figure 3.6 shows pair-wise scatter plots for *MD*, *FA* and *MK* (*FA* vs. *MD*, *MK* vs. *FA*, and *MD* vs. *MK*) values from all voxels within the contralateral cortex ROI of all rats in each group along with their respective histograms (20 bins, smoothed by 3 point moving average). The plot of *MK* vs. *MD* for the severe group (Figure 3.6a) for the *MK* values compared to the *MD* values between the voxels at baseline and the voxels from the sub-acute stage following injury indicating that *MK* is sensitive to changes associated with reactive astrogliosis. Similarly, an upward shift of *MK* peak is also seen while no shift is observed for *FA*. Figure 3.6b shows a similar pair-wise scatter plot for the mildly stained rats. No significant shifts of *MD, FA* or *MK* were observed in this group in the contralateral cortex. To compare the changes in voxel values between baseline and the sub-acute stage for the different parameters, standardized mean effect size was computed using Cohen's d (Cohen, 1988), which is defined as the difference between two means divided by the standard deviation of the data. In this test, an effect size of around 0.8 is considered large, an effect size of 0.5 as moderate and an effect size of 0.2 is considered small (Cohen, 1988). The effect size between the baseline voxels and the seven day voxels for the severe group was large for *MK* ($d_{eff,\, \boldsymbol{MK}} = 0.91$), moderate for *MD* ($d_{eff,\, \boldsymbol{MD}} = 0.46$) and none for *FA* ($d_{eff,\, \boldsymbol{FA}} = 0.03$). In the mild group, the two clusters of baseline and the sub-acute stage voxel values was not separable by the pair-wise plots, although the histogram indicating a slight shift of *MD* and *FA* toward lower values, while *MK* tended to be higher. However, the overall effect of all three parameters were small ($d_{eff,\boldsymbol{MD\&FA}} \approx 0.2$), with *MK* showing the largest effect ($d_{eff,\, \boldsymbol{MK}}$ =

0.35). Overall these results suggest that changes in *MK* are strongly associated with increased GFAP immunoreactivity.

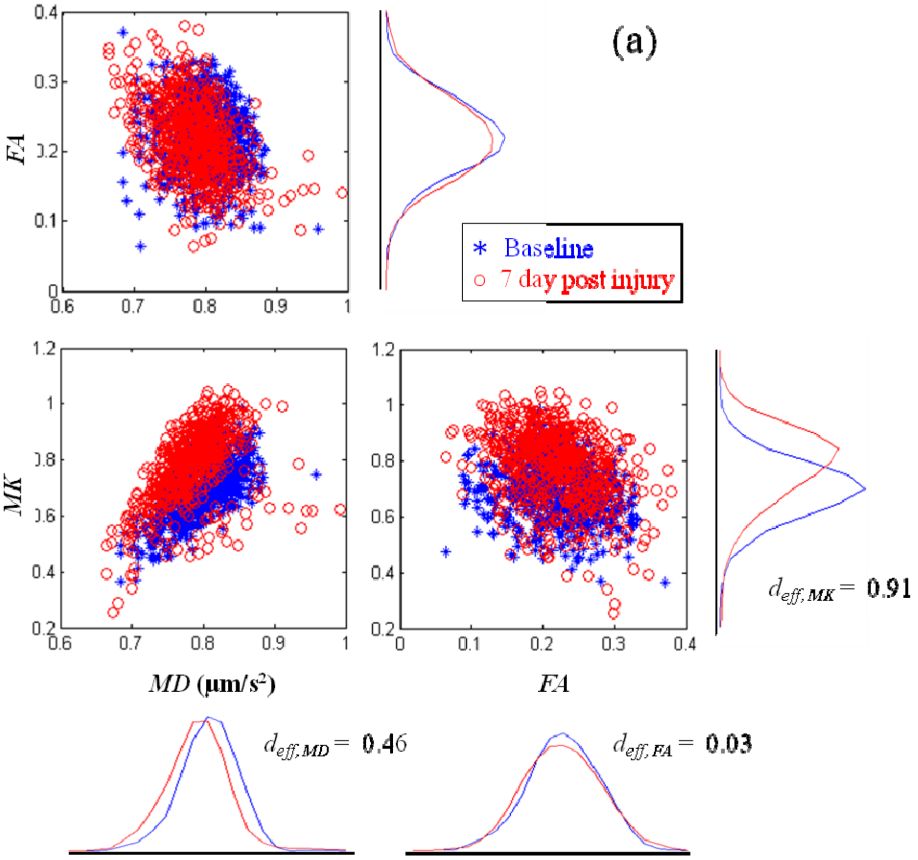

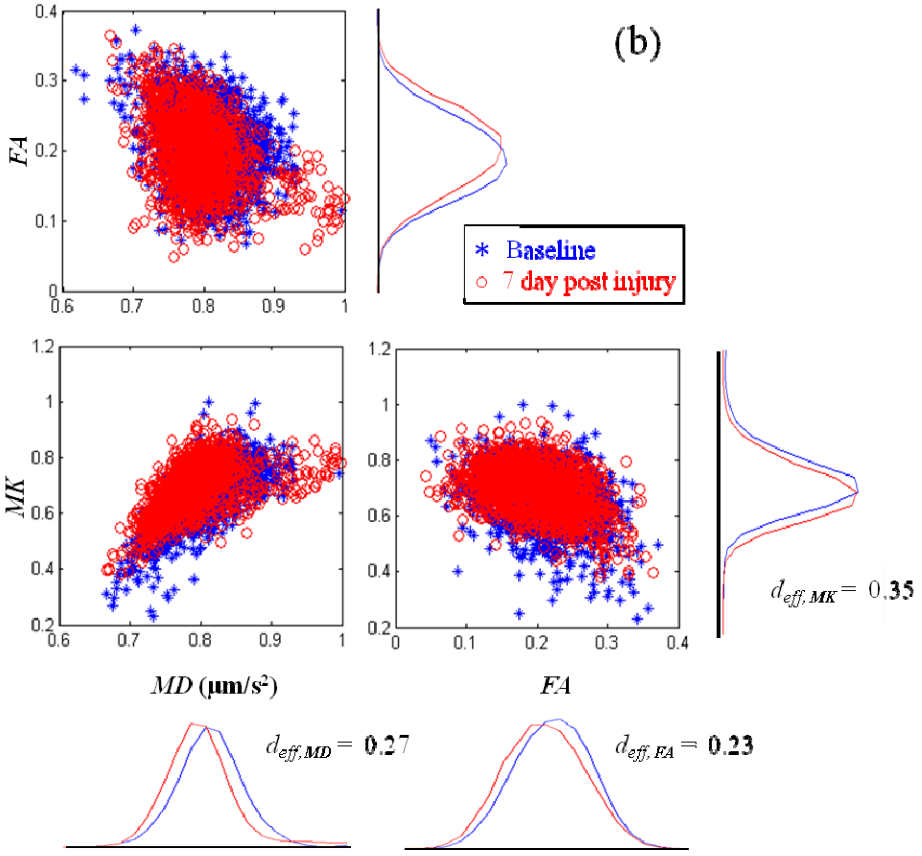

Figure 3.6. Pair-wise scattered plots of diffusion-related (*MD, FA*) and kurtosis-related (*MK*) parameters for voxels from an ROI on the contralateral cortex (see Figure 3.1) from groups of (a) severely and (b) mildly stained rats showing changes in these parameters at 7 days post injury (red dots) in comparison to the baseline (blue dots). The corresponding histograms for each of the parameters with the effect size d_{eff} are also shown.

3.4 Discussion

Diffusion-weighted MRI, and especially DTI, has long been shown to be a powerful tool in detecting tissue microstructure changes *in vivo*. However, the model most widely used inherently expects diffusion distances to have a Gaussian distribution, which can mask information regarding the underlying tissue heterogeneity. More recently, diffusion kurtosis has been described as an imaging marker that can provide information on tissue heterogeneity or tissue complexity (Jensen et al., 2010) and hence can reveal information beyond measures such as *MD* or *FA*. Our results indicate that diffusion kurtosis provides additional information not available through standard DTI parameters, and is sensitive to local tissue heterogeneity both in the gray and white matter following traumatic brain injury. More specifically, our study indicates a strong association with diffusion kurtosis and astrocytic immunoreactivity as revealed by the GFAP stains.

In a study of brain maturation, Falangola et al. (2008) have shown that *MK* is sensitive to changes in grey matter, where *MK* increases with brain maturation while the DTI parameters, *MD* and *FA* remained relatively unchanged. They postulated that the increase in *MK* during maturation in the grey and white matter was likely due to consistent and continuing myelination and an overall increase of the microstructural complexity and increased cell-packing density especially in the grey matter. Post-mortem studies also confirm the increase in the number and volume of glial cells with age in response to neuronal pruning as part of the developmental process of the nervous system (Finch, 2003; Terry et al., 1987). The combined effect of increased glial cell activity and neuronal pruning may essentially offset any changes in DTI parameters including *MD* and *FA*. However, this complex scenario of microstructural changes appears to be sensitive to *MK*.

Previous studies of brain injury have observed reactive astrogliosis activity to peak at 4-7 days post injury (Chen et al., 2003; MacDonald et al., 2007). This observation agrees with our histopathological findings where we observe significant increase in reactive astrocytosis and microglial response at 7 days. Furthermore, this increased reactive astrogliosis corresponds directly to the increased *MK* seen *in vivo* at sub-acute stage when DTI parameters such as *FA* and *MD* have returned to baseline, indicating that *MK* is sensitive to changes in tissue microstructure in response to the injury. Taken together, the results from DKI and histology confirm that *MK* is sensitive to the increased complexity of the tissue microstructure in response to the TBI.

Although the primary injury from CCI was focal, the pattern of injury as observed through DKI, especially at the sub-acute stage, was diffuse and even extended to the contralateral hemisphere. This finding is consistent with a previous study that found progressive neurodegeneration following CCI, starting at the site of the injury and gradually progressing to a widespread callosal and thalamic neuro-degeneration in both hemispheres by 7 days (Hall et al., 2005). The authors attributed this widespread change to degeneration of fibers in the corpus callosum and commissural pathway, causing progressive neuronal death and cellular destruction on the contralateral hemisphere. Reactive astrocytes are also known to have important neuroprotective roles after trauma in preserving neural tissue and restricting inflammation (Chen and Swanson, 2003; Laird et al., 2008; Myer, 2006). So such a process would also likely trigger mild reactive astrogliosis that might contribute to an increase in *MK* in the contralateral hemisphere. It is well known that reactive astrogliosis occurs in response to CNS injury and other disease process, the extent of which may vary based on the severity of the insult (Laird et al., 2008; Sofronview, 2009). These changes are modulated by inter- and intra-cellular signaling mechanisms and have the potential to modify the degree of changes in a manner that can be either detrimental or beneficial for the surrounding cells. The increased GFAP staining in the contralateral cortex for Rat A in Figure 3.5 at the sub-acute stage is indicative of mild to moderate reactive astrogliosis. Although some hypertrophy is observed without intermingling or overlapping of astrocyte domains, it is likely that such proliferation will eventually resolve and the astrocytes will return to their normal appearance (Sofroniew, 2010). Indeed this was the observation made by Chen et al. (2003) in a non-imaging study where a significant proliferation of reactive astrocytes was observed up to 7 days with eventual resolution to normal levels by 28 days post CCI.

The DTI changes in the white matter were more severe in regions adjacent to the direct impact compared to the remote regions in the contralateral hemisphere. A significant reduction in *FA* in the corpus callosum and the contralateral external capsule at the acute stage that returned to baseline by seven days was observed. Further, a trend towards a decrease in *FA*, driven by a reduction in λ_a was observed in the ipsilateral external capsule was observed. This behavior appears to be typical of CCI related axonal injury and is consistent with DTI studies in mice using the same injury model (MacDonald et al., 2007), as well as other diffuse axonal injury studies in human TBI s (Kraus et al., 2007; Mayer et al., 2010). It should be noted that the experimental injury used in our study was of only 1.5 mm impact depth compared to the more severe impact depth of 2.5 mm used by MacDonald et al. (2007). This might also explain the relatively milder changes in both λ_a, and λ_r in our study.

In the regions of the white matter, we also observed increased K_a and decreased K_r associated with decreased and increased diffusivity respectively in their respective directions. This may be due to broken and beading axons, which would cause more water diffusion restriction in the axial direction, leading to lower λ_a and higher K_a. These processes together with demyelination may result in more free water diffusion in the radial direction and hence higher λ_r and lower K_r. Moreover, the significant decrease of

K_r within CC and EC_con at the acute stage is accompanied by no changes in λ_r which further suggests that kurtosis is more sensitive to changes in intra- and extra- axonal water exchange (for example, in the case of axonal break-down and demyelination), as also suggested by Jensen (Jensen et al., 2010). The increase in K_a was also significant in the ipsilateral EC without a corresponding change in λ_a. This is probably due to the combined effect of axonal break-down and swelling in the tissue, which could effectively counterbalance, leading to no changes in *MD* (Figure 3.3), while increasing tissue heterogeneity would still lead to the observed increase in *MK* (Jensen et al., 2010). The increase in K_a and normalization of K_r at sub-acute stage can be attributed to reactive fibrous astrogliosis activity in the white matter.

DTI has been used extensively in characterizing white matter disease because diffusion properties along and perpendicular to the axon provide important information about axonal integrity. However, given the isotropic nature of grey matter, studies of microstructural imaging changes in the grey matter have been very limited. The fact that changes in the grey matter can be realized using *MK* provides an extra dimension to the repertoire of imaging techniques for the investigators. The directly impacted cortex shows an increased *MD* and reduced *FA* at the acute stage due to tissue edema, visible on T_2-weighted images. In the grey matter regions of the hippocampus and the cortex, we observed a reduced *MD* and increased *FA* at the acute stage. Similar DTI signal behavior has been reported in white matter regions, thalamus and at the whole brain level for TBI patients at the acute stage (Bazarian et al., 2007; Chu et al., 2010; Shanmuganathan et al., 2004; Wilde et al., 2008;) and has been attributed to cell swelling and cytotoxic edema. By the sub-acute stage a return to the baseline for *MD* and *FA* was observed in all these regions. Similar patterns of changes in *MD*/*FA* at an early and late stage were reported in a longitudinal study of mild TBI patients at 12 days post injury and 3-5 months post-injury respectively (Mayer et al., 2010). Increased *MD* and/or reduced *FA* at the chronic stage has also been observed in both white matter and grey matter in human studies (Bensen et al., 2007; Kraus et al., 2007; Niogi et al., 2008; Wilde et al., 2006) and also in several animal studies (Immonen et al., 2009; MacDonald et al., 2007).

Reliance purely on DTI parameters may underestimate the underlying cellular processes that influence changes in the tissue microstructure. In our study, the acute *MK* increase was only significant in the ipsilateral cortex and was directly associated with highly restricted diffusion as observed by *MD* in the directly impacted area. However, a wide spread increase in *MK* was observed by the sub-acute stage in other regions, at a time when both *MD* and *FA* appear to return to baseline levels. The increase in *MK* suggests increased tissue heterogeneity which was confirmed as reactive astrogliosis from GFAP staining. The normalization of *MD* and *FA* may reflect the ongoing activity of both detrimental and beneficial astrogliosis processes, the complexity of which is only reflected by changes in *MK*. Once again, this reflects the sensitivity of *MK* that is not captured by either *MD* or *FA* which underestimate the processes underlying tissue microstructure changes, when clearly reactive protoplasmic astrocytes have not completely resolved.

One limitation to the present study is that only GFAP staining was performed to obtain immunohistochemistry information on the animals. Although our study here clearly indicates an association of increased *MK* to increased reactive astrocyte activity from GFAP staining, one should not discount the possibility of other physiological processes that may also be in play that may have an effect on diffusion kurtosis. For example as indicated earlier, cellular destruction, edema, axonal breakage or demyelination, etc have been shown to be sensitive to diffusion-weighted imaging, and may also contribute to changes in diffusion kurtosis. While future studies should focus on teasing the contribution of these physiological processes, it is clear that diffusion kurtosis may have value in the case of mild injury where no focal contusion or lesion is observed on conventional MRI or can be identified by standard DTI parameters. Because of its sensitivity to changes in reactive astrogliosis, diffusion kurtosis may be a suitable imaging marker to monitor inflammatory changes in the brain following TBI.

The association of increased *MK* to increased astrocyte immunoreactivity in this study should be viewed in the context of its limitations. The sample size used in this study is small, especially at the sub-acute stage compared to the acute stage (only 7 out of 12 were imaged at 7 day post injury). Although we observed a strong association of changes in *MK* with GFAP immunoreactivity, it would be of great interest to see how *MK* correlates with histological findings, especially with the density of astrocytes within the injured tissue and the relationship with behavior and size of the contusion. It should be noted that reactive astrogliosis is believed to be a reliable and sensitive marker of diseased tissue (Sofroniew, 2010) and can play an important role in determining long-term clinical outcome (Cheng et al., 2003; Sofroniew, 2009). Another key limitation to our study is that we only followed the animals for 7 days. It would of interest to see if the *MK* tracks the normalization of the astrocytic activity over a longer period.

We only used three b-values primarily because of concern for the effects of prolonged anesthesia for the animals, potential for the animal to move during these prolonged experiments, and time constraints posed for magnet use. The reliability in the estimation of DKI parameters increases with the use of multiple b-values as it helps in minimizing fitting errors (Cheung et al., 2008; Falangola et al., 2008; Hui et al., 2008). However, more b-values will have little influence on the standard DTI parameters (Veraart et al., 2011). While the use of only three different b-values up to a maximum b-value of 2000 s/mm^2 may have led to some error in the estimation of the DKI parameters, such an acquisition has been suggested to be more practical in the clinical scenario (Jensen et al., 2010).

3.5 Conclusions

In summary, diffusion kurtosis parameters can provide additional microstructural information and complement the parameters from diffusion tensor imaging. Our study clearly indicates changes in diffusion kurtosis parameters correspond to active processes that involve reactive astrocytes not realized by other MR imaging techniques. Given that reactive astrogliosis is considered to be a reliable and sensitive biomarker for insults from traumatic brain injury and the fact that it can play an important role in determining the clinical outcome, we believe that DKI parameters are effective imaging markers to detect this activity *in vivo*.

Chapter 4. Improved Fast DKI Reconstruction

4.1 Introduction

Conventional fitting for Diffusion Kurtosis Imaging (DKI), as explained in section 2.3.3, typically uses a Levenber-Marquardt nonlinear fitting algorithm (Jensen et al., 2005). The apparent diffusion coefficient $D_{app}(\mathbf{g})$ and kurtosis $K_{app}(\mathbf{g})$ are fitted from each diffusion direction **g** according to equation:

$$\ln(S(b,\mathbf{g})/S_0) = -bD_{app}(\mathbf{g}) + \frac{1}{6}b^2 D_{app}{}^2 K_{app}(\mathbf{g}) \tag{4.1}$$

The diffusion tensor **D** and the kurtosis tensor **W** are then estimated by using linear least-squares fit to Eq. 2.16-17. A whole-brain dataset can take well more than 1 hour to process (Lu et al., 2006). This significantly limits the clinical application of DKI, as real-time reconstruction and visualization are highly desirable in a clinical environment.

A faster, but limited, DKI reconstruction algorithm was introduced by Jensen et al. (Jensen et al., 2009), which explicitly solves Eq. 4.1 for the diffusion coefficient D_{app} and kurtosis K_{app} when exactly 3 b-values (b_1, b_2, b_3) are used. Here, $S(b)$ and S_0 are diffusion weighted and non-diffusion weighted signals, respectively. D_{app} and K_{app} can be calculated using a closed-form expression:

$$D_{app} = \frac{(b_3+b_1)D^{(12)} - (b_2+b_1)D^{(13)}}{b_3-b_2} \tag{4.2}$$

$$K_{app} = 6\frac{D^{(12)} - D^{(13)}}{(b_3-b_2)D_{app}^2} \tag{4.3}$$

where

$$D^{(12)} = \frac{\ln[S(b_1)/S(b_2)]}{b_2 - b_1}, \quad D^{(13)} = \frac{\ln[S(b_1)/S(b_3)]}{b_3 - b_1} \tag{4.4}$$

Jensen's fast DKI algorithm reduces post-processing speed to only a few seconds. But it also has the following limitations:

1. It only works for 3 b-values, but typically 4-5 b-values are used in DKI experiments.
2. The closed-form expression assumes the diffusion directions are exactly the same for different b-values. While this is typically true during data acquisition, after motion correction, which requires rotating the diffusion directions accordingly, this condition usually does not hold anymore.

Furthermore, although it is a common practice to fit the diffusion coefficient D_{app} in each diffusion direction first and then reduce to the diffusion tensor **D**, a similar approach for DKI reconstruction poses an over-fitting problem and can increase fitting errors for this much more complex model. Fitting for D_{app} and K_{app} in each diffusion direction can add up to 60 parameters to fit for a common diffusion weighted (DW) imaging scheme of 30 diffusion directions, while the number of independent tensor parameter is only 21 (6 for the diffusion tensor and 15 for the kurtosis tensor).

A potential way of overcoming these obstacles arises from the fact that the DKI equation, when written in the tensor form, can also be easily transformed to a set of linear equations. They can then are solved by linear least squares fitting and result in a significantly reduced reconstruction time.

In this chapter, an improved tensor-based fast DKI reconstruction method, fDKI_T is described. It is compared to the conventional non-linear least squares method (referred to as NLS) (Jensen et al., 2005), as well the original fast DKI method (Jensen et al., 2009). A non-linear least squares version of the tensor-based DKI reconstruction (NLS_T) is also considered in order to assess the errors of going from non-linear DKI reconstruction to linear reconstruction. Analysis was performed on a set of rat-brain data, at both the whole-brain level and the region-of-interest (ROI) level, based on the accuracy of reconstructed parametric maps.

4.2 Methods

4.2.1 Theory

The diffusion tensor **D** and kurtosis tensor **W** can be estimated directly through the following equation after combining and rewriting the Eq. 4.1 and Eq. 2.16-17:

$$\ln\frac{S(\mathbf{g},b)}{S_0} = -b\sum_{i=1}^{3}\sum_{j=1}^{3} g_i g_j D_{ij} + \frac{1}{6}b^2\sum_{i=1}^{3}\sum_{j=1}^{3}\sum_{k=1}^{3}\sum_{l=1}^{3} g_i g_j g_k g_l K_{ijkl} \tag{4.5}$$

where,

$\mathbf{g} = (g_1, g_2, g_3)$ is the unit-vector in the direction of the diffusion gradient,

$S(\mathbf{g},b)$ is the diffusion-weighted signal at a particular b value with direction **g**,

S_0 is the MR signal with no diffusion weighting (b = 0 s/mm^2), and

D_{ij} is element (i,j) of the 3x3 diffusion tensor **D**.

K_{ijkl} is element (i,j,k,l) of the 3x3x3x3 4th order tensor **K**, which is related to the kurtosis tensor **W** and the mean diffusivity MD (measured in mm^2/s) by:

$$\mathbf{K} = MD^2 \cdot \mathbf{W} \tag{4.6}$$

By rewriting **D** and **W** in a vector format where:

$$D_v = [D_{11}, D_{22}, D_{33}, D_{12}, D_{13}, D_{23}], \tag{4.7}$$

$$K_v = [K_{1111}, K_{2222}, K_{3333}, K_{1112}, K_{1113}, K_{1222}, K_{2223}, K_{1333}, K_{2333}, K_{1122}, K_{1133}, K_{2233}, K_{1123}, K_{1223}, K_{1233}], \tag{4.8}$$

and defining a vector of monomials of the diffusion direction **g** that correspond to *D_v* and *K_v*, respectively:

$$g_d = [g_1^2, g_2^2, g_3^2, 2g_1g_2, 2g_1g_3, 2g_2g_3] \tag{4.9}$$

$$\begin{aligned} g_k = [&g_1^4, g_2^4, g_3^4, 4g_1^3g_2, 4g_1^3g_3, 4g_1g_2^3, 4g_2^3g_3, 4g_2g_3^3, 6g_1^2g_2^2, 6g_1^2g_3^2, 6g_2^2g_3^2, \\ &12g_1^2g_2g_3, 12g_1g_2^2g_3, 12g_1g_2g_3^2], \end{aligned} \tag{4.10}$$

Eq. 4.5 can then be transformed to a set of linear equations:

$$D_v \cdot g_d^{\ T} = \sum_{i=1}^{3}\sum_{j=1}^{3} g_i g_j D_{ij} \tag{4.11}$$

$$K_v \cdot g_k^{\ T} = MD^2 \sum_{i=1}^{3}\sum_{j=1}^{3}\sum_{k=1}^{3}\sum_{l=1}^{3} g_i g_j g_k g_l W_{ijkl}. \tag{4.12}$$

D_v and K_v can be easily solved through matrix division as:

$$\ln\frac{S(\mathbf{g},b)}{S(0)} = [-b, \frac{1}{6}b^2] \cdot \begin{bmatrix} Dv \cdot gd^T \\ Kv \cdot gk^T \end{bmatrix}. \tag{4.13}$$

D_{app} and K_{app} at a particular direction **g** can then be estimated by:

$$D_{app}(\mathbf{g}) = D_v \cdot g_d^{\ T} \tag{4.14}$$

$$K_{app}(\mathbf{g}) = \frac{K_v \cdot g_k^{\ T}}{D_{app}(\mathbf{g})^2} \tag{4.15}$$

All parametric maps can be calculated as discussed in section 2.3.4.

4.2.2 Data Acquisition

DKI data were collected on an adult male Sprague-Dawley rat. Imaging was performed on a Bruker Biospec 7.0 Tesla 30 cm horizontal bore scanner (Bruker Biospin MRI GmbH, Germany) equipped with a BGA12S gradient system capable of producing pulse gradients of 400 mT/m in each of the three dimensions (x, y and z), and interfaced to a Bruker Paravision 5.0 console. A Bruker ^{1}H 4-channel surface coil array was used as the receiver and a Bruker 72 mm linear-volume coil, as the transmitter. During the experiment, the animal was under 1-2% isoflurane anesthesia and 1 *L/min* oxygen administration. A MR compatible small-animal monitoring and gating system (SA Instruments, Inc., New York, USA) was used to monitor the animal respiration rate and body temperature. The animal body temperature was maintained at 36-37^o C using a warm water bath. Diffusion weighted images were acquired with a single shot spin-echo echo-planar imaging (EPI) sequence. A Bruker standard encoding scheme of 30 gradient directions was used with δ/Δ = 4/20 ms. Five non-zero b-values: 500, 1000, 1500, 2000, 2500 s/mm^2 were acquired for each direction following five images acquired at b = 0 s/mm^2. FOV = 3.0 × 3.0 cm^2, matrix resolution = 128 × 128, TR/TE = 6000/50 ms, slice thickness = 1 mm with no gap, number of slices = 24, number of averages = 2. The acquisition time is around 17 min. A proton density (PD) and T_2-weighted images were obtained using a 2D rapid acquisition with relaxation enhancement (RARE) sequence in the slice locations for anatomical reference. Imaging was performed over a 3 cm field of view (FOV) in the axial plane with an in-plane resolution of 117μm, at an effective echo-time of 18.9 ms for the proton density weighted image and an effective echo-time of 56.8 ms for the T_2-weighted image. The echo-train length for each of the echoes was 4 and the repeat time (TR) was 5500 ms with two averages for an acquisition time of around 12 minutes.

4.2.3 Post processing

1) Data Reconstruction

Diffusion weighted (DW) images from individual averages were corrected first for motion artifacts using the 3dvolreg command in AFNI (Analysis of Functional NeuroImages, http://afni.nimh.nih.gov/afni; Cox, 1996). Gaussian smoothing with a full width at half maximum (FWHM) of 0.3 mm was applied to the motion corrected DW images to increase the signal-to-noise ratio (SNR). The two repetitions were averaged first. Images from all 5 $b = 0$ s/mm^2 were then averaged as a b_0 volume. DW images from all five b-values ($b = 500, 1000, 1500, 2000, 2500$ s/mm^2) for 30 directions were fitted voxel-wise using the nonlinear least squares fitting of the tensor-based DKI (Eq. 4.5). DTI and DKI parameter maps (FA, MD, MK, K_a, K_r), as well as the surface integrated version of the mean and radial kurtosis (MK_s, K_{rs}), were generated as described in chapter 2.1.4 (Eq. 2.9-11) and 2.3.4 (Eq. 2.19, 2.22-23, 2.26-29) and used as the gold standard. Then, a subset of the full dataset with two non-zero b-values ($b = 1000, 2000$ s/mm^2) and the b_0 volumes were singled out as a short, and more clinically practical, protocol for voxel-wise fitting using:

1. The Conventional nonlinear least squares (NLS),
2. The fast DKI algorithm (fDKI),
3. The tensor based fast DKI algorithm (fDKI_T) algorithm as described in this chapter,

(4) The nonlinear least squares version of fDKI_T that fit for Eq. 4.5 directly (NLS_T).

DTI and DKI parameter maps were generated the same way as for the ground truth.

2) Error Analysis

The fitting error for different DKI reconstruction methods was first assessed at the whole brain level. A brain mask was manually drawn to exclude non-brain regions using MIPAV (Medical Image Processing, Analysis, and Visualization) application by NIH (http://mipav.cit.nih.gov) (McAuliffe et al., 2001). The percent error of each parameter compared to the gold standard was calculated voxel-wise using:

$$Error_i = \left|S_i - S_i^{gold}\right| \big/ S_i^{gold} \cdot 100\%, \qquad i \in [0, N] \tag{4.16}$$

where N is the total number of voxels within the brain mask. S_i and S_i^{gold} are values at voxel i of the image for a specific method, and the gold standard, respectively. The median error, as well as the 25th and the 75th percentile error values, were calculated to assess the overall error in using each method. Median error is more representative of a typical error value than mean error, since many of the statistics estimated here have strongly non-Gaussian error distributions with significant tails.

Since ROI analysis still remains the most common way of data analysis, the fitting error was further analyzed in several representative grey matter and white matter regions, to understand the effect of different reconstruction method on regional parameter values. Two grey matter regions: Cortex (CTX) and hippocampus (HC), and two white matter regions: Corpus Callosum (CC) and External Capsule (EC), were considered. ROIs were placed on 2-3 consecutive slices near Bregma 2.12mm – 4.52mm (Paxinos and Watson, 1986) as shown in Figure 4.1. These regions were defined on the *FA* images using the T_2-weighted image for anatomic reference. Regional fitting errors were calculated as the mean and standard deviation of voxel-wise errors ($Error_i$ in Eq. 4.16) within each region.

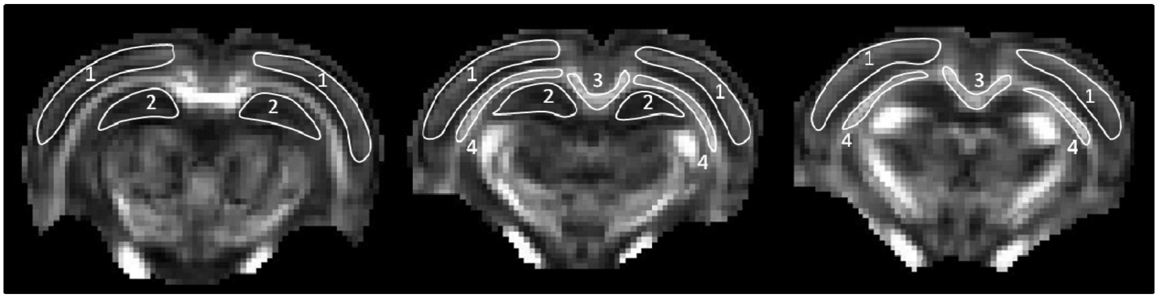

Figure 4.1. Illustration of ROIs on *FA* maps on three consecutive coronal slices. Regions shown are: (1) cortex (CTX), (2) hippocampus (HC), (3) corpus callosum (CC) and (4) external capsule (EC).

4.3 Results

Figure 4.2 shows *FA*, *MD*, *MK*, K_a, K_r, MK_s, and K_{rs} maps using all methods (NLS, fDKI, fDKI_T, NLS_T), compared to the gold standard. DTI derived parameters (*MD* and *FA*) show little visible difference among all the methods compared to the gold standard. The *FA* maps appear somewhat nosier for all methods when only two b-values are used, especially in the low *FA* regions like the hippocampus and the thalamus (yellow arrow). DKI derived parameters (*MK*, K_a, K_r, MK_s, K_{rs}) are noticeably noisier when only 2 b-values are used, compared to the gold standard. Little difference is observed for the *MK* and MK_s maps among different reconstruction methods. K_a, K_r and K_{rs} maps are less noisy for both the tensor based methods (fDKI_T and NLS_T) than either fDKI or NLS, with NLS showing slight improvement over fDKI, but with very little visible difference between fDKI_T and NLS_T. Between the surface integrated parameters (MK_s and K_{rs}) and the conventional ones (MK and K_r), no difference is observed for the mean kurtosis, but the radial kurtosis is much improved using the surface integration methods.

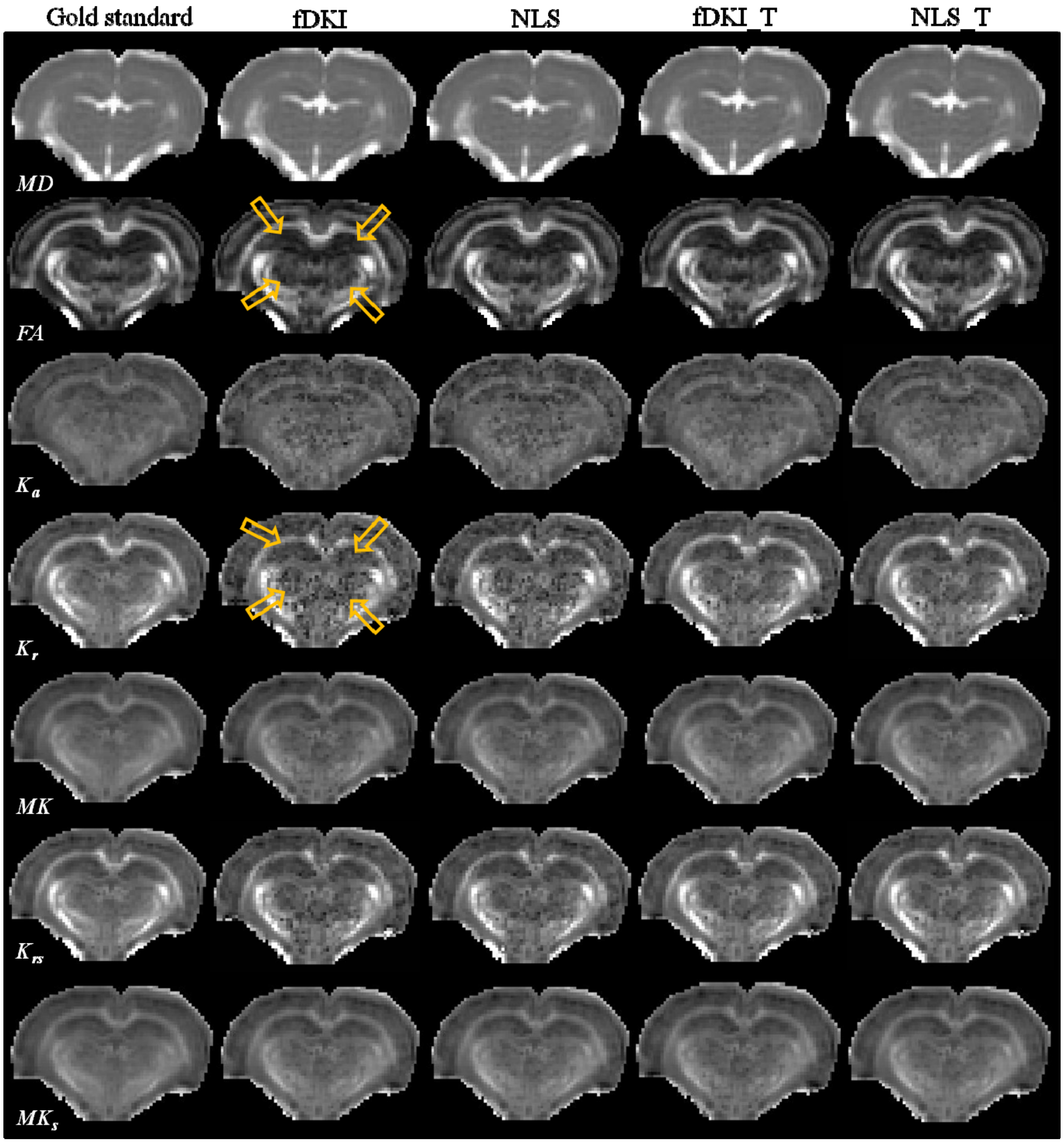

Figure 4.2. FA, MD, MK, K_a, K_r, MK_s, K_{rs} maps using the all methods (fDKI, NLS, fDKI_T, NLS_T), compared to the gold standard. Yellow arrows show specific regions (hippocampus and thalamus) that are more susceptible to noise.

Table 4.1 shows the median percent error calculated for all four methods (fDKI, NLS, fDKI_T, NLS_T) and all DTI and DKI parameters (*FA*, *MD*, *MK*, K_a, K_r, MK_s, K_{rs}). Figure 4.3 shows the same percent errors graphically and with confidence intervals (median error, with the 25th and the 75th percentile error indicated by the error bars). For DTI-related parameters (*MD* & *FA*), there is very little difference in estimation error among the different reconstruction methods. For DKI-related parameters (K_a, K_r, *MK*, K_{rs} and MK_r), the tensor-based methods (fDKI_T and NLS_T) perform significantly better than either fDKI or NLS, both because of smaller median error and less variability in error across brain voxels (75th–25th error). NLS produces overall smaller errors than fDKI, as expected by nonlinear fitting, but there is almost no difference between fDKI_T and NLS_T. Among all parameters, *MD* shows the least error across the brain; followed by *MK* and MK_s. K_{rs} has smaller errors than K_{rs} for all methods except fDKI. *MK* does not show any difference in errors compared to MK_s.

	fDKI	**NLS**	**fDKI_T**	**NLS_T**
MD	1.25	1.23	1.25	1.27
FA	7.61	7.56	7.61	7.58
MK	3.57	3.43	2.59	2.58
K_a	8.81	8.55	5.33	5.31
K_r	6.02	6.06	4.56	4.56
MK_s	3.58	3.47	2.59	2.57
K_{rs}	6.15	5.96	4.15	4.15

Table 4.1. Median percent error for all four methods (fDKI, NLS, fDKI_T, NLS_T) and all DTI and DKI related parameters (*FA*, *MD*, *MK*, K_a, K_r, MK_s, K_{rs}).

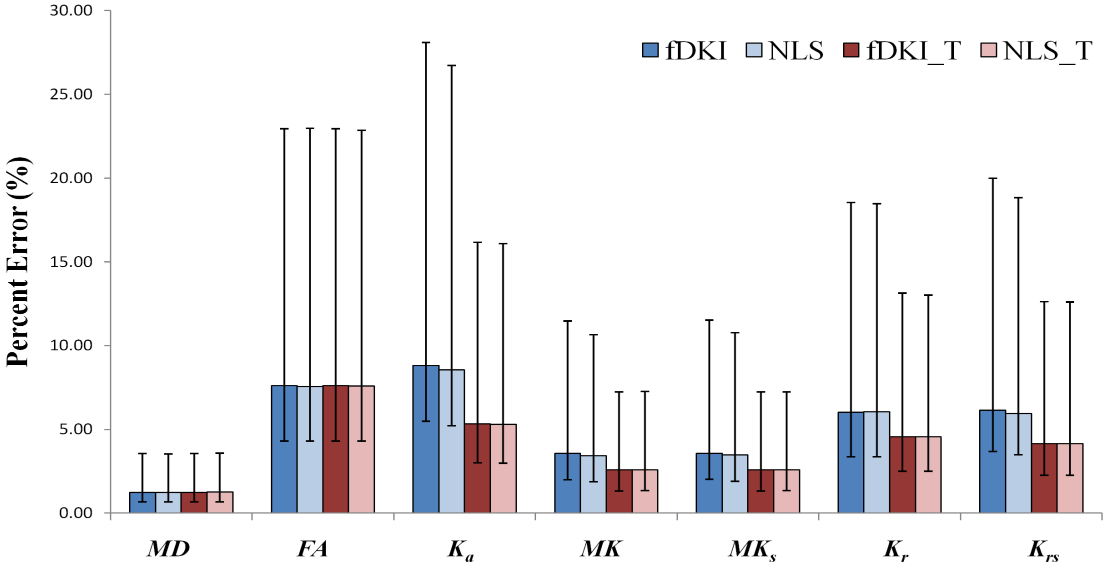

Figure 4.3. Median percent error for all four methods (fDKI, NLS, fDKI_T, NLS_T) and all DTI and DKI related parameters (FA, MD, MK, K_a, K_r, MK_s, K_{rs}). Error bars indicate the 25th and the 75th percentile values.

Figure 4.4 shows errors in DKI parameters (MK, K_a, K_r, MK_s, K_{rs}) for various regions. DTI parameters are not shown as there was little noticeable difference between the different reconstruction methods. A similar trend as the whole brain analysis was observed. Both tensor-derived methods (fDKI_T and NLS_T) provided higher accuracy and less variability than either fDKI or NLS. This is indicated both by smaller errors compared to the gold standard and by smaller standard deviations of errors within each region. NLS has fewer errors than fDKI for both radial kurtosis measures (K_r and K_{rs}). The difference between the two tensor derived methods (fDKI_T and NLS_T) is very small. K_{rs} provides lower errors than K_r for all regions, while MK_s shows no improvement compared to MK.

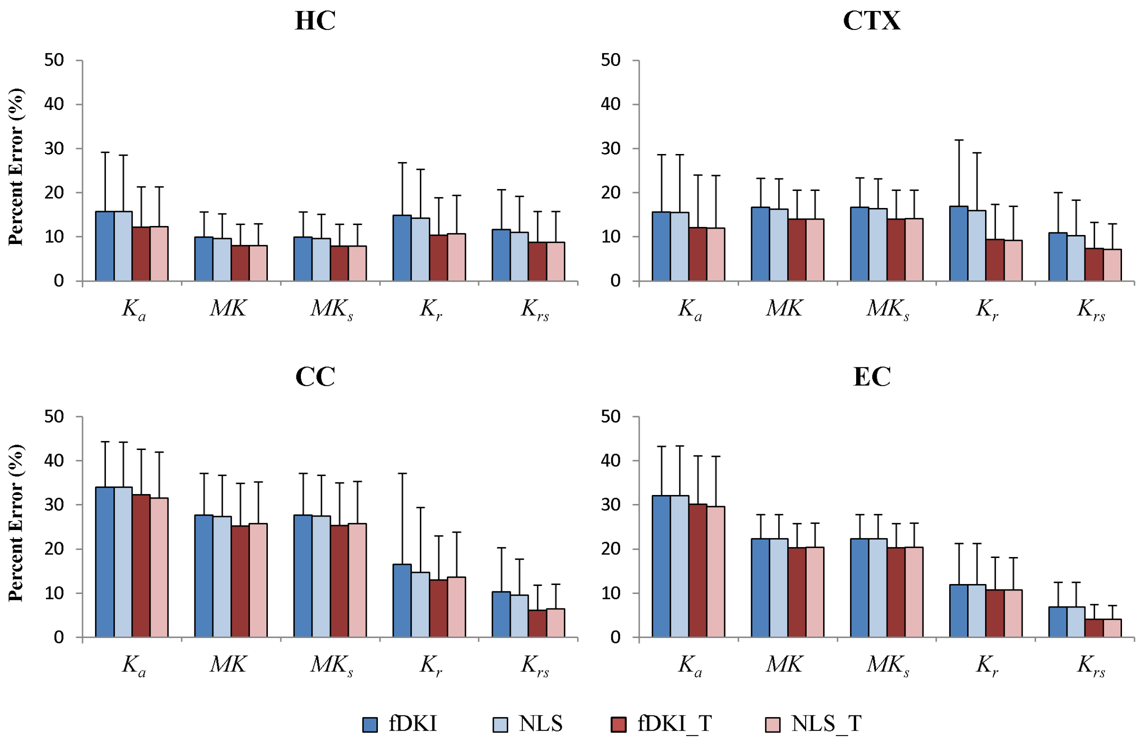

Figure 4.4. Fitting errors in DKI parameters (K_a, MK, MK_s, K_r, K_{rs}) values in cortex (CTX), hippocampus (HC), external capsule (EC) and corpus callosum (CC). Error bars indicate standard deviations of percent errors within each region.

4.4 Discussion

This study describes a tensor-based fast DKI reconstruction method, fDKI_T, which provides better-fitting results than the original DKI reconstruction (NSL) and the fast DKI method (fDKI). This is indicated by less noise in the DKI parametric maps, smaller overall errors across the whole brain, as well as higher accuracy and less variation in regional values. The fDKI_T reconstruction time for a whole brain dataset is only several seconds, comparable to the reconstruction time in DTI, rather than the hour required by the full non-linear fitting. It should be particularly helpful for clinical studies where real-time reconstruction and visualization is highly desirable.

The fDKI_T method is an improvement not only over the original fast DKI method (fDKI) (Jensen et al., 2009), but even over the conventional non-linear least squares method (NLS) (Jensen et al., 2005; Lu et al., 2006) as well. This is due to the fact that conventional DKI fitting estimates 2 parameters (D_{app} and K_{app}) for each diffusion direction, which can result in 60 parameters for the 30 diffusion directions as in this study. These 60 parameters then need to be reduced to 21 tensor-related parameters through a linear least squares fit, which poses an over-fitting problem. In contrast, the proposed fDKI_T method estimates the 21 tensor-related parameters (6 for the diffusion tensor and 15 for the kurtosis tensor) directly from diffusion weighted signals and hence reduces the overall fitting errors.

The proposed fDKI_T method is also flexible for general diffusion weighted imaging schemes (e.g. the number of b-values or applied diffusion gradients directions) and does not require the same set of diffusion directions for different b-values. This provides flexibility for both image acquisition schemes and post-processing methodologies employed.

The results from this study also suggest that if the tensor-based formula is used (Eq. 4.5), then the linear least squares fit (fDKI_T) provides as good results as the much more time consuming non-linear least squares fit (NLS_T). This, again, arises from the improved robustness of the reduced number of fitting parameters. The signal-to-noise ratio (SNR) in the b_0 volume averaged around 35 in the dataset used for this study, which is similar as standard clinical studies (~25-40). If image SNR is much lower (<20), however, NLS_T might show more advantages than fDKI_T because linear fitting requires DW data to be log-transformed first, e.g., $\ln(S(b)/S_0)$, and will give an incorrect weighting for fitting residuals at very low SNR.

Compared to the DTI parameters (FA and MD), DKI parameters (MK, K_a, K_r) are more error prone. This is evident from the increased noisiness in the fitted DKI parametric maps using 2 b-values, compared to the gold standard that uses 5 b-values, while little difference was noted in the DTI parameters. The overall percentage errors also varied strongly across the different fitting methods, indicating that DKI fitting is less robust to changes in the numerical computation method than in the DTI fitting. Among all DKI parameters, radial kurtosis is the most susceptible to noise, followed by axial kurtosis and mean kurtosis. Another important finding is that the surface integration greatly improves the estimation accuracy for radial kurtosis and should always be used. For mean kurtosis, an average over K_{app} from all diffusion directions appeared to work as well as the extended version of surface integration.

All DKI reconstruction methods were compared for a short imaging scheme with only 2 nonzero b-values and 30 diffusion directions. This was suggested by Jensen as the most efficient scheme of DKI acquisition (Jensen et al., 2010). When more b-values are used, the advantage of fDKI_T over NSL or fDKI will likely decrease, due to the increased redundancy of measurements over fitting parameters. Critically, however, acquiring more b-values also means a prolonged imaging acquisition time. This can be hard to accommodate for clinical studies, especially for patients in an acutely injured stage who may be in severe pain or discomfort.

4.5 Conclusion

In this chapter, an improved fast DKI method (fDKI_T) was described. It fits the diffusion and kurtosis tensors directly and improved fitting accuracy over conventional DKI fitting methods. The fDKI_T method provides a DKI reconstruction time of only seconds for a complete brain dataset, which is comparable to the typical DTI reconstruction time. Using the tensor based approach, linear fitting also provides comparable results to the much more time consuming non-linear fitting. This will greatly facilitate DKI applications in clinical practice where real-time reconstruction is highly desirable.

Chapter 5. Diffusion Weighting Schemes and Reconstruction Methods for Diffusion Kurtosis Imaging Parameters

5.1 Introduction

Diffusion Kurtosis Imaging (DKI) characterizes the non-Gaussian nature of water diffusion in tissues (Jensen et al., 2005) and has gained much interest lately. The DKI model extends the linear DTI model by using a cumulant expansion in diffusion weighting (b) with a b^2 term:

$$\ln S(b) = \ln S_0 - bD_{app} + \frac{1}{6} b^2 D^2 K_{app} \tag{5.1}$$

where $S(b)$, S_0 are diffusion weighted and non-diffusion weighted signals, respectively. D_{app} is the apparent diffusion coefficient and K_{app} the apparent diffusion kurtosis. Studies have shown that DKI can capture information regarding the environment of the tissue micrsotructure and extends the utility of diffusion tensor imaging to probe gray matter structures (Cheung et al., 2009; Falangola et al., 2008; Grossman et al., 2011; Helpern et al., 2011; Hui et al., 2008; Wang et al., 2011; Zhuo et al., 2012).

Extending DKI to the clinical, however, poses several challenges. The biggest challenge is the long image acquisition time. The DKI model involves estimation of both the 2nd order diffusion tensor (3×3 symmetric tensor with 6 independent elements, as in standard DTI) and a 4th order kurtosis tensor (3×3×3×3 symmetric tensor with 15 independent elements). So, DKI acquisition requires a minimum of two non-zero b-values measured with at least 15 diffusion directions (Lu et al., 2006). Compared to a

DTI acquisition, which requires only one non-zero b-values measured with at least 6 diffusion directions, DKI acquisition needs approximately 5 times more time. In practice, DKI or DTI acquisitions usually involve several times more data than minimally required in order for more reliable tensor fitting. For example, 30 or more diffusion directions with a b-value of approximately 1000 s/mm^2 are usually recommended for the diffusion tensor estimation in DTI (Jones et al., 1999). A typical DKI imagine scheme with 30 diffusion directions and 5 non-zero b-values (b = 500, 1000, 1500, 2000, 2500 s/mm^2, referred to as the 5B30D scheme) takes nearly 20 min to cover the whole brain (Jensen et al., 2005). Such long acquisitions not only lead to poor data quality because of motion but can be intolerable for patients who may be under severe discomfort. To circumvent the long acquisition time, usually only part of the brain is covered in DKI studies in order to achieve a more clinically feasible scan time of ~10 min (Falangola et al., 2008; Helpern et al., 2011; Wang et al., 2011). More recently, Jensen et al. has suggested a shorter DKI imaging scheme with 30 diffusion directions and only 2 non-zero b-values (b = 1000, 2000 s/mm^2, referred to as the 2B30D scheme) (Jensen and Helpern, 2010) for more efficient DKI acquisition. The 2B30D scheme requires only 7 min to cover the whole brain. But, little is known about the whether it might be an optimal scheme, and what is the accuracy and variability in estimated DKI parameters using this imaging scheme, compared to the 5B30D scheme.

This leads to a question: what is the optimal DKI imaging scheme, within a limited acquisition time? Ideally, model fitting always improves with more measurements. More measurements here can be either more diffusion weightings (more b-values) or more diffusion directions. There has been substantial theoretical and experimental effort in developing optimized DTI imaging schemes to improve the accuracy and variability in estimating the diffusion tensor (Alexander and Barker, 2005; Conturo et al., 1996; Hasan et al., 2001, Jones et al., 1999; Jones, 2004; Landman et al., 2007). But, little research has been done on the choices of possible b-values and diffusion directions for DKI and their effect on the estimation of the kurtosis tensor. Previously Poot et al., (2009) proposed an optimization framework for DKI based on minimizing the Cramer-Rao lower bound of a DKI parameter (mean kurtosis, MK or radial kurtosis, K_r) (Poot et al., 2009). Although Poot's approach provides a theoretical foundation for optimizing DKI imaging schemes, it depends on the estimation of a prior distribution of DKI parameters. The distribution can vary depending on the diffusion weighted MR imaging parameters (echo time, repetition time, image resolution, etc.) and the subject being scanned. So, Poot provides no uniform solution. What constitutes an optimal and efficient DKI acquisition still remains unknown.

A second challenge for DKI is the low signal-to-noise ratio (SNR) in diffusion-weighted images. Diffusion weighted MRI typically uses the echo planar imaging (EPI) technique, which is rapid but inherently low SNR. On top of that, the diffusion weighting also causes signal attenuation that scales with the b-value (Basser et al., 1994). In DKI, b-values up to 2000 or 2500 s/mm^2 are typically used, much more than in a standard DTI acquisition (b = 1000 s/mm^2), in order to reveal the heterogeneous diffusion distances related to the heterogeneous cellular structures (Jensen et al., 2005). Therefore, image noise is a greater concern in DKI. The effect of noise on DTI parameters has been investigated extensively (Anderson et al., 2001; Jones et al., 2004; Farrel et al., 2007; Landman et al., 2008), but how noise affects the accuracy and variability of the estimated

DKI parameters is not well known. Such an understanding would be very helpful in interpreting DKI results.

Another factor that affects the estimation of DKI parameters is the choice of reconstruction method, because estimation of the kurtosis tensor can be highly susceptible to fitting errors (Tabesh et al., 2010; Veraart et al., 2011). Since diffusion of water molecules reflects the physical property of tissues, diffusion parameter estimates must be physically meaningful. But, noise in the measured diffusion weighted signal can make the estimated diffusion and kurtosis parameters deviate from their true underlying values, causing erroneous inferences. For example, the diffusion coefficient (D_{app}) should always be non-negative, i.e., the diffusion weighted signal $S(b)$ should have attenuated signal compared to non-diffusion weighted signal S_0 (Basser et al., 1994). This is the guiding principle of diffusion weighted MRI, but it can be violated in isolated voxels when diffusion is extremely restricted and very little signal attenuation is truly present. Kurtosis values can also be easily fitted too low or too high. The lower physical bound for kurtosis values should be zero, according to both multi-compartment diffusion models and empirical evidence from the brain (Jensen and Helpern, 2010): $S(b)$ should be a convex function of b. But when the signal attenuation is small and $S(b)$ stays almost constant for all b, noise can easily make $S(b)$ appear as a concave function of b. This then may result in very large negative kurtosis values. The upper bound for kurtosis values is believed to be $3/(b_{max} \cdot D_{app})$, where b_{max} is the maximum b-value used for acquisition (Jensen and Helpern, 2010). This constraint is to ensure that $S(b)$ stays within the monotonically decaying portion with respect to b (the left half of the quadratic DKI Eq. 5.1), because stronger diffusion weighting (higher b-value) should always result in higher signal attenuation (Basser et al., 1994). For the same reason, b_{max} in DKI acquisition is always restricted to no more than 2500-3000 s/mm^2. Yet, even with a b_{max} of only 2000 s/mm^2, such violations can still arise in case of high diffusion coefficient (e.g., in cerebral spinal fluid or along the axial direction of the axons).

Negative diffusion coefficients are rather rare (< 1% of brain voxels) and are associated with extremely low SNR (Landman et al., 2008). Hence, although nonnegative diffusion tensor reconstruction methods have been developed (Cox and Glen, 2006; Koay et al., 2006), the unconstrained linear least squares fitting still remains the most common choice for DTI reconstruction due to its fast and easy implementation. On the contrary, physically irrelevant kurtosis values are frequently observed in more than 10% of brain voxels (Tabesh et al., 2011; Veraart et al., 2011) and may cause erroneous results if left untreated. Therefore, constrained fitting, which ensures all diffusion and kurtosis values are physically meaningful, has been suggested for DKI reconstruction (Jensen and Helpern, 2010; Tabesh et al., 2010; Veraart et al., 2011). But, caution must be taken with constrained fitting because it may itself introduce new errors. For example, the maximum kurtosis value is based on the estimation of D_{app}. An underestimated D_{app} can lead to overestimated K_{app}. Therefore, it is important to understand the effect of constrained fitting in estimating DKI parameters.

In this study, the way in which diffusion weighted imaging schemes affect the accuracy and variability of DKI derived parameters are analyzed using data obtained from a human volunteer. Based on the results, we proposed two optimal DKI imaging schemes within a clinically feasible acquisition time (<10 min). The performance of these optimal schemes are compared to the more frequently used DKI imaging schemes

(5B30D and 2B30D) by evaluating their estimation accuracy of DKI parameters and their susceptibility to physically irrelevant diffusion and kurtosis values. Finally, the effect of constrained versus unconstrained DKI reconstruction methods and image SNR are analyzed for different imaging schemes using both human data and Monte Carlo simulation.

5.2 Preprocessing Methods

5.2.1 Data Acquisition

A complete DKI dataset was obtained on a healthy 33 year old male volunteer on a Siemens Tim Trio 3T clinical scanner with body coil excitation and 12-channel phased array coil for reception. Following a 3D T_1-MPRAGE acquisition for anatomical reference, four separate datasets of DKI acquisitions were obtained. Each DKI dataset contained 5 non-zero b-values (b = 500, 1000, 1500, 2000, 2500 s/mm^2), each applied in 64 diffusion directions plus eight additional volumes with no diffusion weighting (b = 0 s/mm^2). Diffusion weighted gradient was applied using a twice-refocused single-short spin-echo echo planar imaging sequence for reduced eddy current distortion [Reese et al., 2003]. Each DKI dataset contained 40 axial slices and were collected with an isotropic resolution of 2.7mm. Parallel imaging using the GRAPPA technique was used with an acceleration factor of 2 at a TE/TR = 101ms/5500ms. Due to the lengthy acquisition time of a complete 64 direction using five b-values, each repeat of the DKI acquisition was split into two sessions with 32 directions each and the transmit frequency was readjusted after each single set to account for the B_0 frequency shift. The total scan time for one repeat of DKI dataset was 25 minutes (12.5 minutes for each 32 direction set). The 3D

T_1-MPRAGE sequence was acquired in the sagittal plane with an isotropic resolution of 1mm, at an FOV of 25.6cm, using TI/TE/TR/flip of 900ms/3.39ms/2500ms/9°.

5.2.2 Data Preprocessing

Each of the two 32 direction DKI acquisitions were first concatenated which resulted in four complete DKI datasets with 64 directions and five diffusion weightings. Each volume of each dataset was then registered to the b=0 volume using 12 degree-of-freedom affine registration to correct for motion SPM8 (Statistical Parametric Mapping, Wellcome Department of Imaging Neuroscience, University College London, UK). The four motion-corrected DKI datasets were then averaged to construct an averaged DKI dataset to serve as the gold standard. Both the individual DKI datasets and the averaged DKI datasets were then smoothed with a 3D Gaussian filter with FWHM = 3.0mm to increase the SNR. The appropriate datasets were used to construct subsets as described in section 5.2.5.

5.2.3 DKI Reconstruction

The diffusion tensor **D** and kurtosis tensor **W** were estimated for without any constraints using the linear least squares (LS) fit using the following equation (Zhuo et al, 2011):

$$\ln S(\mathbf{g},b) = \ln S_0 - b\sum_{i=1}^{3}\sum_{j=1}^{3} g_i g_j D_{ij} + \frac{1}{6}b^2 \sum_{i=1}^{3}\sum_{j=1}^{3}\sum_{k=1}^{3}\sum_{l=1}^{3} g_i g_j g_k g_l K_{ijkl} \qquad (5.2)$$

where $S(\mathbf{g},b)$ is the diffusion weighted signal at diffusion direction $\mathbf{g} = (g_1,g_2,g_3)$ at a particular b-value. S_0 is the non-diffusion weighted signal, D_{ij} is an element of the diffusion tensor **D** and K_{ijkl} is related to element W_{ijkl} of the kurtosis tensor **W** by $K_{ijkl} = MD^2 \cdot W_{ijkl}$.

Since both **D** and **W** are totally symmetric matrices, with 6 independent elements of the diffusion tensor and 15 independent elements for the kurtosis tensor respectively, a total of 21 parameters were fitted using Eq. 5.2. The apparent diffusion coefficient $D_{app}(\mathbf{g})$ and apparent kurtosis $K_{app}(\mathbf{g})$ for each direction **g** were then calculated from:

$$D_{app}(\mathbf{g}) = \sum_{i=1}^{3}\sum_{j=1}^{3} g_i g_j D_{ij} \tag{5.3}$$

$$K_{app}(\mathbf{g}) = \frac{1}{D_{app}(\mathbf{g})^2} \sum_{i=1}^{3}\sum_{j=1}^{3}\sum_{k=1}^{3}\sum_{l=1}^{3} g_i g_j g_k g_l K_{ijkl} \tag{5.4}$$

Three types of constraints based on physical constraints of the biological system were considered as suggested by Tabesh et al. (2010):

Constraint 1: Non-negative diffusion coefficient, which requires that:

$$D_{app}(\mathbf{g}) \geq 0 \text{ , for any } \mathbf{g} \tag{5.5}$$

Constraint 2: Non-negative kurtosis, which requires that:

$$K_{app}(\mathbf{g}) \geq 0 \text{ , for any } \mathbf{g} \tag{5.6}$$

Constraint 3: The diffusion weighted signal $S(\mathbf{g},b)$ should be a monotonically decreasing function of b, which requires that:

$$K_{app}(\mathbf{g}) \leq K_{\max}(\mathbf{g}) = \frac{3}{D_{app}(\mathbf{g}) \cdot b_{\max}} \text{ , for any } \mathbf{g} \tag{5.7}$$

where b_{max} is the maximum b-value used in the imaging protocol.

The constrained linear least squares fitting (CLS) was implemented using the lsqlin() function in Matlab (Version R2007a, MathWorks) based on quadratic programming (Tabesh et al., 2010).

DTI parameters, such as mean diffusivity (*MD*), fractional anisotropy (*FA*), axial (λ_a) and radial diffusivity (λ_r) were calculated by eigen-decomposition of the diffusion tensor (Eqs. 2.9-11). DKI parameters, such as mean kurtosis (*MK*), axial kurtosis (K_a) and radial kurtosis (K_r) were calculated from the kurtosis tensor using elliptic integrals derived by Tabesh et al., (2010).

5.2.4 Image Analysis

Performance of DKI estimation was based on the accuracy and variability in estimating diffusion tensor and kurtosis tensor parameters. Parameter values were measured from several representative regions of interest (ROI) and from the whole brain.

In ROI analysis, four representative ROIs, two each from white and gray matter were chosen (Figure 5.1). The white matter (WM) ROI's included the genu of the corpus callosum and the internal capsule. The gray matter (GM) ROI's included the thalamus and the basal ganglia. ROIs were drawn on the *FA* map reconstructed from the gold standard data (average of the 4 complete DKI datasets), with the 3D MPRAGE images serving as the high resolution anatomical reference. Voxel values from preprocessed diffusion weighted images were averaged first from each region before tensor fitting. These were compared with the respective parameter values from the ROI's of the parametric maps of the gold standard dataset. It should be noted that the gold standard data did not exhibit any violations of the above mentioned constraints (section 5.2.2) and hence the LS-fitted and the CLS-fitted data produced the same results.

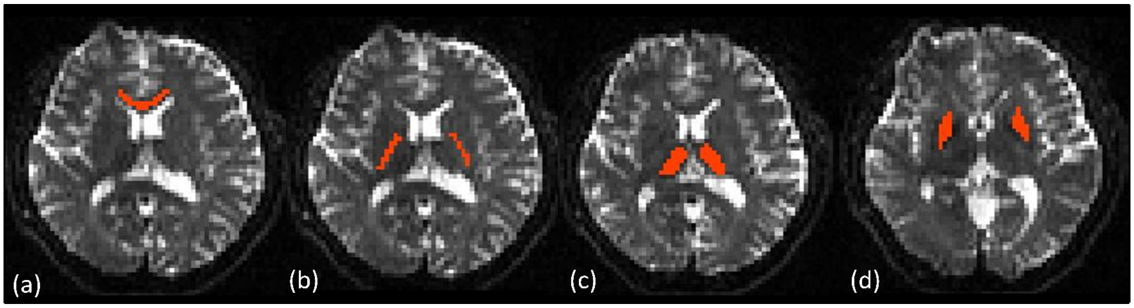

Figure 5.1. Illustration of different ROIs used in imaging analysis: genu of the Corpus Callosum (a) and internal capsule (b) in white matter; and the thalamus (c) and basal ganglia (d) in grey matter. The ROIs were shown on a b_0 image.

In order to understand the overall accuracy and variability of DKI parameters in different brain tissues that have distinct diffusion properties, values from whole brain white matter (WM), grey matter (GM) and cerebrospinal fluid (CSF) were also analyzed. Since the MPRAGE images were acquired at a higher resolution than the DW images, the MPRAGE images were resampled to the resolution as the DW images. A segmentation of the whole brain to different brain tissues (WM, GM and CSF) was then performed using the 3D MPRAGE images after registering the MPRAGE images to the FA images using SPM8. Figure 5.2 showed two representative slices from the original MPRAGE images and the segmented tissue masks for each of the brain tissue types (WM: pink, GM: green, CSF: blue). The segmented tissue probability maps were thresholded with a $p > 0.6$ to generate binary masks for each segment. The segmented GM and WM *MK* maps are also shown in Figure 5.2.

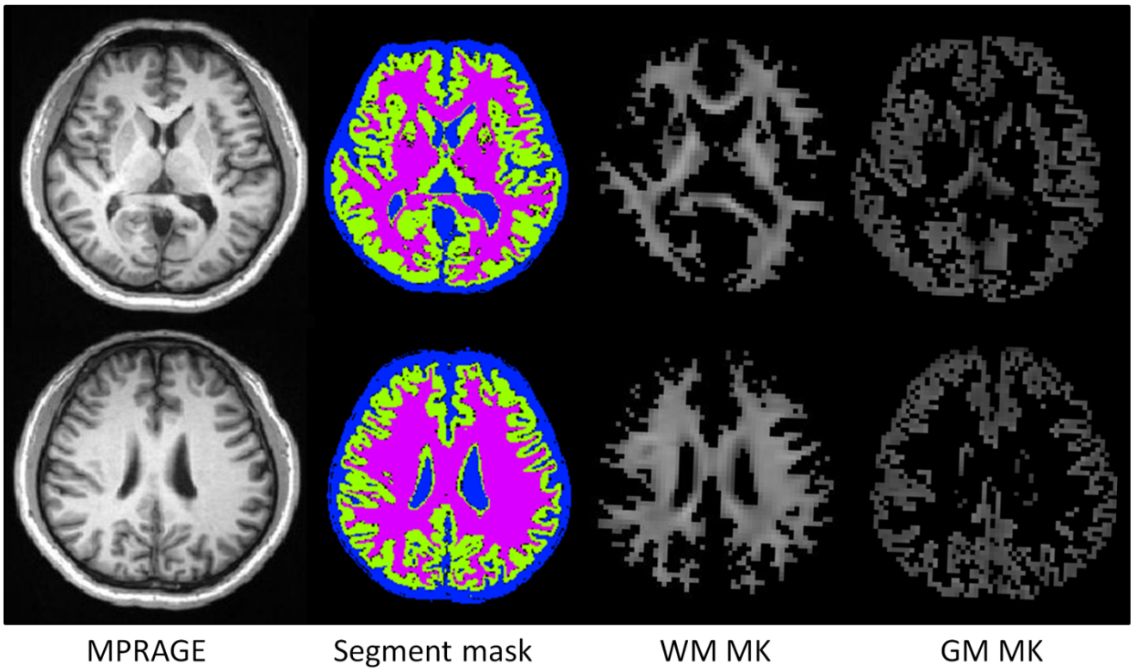

Figure 5.2. Segmentation results based on the MPRAGE acquisition. Images shown from left to right are: representative slices of the MPRAGE volume; the segment mask (WM in pink, GM in green, CSF in blue); masked out WM *MK* map; masked out GM *MK* map.

5.2.5 Partitioning and Selection of Diffusion Gradient Subsets

The effect of diffusion weighted imaging schemes was studied by partitioning and grouping of diffusion weighted data from the complete DKI datasets to construct various imaging schemes. More specifically, the effect of the number of diffusion direction chosen was studied by taking subsets with 15 (Ndir_{15}), 30 (Ndir_{30}) and 45 (Ndir_{45}) diffusion directions from the complete dataset of 64 directions (Ndir_{64}). Effect of the applied diffusion weightings was studied by taking various combinations of two (Nbval_{2}), three (Nbval_{3}) and four (Nbval_{4}) nonzero b-value subset from the complete set of 5 b-values (Nbval_{5}) used for the gold standard dataset. These repartitioned and grouped data were then used to recreate the diffusion and kurtosis tensors respectively for each of the imaging schemes.

1) Selection of Diffusion Direction Subsets

To study the effect of applied number of diffusion directions, subsets with 15 ($Ndir_{15}$), 30 ($Ndir_{30}$) and 45($Ndir_{45}$) diffusion directions were taken from the complete dataset of 64 directions. The Monte Carlo pair-wise (MCPW) relaxation method was used (Landman et al., 2006) to derive these data with subsets of direction vectors that are as uniformly distributed as possible on a unit sphere, and yet had minimal electrostatic energy (Jones et al., 1999), In the MCPW procedure, an initial direction vector subset with desired number of directions is first selected randomly. An exhaustive pair-wise swapping of each direction vector within the direction subset and each gradient vector outside of the direction subset is then carried out in order to minimize the electrostatic energy of the selected direction subset. Although each MCPW procedure results in a different optimal direction subset, depending on the starting subset, they are all near optimal. Figure 5.3 shows the achieved electrostatic energy for 100 MCPW procedures for an optimal $Ndir_{30}$ subset from $Ndir_{64}$. The electrostatic energy for all optimal $Ndir_{30}$ subsets (blue circles) are significantly lower compared to a randomly picked 30-direction subset (red line), and are all within 1% of the MR vendor provided 30-direction set, which is considered truly optimal (green line).

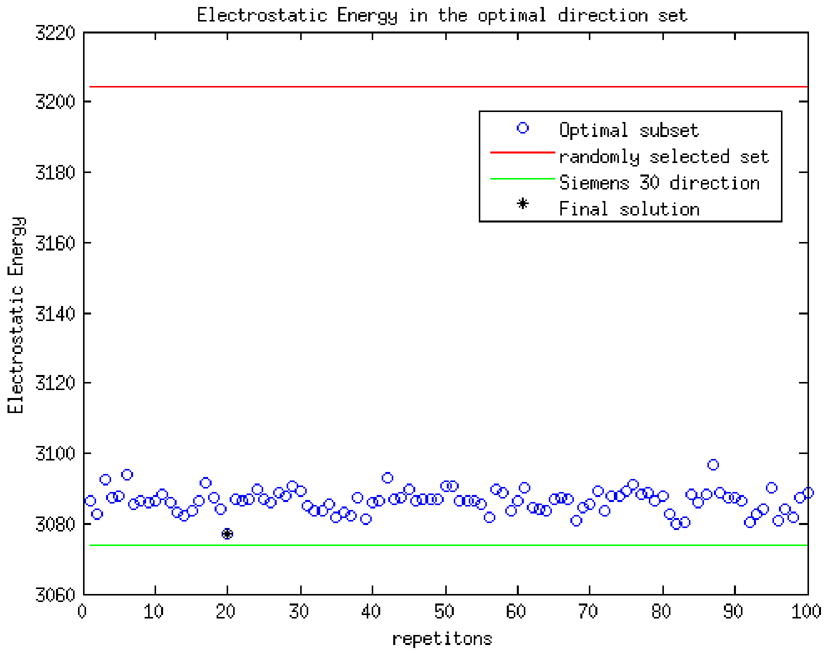

Figure 5.3. Electrostatic energy of 100 optimal 30-diffusion-direction subsets ($Ndir_{30}$) from the MCPW procedures (blue circles). All optimal $Ndir_{30}$ subsets achieved electrostatic energy that is much lower than a random pick (red line) and is close to the MR vendor provided 30-direction set (green line).

In order to find diffusion gradient subsets that are close to the true optimal, 100 MCPW procedures were run for each number of diffusion directions ($Ndir_{15}$, $Ndir_{30}$, $Ndir_{45}$) and the one with the lowest electrostatic energy was selected (denoted as black star for the $Ndir_{30}$ subset in Figure 5.3). Figure 5.4 shows the final optimal $Ndir_{15}$, $Ndir_{30}$ and $Ndir_{45}$ subsets from the complete $Ndir_{64}$ set. These subsets were used for whole-brain analysis of DKI parameters.

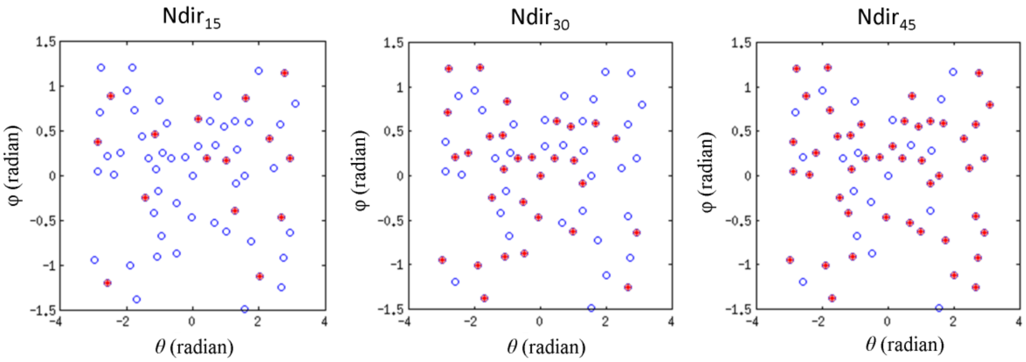

Figure 5.4. The optimal 15, 30, 45 diffusion direction subsets from 100 MCPW procedures. Each of the direction subsets is plotted (red stars) alongside the complete Ndir_{64} set (blue circles) using spherical coordinate grid.

Landman et al. has suggested that diffusion direction sets may have angular dependent variability in estimating diffusion tensors (Landman et al., 2007). Therefore, the optimal diffusion direction subsets are reasonable for whole-brain analysis where the variability in tensor directions differs in different anatomies. However, at the ROI level within a given anatomical region, this may cause unwanted bias. In order to account for this angular dependent variability that is associated with the choice of the diffusion direction vectors, eight maximally different direction subsets were picked from the Ndir_{64} set for each of 15, 30 and 45 diffusion direction schemes. Since, at most, four independent direction subsets can be found with the smallest Ndir (Ndir_{15}), eight maximally different gradient sets were considered to be a fair number to account for the variability associated with the derived tensor parameters. To choose maximally different gradient subset, 1000 MCPW procedures were performed and a gradient subset was kept only if it had at least K different directions than all previously chosen sets. In our experiment, the selected subsets were at least 25% different from each other for Ndir_{45} ($K = 12$), at least 50% from each other for Ndir_{30} ($K = 15$) and at least 70% different from each other for Ndir$_{15}$ (K = 11). Figure 5.5 shows an example selection of eight Ndir$_{30}$ subsets (red stars) plotted against the original Ndir$_{64}$ set (blue circle) using spherical coordinates. The electrostatic energy of selected Ndir$_{30}$ subsets are at most 0.6% higher than that provided by the vendors provided optimal 30 direction set. The eight subsets for each Ndir set were then picked from each of the 4 DKI datasets, resulting in a total of 32 data points (4 repetitions × 8 direction sets) for each imaging scheme with 15, 30 and 45 diffusion directions.

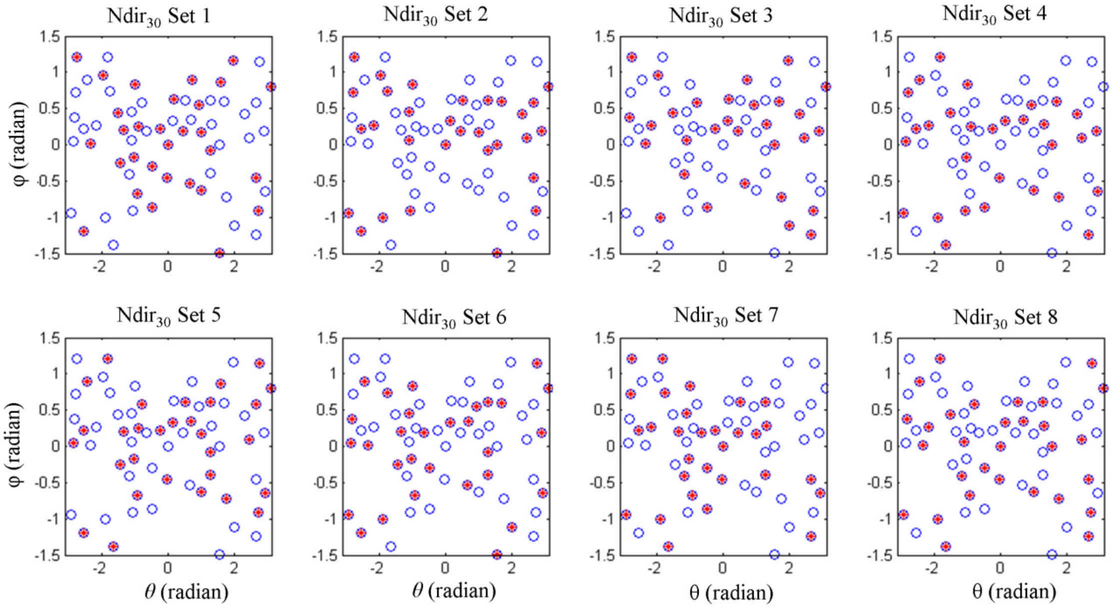

Figure 5.5. The graphs demonstrate an example of eight Ndir$_{30}$ subsets (red stars) deduced from the complete 64 diffusion directions (blur circles) using a spherical coordinate grid.

2) Selection of Diffusion Weighting Subsets

All possible choices of Nbval$_2$, Nbval$_3$ and Nbval$_4$ were considered from the complete Nbval$_5$ set by keeping b=1000 s/mm^2 (standard clinical choice in DTI) as a standard fixture in each of the choices. Choosing a b=1000 s/mm^2 as a standard fixture in each scheme allows the flexibility for choosing either DTI or DKI reconstruction algorithms. It should be noted that the diffusion tensor parameters estimated using the DKI model have a positive bias compared to those estimated using the DTI model (Veraart et al., 2011), and, therefore, this flexibility may be desirable as it provides the ability to compare the diffusion tensor values with existing literature that is widely available based on DTI reconstruction.

Therefore, the choices of b-values studied here were:

$\underline{\text{Nbval}_2}$: $b = 1000, 2000$ s/mm^2; $b = 1000, 2500$ s/mm^2.

$\underline{\text{Nbval}_3}$: $b = 500, 1000, 2000$ s/mm^2; $b = 500, 1000, 2500$ s/mm^2; $b = 1000, 1500, 2000$ s/mm^2; $b = 1000, 1500, 2500$ s/mm^2; $b = 1000, 2000, 2500$ s/mm^2.

$\underline{\text{Nbval}_4\text{:}}$ $b = 500, 1000, 1500, 2000$ s/mm^2; $b = 500, 1000, 1500, 2500$ s/mm^2; $b = 1000, 1500, 2000, 2500$ s/mm^2; $b = 500, 1000, 2000, 2500$ s/mm^2.

$\underline{\text{Nbval}_5\text{:}}$ $b = 500, 1000, 1500, 2000, 2500$ s/mm^2.

Note that the number of b-values specifically refers to the nonzero b-values and does not include the $b = 0$ dataset (same for all later references).

5.3 Experimental Methods and Results

Five sequential experiments are described in this section. The first experiment involves the evaluation of the effect of the choice of the specific b-values on the final diffusion and kurtosis parameters. The goal here is to understand the effect of specific b-values chosen and their influence in estimation accuracy. This experiment will provide information on optimal b-values to choose for diffusion or kurtosis tensor estimation.

The second experiment checks the effect of number of b-values and number of diffusion directions on the estimated diffusion and kurtosis parameters. The goal of this experiment is to understand the benefits of the increased number of b-values versus the number of diffusion directions applied. These experiments will lead to the identification of efficient imaging schemes, specifically those that can be obtained in a clinically feasible time (10 min of acquisition time).

The third experiment will be to assess the performance of different imaging schemes derived from the second experiment, compared to the ideal imaging scheme of 5 b-values and 30 diffusion directions (Jensen et al., 2005; Helpern et al., 2011; Hui et al., 2008; Cheung et al., 2009) (hereafter referred to as the 5B30D scheme) and a previously suggested shorter imaging scheme of 2 b-values and 30 diffusion directions (Jensen and Helpern, 2010; Tabesh et al., 2011) (hereafter referred to as the 2B30D scheme).

The fourth experiment involves the evaluation of the non-constrained least square and the constrained least square fitting technique to assess their ability to provide accurate diffusion and kurtosis tensor estimates. Three specific constraints as described in section 5.2.3, to ensure the derived diffusion and kurtosis parameters to be physically meaningful, will be considered.

The fifth experiment involves the evaluation of the effect of noise to the accuracy and variability in estimating diffusion and kurtosis parameters using different imaging schemes.

5.3.1 Experiment#1: Effect of the Choice of b-values on the Derived DKI Parameters

Methods: The effect of the choice of b-values on the quality of DKI estimation was assessed in this experiment by comparing the accuracy and variability in regional parameteric values, compared to the gold standard. The comparison was performed using 30 diffusion directions as it is the most frequent choice for a DKI acquisition. It is also more clinically practical than 45 or 64 directions where the acquisition time is well above 10 min since more than 2 b-values are used.

Regional diffusion weighted signals were extracted from the four complete DKI datasets. Different b-value subsets and the eight $Ndir_{30}$ subsets were then selected from each of the four complete DKI datasets to recreate the diffusion and kurtosis tensors using CLS, resulting in 32 data points for each parameter for each b-value set. The mean ($\bar{S}$) and standard deviation ($\sigma(S)$) from these 32 data points for each parameter were then calculated. Estimation accuracy is based on percent bias for each parameter calculated. Since the bias can be positive or negative for different imaging schemes, only the absolute values of bias are considered here:

$$Bias_{roi} = \frac{\left|\bar{S} - S^{gold}\right|}{S^{gold}} \cdot 100\% \tag{5.8}$$

where S^{gold} stands for the gold standard parameter value. Estimation variability is based on the percent coefficient of variation (CV) for each parameter:

$$CV_{roi} = \frac{\sigma(S)}{\bar{S}} \cdot 100\% \tag{5.9}$$

This experiment should lead to the best combination of b-values that would provide the diffusion and kurtosis tensor estimates with the highest accuracy and the least variability from each of the $Nbval_2$, $Nbval_3$ and $Nbval_4$.

Results: Figure 5.6 shows the mean and standard deviation of K_a, K_r, MK and λ_a, λ_r, MD for each Nbval set compared to the gold standard value for genu and thalamus, as representative of WM and GM regions. The Nbval sets with a b_{max} of 2000 s/mm^2 ($Nbval_2$: b = 1000, 2000 s/mm^2; $Nbval_3$: b = 500, 1000, 2000 s/mm^2 and b = 1000, 1500, 2000 s/mm^2; $Nbval_4$: b = 500, 1000, 1500, 2000 s/mm^2) demonstrated a strong positive bias in estimating all parameters. The bias is worse for the kurtosis parameters (K_a, K_r, MK) compared to the diffusion parameters (λ_a, λ_r, MD). The variability in all the estimated parameters as demonstrated by the standard deviations in the graphs was also higher in the sets with a b_{max} of 2000 s/mm^2. For the $Nbval_2$ set, b = 1000, 2500 s/mm^2 shows clear advantage in terms of both bias and variability in both regions. For the $Nbval_3$ and $Nbval_4$ subsets, the differences between the various choices of b-values with a b_{max} of 2500 s/mm^2 are small.

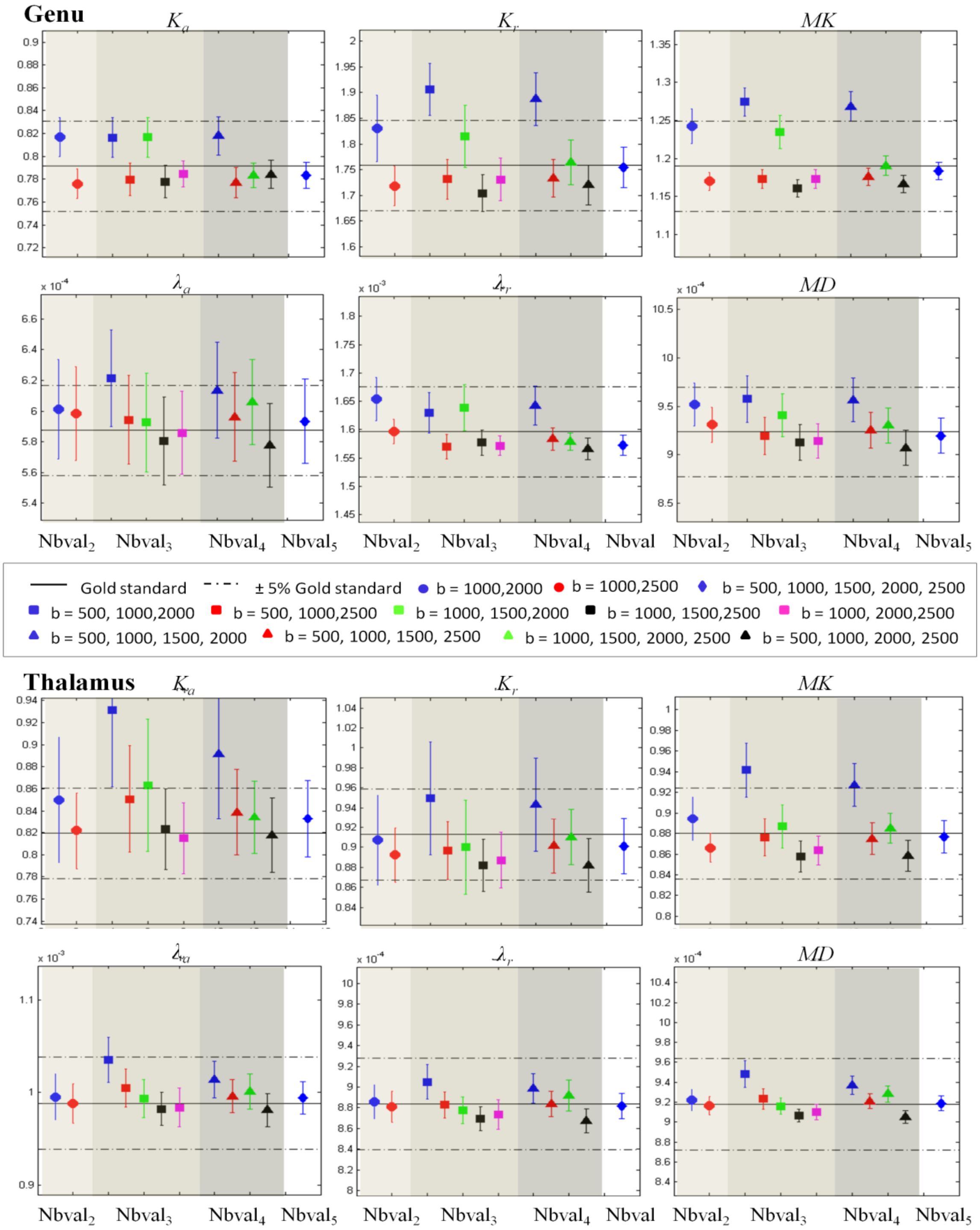

Figure 5.6. Mean and standard deviation (error bars) of K_a, K_r, MK and λ_a, λ_r, MD for each Nbval set compared to the gold standard value for genu and thalamus. The solid line shows the gold standard value and the dotted line shows ±5% of the gold standard value.

Table 5.1 displays the overall percent bias and coefficient of variation (CV) averaged across diffusion and kurtosis parameters (λ_a, λ_r, MD and K_a, K_r, MK) for the various Nbval sets in all WM (genu and internal capsule) and GM (thalamus and basal ganglia) regions. The differences between the two $Nbval_3$ sets: b = 500, 1000, 2500 s/mm^2 vs. b = 1000, 2000, 2500 s/mm^2 or the two $Nbval_4$ sets: b = 500, 1000, 1500, 2500 s/mm^2 vs. b = 1000, 1500, 2000, 2500 s/mm^2 is small. The bias and CV also vary across regions. The final choices (indicated in Table 5.1 in bold) were based on the low CV and bias averaged from all regions.

b-values	genu		thalamus		internal capsule		basal ganglia		Average	
	Bias	CV	Bias	CV	Bias	CV	Bias	CV	Bias	CV
1000, 2000	3.47	2.91	1.22	3.24	2.90	2.86	3.85	4.13	2.53	3.29
1000, 2500	**1.42**	**2.24**	**0.78**	**2.28**	**0.72**	**1.77**	**1.58**	**2.75**	**1.53**	**2.26**
500, 1000, 2000	5.04	2.66	5.84	3.64	4.95	2.49	5.98	4.76	4.51	3.39
500, 1000, 2500	1.27	2.23	1.39	2.60	0.64	1.74	0.96	3.52	1.35	2.52
1000, 1500, 2000	2.60	2.92	1.47	3.16	1.90	2.79	3.65	3.96	2.23	3.21
1000, 1500, 2500	1.80	2.20	1.65	2.17	1.53	1.63	1.84	2.88	1.79	2.22
1000, 2000, 2500	**1.10**	**2.09**	**1.29**	**2.22**	**0.93**	**1.61**	**2.11**	**2.53**	**1.35**	**2.11**
500, 1000, 2500, 2000	4.70	2.63	3.96	3.05	4.31	2.42	5.01	3.78	3.79	2.97
500, 1000, 1500, 2500	1.15	2.15	0.88	2.23	0.61	1.63	0.77	2.75	1.20	2.19
1000, 1500, 2000, 2500	**1.06**	**2.06**	**0.99**	**2.19**	**0.91**	**1.56**	**1.37**	**2.59**	**0.74**	**2.10**
500, 1000, 2000, 2500	1.72	2.11	1.69	2.13	1.71	1.54	2.01	2.98	1.28	2.19
500, 1000, 1500, 2000, 2500	**0.78**	**2.06**	**0.69**	**2.16**	**0.27**	**1.54**	**0.80**	**2.77**	**0.43**	**2.13**

Table 5.1. Percent bias and coefficient of variation (CV) averaged across the diffusion and kurtosis parameters (K_a, K_r, MK, λ_a, λ_r, MD) for all ROIs. An overall average for the bias and CV are listed in the last column. Rows in bold indicate the final choice of b-values for Nbval$_2$ (b = 1000, 2500 s/mm^2), Nbval$_3$ (b = 1000, 2000, 2500 s/mm^2) and Nbval$_4$ (b = 1000, 1500, 2000, 2500 s/mm^2). Bias and CV shown are all in %.

5.3.2 Experiment#2: Effect of the Number of b-values Chosen & Diffusion Directions Chosen on the Variability of DKI estimation

Methods: The accuracy and variability of diffusion and kurtosis parameter estimates from the choice of the number of b-values and diffusion gradient direction subsets were studied in this experiment. The goal of this experiment was to understand whether the increased number of b-values or an increased number of diffusion directions is beneficial for accurate DKI estimation. Only the optimal Nbval sets from Exp#1 were considered along with the eight subsets from each of the Ndir subsets ($Ndir_{15}$, $Ndir_{30}$ and $Ndir_{45}$) and the one complete $Ndir_{64}$ set for every DKI dataset. Assessment was again based on estimation bias (Eq 5.8) and variability (Eq 5.9) from each of the Nbval / Ndir combinations. The output of this experiment is to arrive at efficient imaging schemes that are practical in the clinical setting (acquisition time of ~10 min).

Results: Figure 5.7 shows mean and standard deviation of K_a, K_r, MK and λ_a, λ_r, MD with various numbers of b-values (Nbval2, Nbval3, Nbval4, Nbval5) and diffusion directions ($Ndir_{15}$, $Ndir_{30}$, $Ndir_{45}$ and $Ndir_{64}$) in genu and thalamus. The inherent variability for each parameter was determined from the four repetitions of the complete DKI acquisition, whose CV was found to be approximately 2% (ranging from 0.5% -5% across parameters and regions). Given this variability, the number of b-values chosen appeared to make little difference to the estimate of both the diffusion and kurtosis parameters. However, there is a significant reduction in the variability and accuracy of the estimates when going from 15 ($Ndir_{15}$) to 30 diffusion directions ($Ndir_{30}$), especially for the kurtosis parameters (K_a, K_r, MK). A further reduction in the variability with increasing diffusion directions from 30 to 45 ($Ndir_{45}$) was also observed for K_r in the genu and K_a and K_r for the thalamus.

To determine the optimal imaging schemes, the bias and CV for diffusion and kurtosis parameters (K_a, K_r, MK and λ_a, λ_r, MD) were averaged. The average bias for any parameters did not appear to be related to the choice of the imaging scheme (typically 1-2%, compared to the inherent variability of approximately 2% for the gold standard). Therefore, only the averaged CV from all regions was considered in determining the efficient imaging schemes (Figure 5.8). For each region, the average CV was plotted against the number of diffusion weightings used to obtain the data (NDir × Nbval) as shown in Figure 5.8. The average CVs for $NDir_{15}$ were much higher than any other NDir set for all regions. As expected, reduced CVs were observed with increased diffusion directions. However, for each NDir set, increased numbers of b-values appear to have very little effect on reducing CVs. With an acquisition time of approximately 6 sec (repeat time) for each diffusion weighted volume, and a recommended choice of at least 1 b_0 volume for every 7 diffusion weighted volumes (Jones et al., 1999), 90 diffusion weighted volumes would require an acquisition time of approximately 10 min (dotted line in Figure 5.8). Keeping this time constraint in mind, optimal imaging scheme is the combination of $NDir_{30}$ and $Nbval_2$ with approximately 7 min of acquisition time (referred to as the Opt7min scheme, circled in red in Figure 5.8). However, an extended imaging scheme may be used which is a combination of $NDir_{45}$ and $Nbval_2$, which requires an acquisition time of approximately10 min (referred to as the Opt10min scheme, circled in black in Figure 5.8).

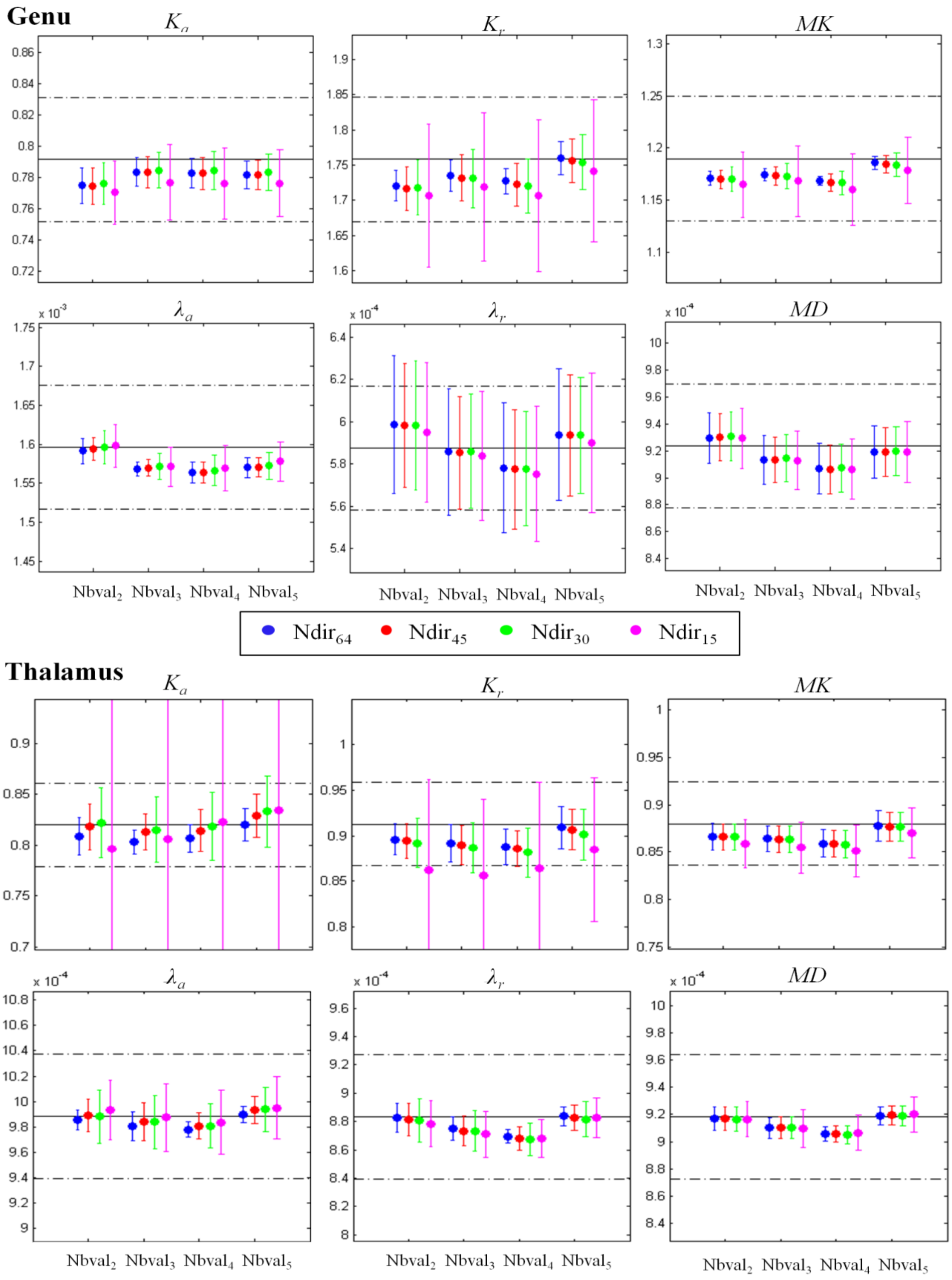

Figure 5.7. Mean and standard deviation (error bars) of K_a, K_r, MK and λ_a, λ_r, MD in the genu and thalamus for various b-valuses (Nbval$_2$, Nbval$_3$, Nbval$_4$, Nbval$_5$) and diffusion directions (Ndir$_{64}$, Ndir$_{45}$, Ndir$_{30}$, Ndir$_{15}$). The solid line is the gold standard value and the dotted line shows ±5% of the gold standard value.

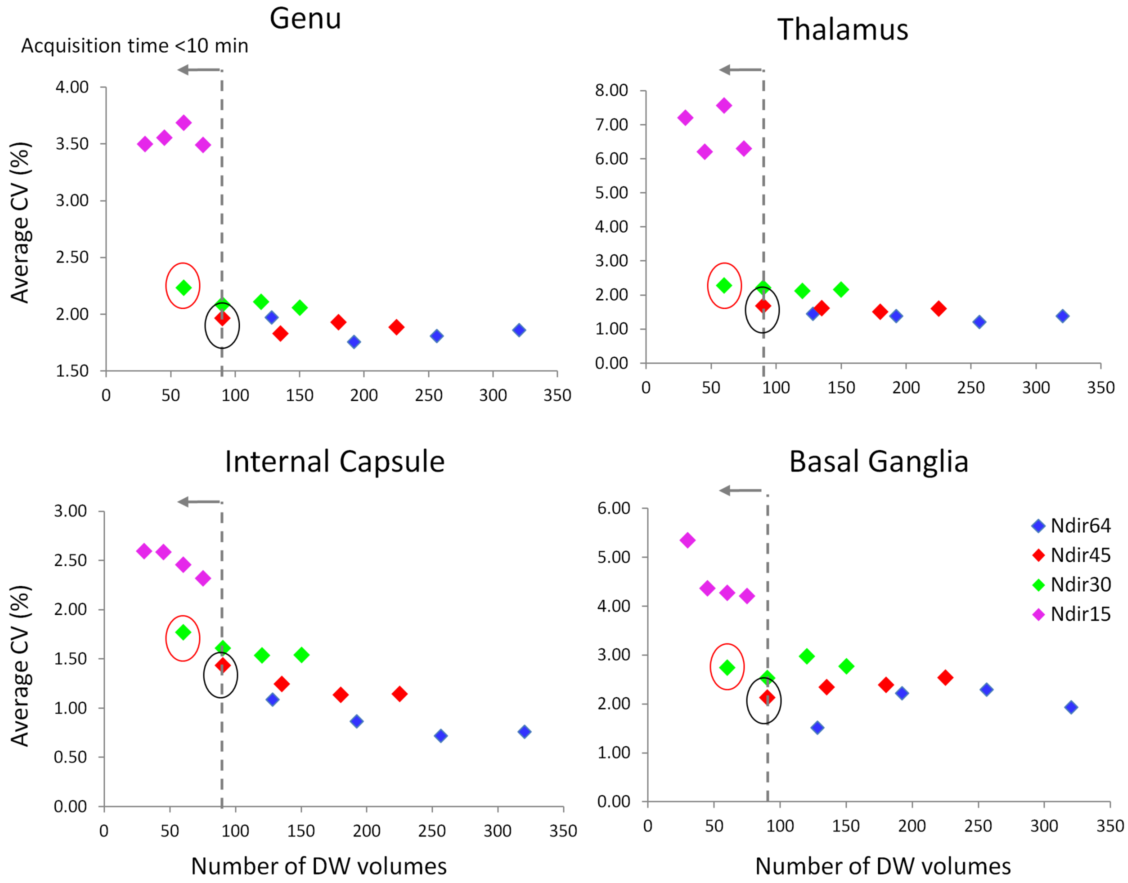

Figure 5.8. Average CVs for various imaging schemes in all ROIs. Number of diffusion weighted (DW) volumes is calculated as NDir × Nbval. For each NDir set, the imaging schemes Nbval2 → Nbval5 required longer acquisition time. Dotted line shows the preferred clinical acquisition limit of 10 min. The imaging scheme circled in red is the optimally efficient scheme with approximately 7 min of acquisition time (Opt7min). The one circled in black is an extended imaging scheme with approximately 10 min of acquisition time (Opt10min).

5.3.3 Experiment#3: Performance Evaluation of the Optimal Imaging Schemes

Methods: The initial assessment of the effect of b-values and diffusion directions were based on ROI analysis. Performance of the two optimal imaging schemes determined from Exp #2 (the Opt7min scheme with 30 diffusion directions, b = 1000, 2500 s/mm^2,

~7 min; and the Opt10min scheme with 45 diffusion directions, b = 1000, 2500 s/mm^2, ~10 min) were evaluated in this experiment at the whole-brain level within the GM and WM masks produced from the segmentation of whole brain, as described previously. The two optimal imaging scheme were compared to the gold standard 64 direction and 5 b-value set, the recommended 30 diffusion directions (the 5B30D scheme, ~17min) (Jensen et al., 2005; Helpern et al., 2011; Hui et al., 2008; Cheung et al., 2009) and a previously suggested short imaging scheme of 2 b-values (b = 1000, 2000 s/mm^2) and 30 diffusion directions (the 2B30D scheme, ~7min) (Jensen and Helpern, 2010; Tabesh et al., 2011).

Performance of the various imaging schemes were evaluated based on the accuracy and variability in estimated diffusion and kurtosis tensor parameters from repeated measurements. Different combinations of b-values and diffusion directions were picked out from each of the four complete DKI datasets to construct different imaging schemes. Let $\overline{S_\iota}$ and $\sigma(S_i)$ denote the mean and standard deviation for each parameter from 4 repeated acquisitions in voxel i. Then, the estimation accuracy was assessed by comparing percent bias voxel-wise to the gold standard (S_i^{gold}):

$$Bias_i = \frac{\overline{S_i} - S_i^{gold}}{S_i^{gold}} \cdot 100\%, \qquad i = 1, ..., N \tag{5.10}$$

where N is total number of voxels within a WM or GM mask. Estimation variability was assessed voxel-wise by the CV:

$$CV_i = \frac{\sigma(S_i)}{\overline{S_i}} \cdot 100\%, \qquad i = 1, ..., N \tag{5.11}$$

The distribution of CV_i and $Bias_i$ for each parameter was compared among various imaging schemes based on the median, 25th (Q_1) and the 75th (Q_3) percentile values, as well as the interquantile range (IQR = $Q_3 – Q_1$). The IQR is a measure for estimation variability as it represents the spatial variability of CV or Bias across brain voxels.

Results: Figure 5.9 shows representative *FA*, *MK* and K_r maps using the various imaging schemes from the first DKI acquisition compared to the gold standard. White arrows indicate the frontal lobe, where the most differences were observed for *MK* and K_r among the various imaging schemes. It is likely that the susceptibility-induced distortion from the sinus may have played a role for these observed differences. Residual misalignment in voxels across different diffusion directions, even after co-registration, caused a higher variability in estimating the kurtosis tensor in the frontal lobe. The variability in the estimates was reduced when using increased diffusion directions with the Opt10min scheme (45 diffusion directions) compared to all other 30 diffusion direction schemes. A similar reduction in variability was also observed in thalamus (yellow arrows in Figure 5.9) for K_r in the Opt10min scheme compared to other schemes. The Opt7min scheme with only 2 b-values produced similar maps to the much lengthier 5 b-value scheme (5B30D). The estimates were also better compared to the 2B30D scheme, when using a higher b_{max} of 2500 s/mm^2. The diffusion tensor estimation appeared to be minimally affected by the various imaging schemes as indicated by similar *FA* maps from the various imaging schemes.

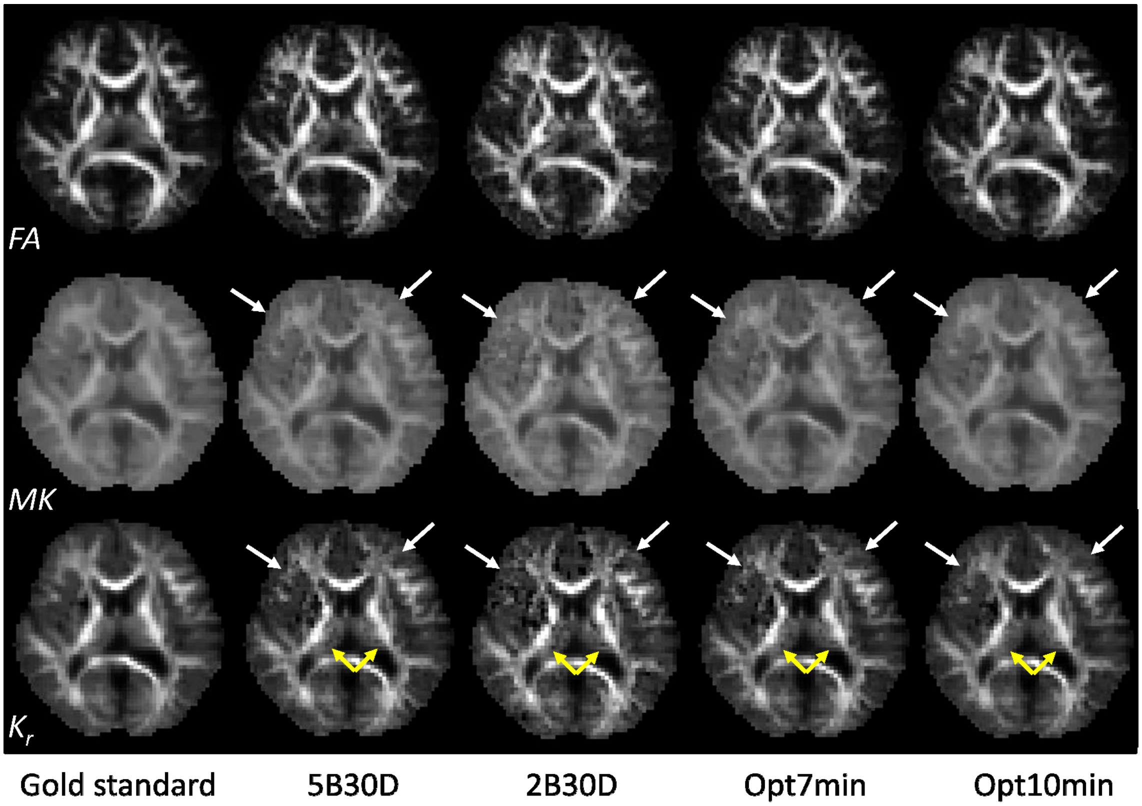

Figure 5.9. Representative FA, MK and K_r maps using various imaging schemes. White arrows (frontal lobe grey and white matter) and yellow arrows (thalamus) indicate regions showing large differences for various imaging schemes.

The variability in estimating diffusion and kurtosis parameters across repeated measurements using the various imaging schemes are shown in Figure 5.10. The distribution of the CVs for all voxels within the GM or WM masks is represented by their median CV, and the 25th (Q_1) and the 75th (Q_3) percentile CVs. Among different imaging schemes, the Opt10min scheme has the lowest median CV as well as the lowest IQR for all parameters in both GM and WM, indicating an overall lower variability in estimating the diffusion and kurtosis parameters. The Opt7min provides similar CV and IQR as the 5B30D scheme for MD and MK. For other parameters, the 5B30D scheme performs slightly better than the Opt7min scheme with the biggest difference being for the estimation of FA in GM, where the Opt7min has a 1.5% higher median CV and 0.73%

higher IQP compared to the 5B30D scheme. The 2B30D scheme had the highest median CV and IQP among all schemes and the effect was worse for kurtosis parameters in WM. In general, kurtosis parameters were found to have higher CVs than diffusion parameters and the only exception was *FA* in GM, which had the highest variability due to the inherent low diffusion anisotropy in GM.

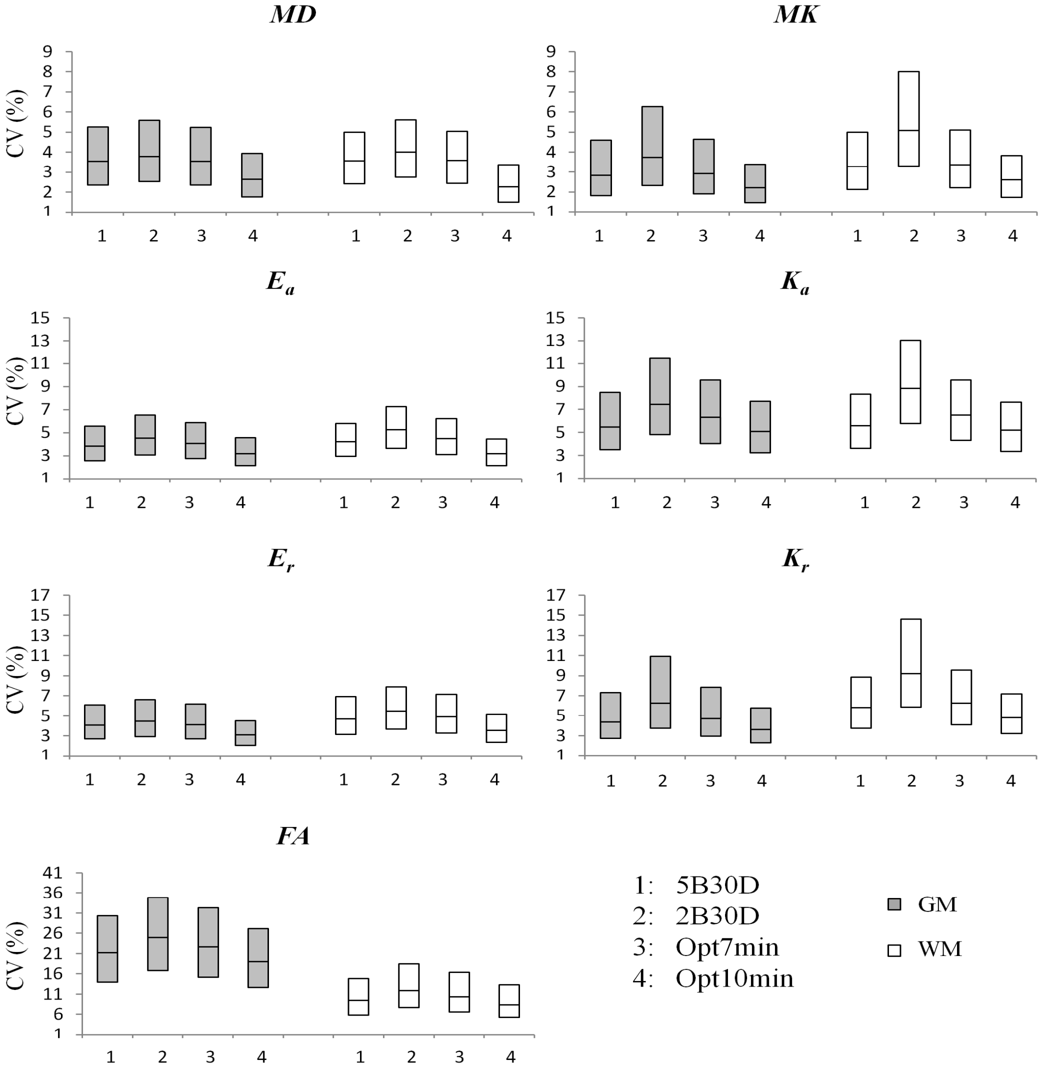

Figure 5.10. Estimation variability using different imaging schemes for all diffusion (*MD*, E_a, E_r, *FA*) and kurtosis parameters (*MK*, K_a, K_r). Each box shows median CV from repeated DKI acquisitions in GM and WM voxels. Upper and lower bounds of each box represent the 25th and 75th percentile values of CV.

The estimation accuracy of the various imaging schemes was evaluated by the average percent bias of four DKI acquisitions compared to the gold standard. Figure 5.11 shows the distribution of average bias for different diffusion and kurtosis parameters in all GM and WM voxels. The 2B30D scheme is not included in the graph since it exhibited a much higher bias compared to the other three schemes due to its b_{max} (2000 mm/s^2 vs. 2500 mm/s^2 for all other). The 5B30D scheme exhibited the least bias (closer to 0) for all kurtosis parameters in both GM and WM, and for diffusion parameters (except *FA*) in GM, indicating the benefit of using increasing number of b-values for accurate estimation. For diffusion parameters in WM and *FA* in both WM and GM, the Opt10min scheme provided slightly lower bias than the 5B30D scheme, indicating that the anisotropic diffusion (typical in WM) were better measured by more diffusion directions. The Opt10min scheme also has the lowest spatial variability in bias across brain voxels (lower IQP) for all parameters in both GM and WM, indicating that the estimation bias for the Opt10min scheme is likely systematic, due to the choice of b-values. The Opt7min showed higher percent bias (~1% in diffusion parameters and 2% in kurtosis parameters compared to the 5B30D scheme; ~0.5% in all parameters compared to the Opt10min scheme), as well as a higher variability in bias compared to the Opt10min scheme (IQP ~ 0.5% higher for diffusion parameters and 1% higher for kurtosis parameters). Generally biases were much higher in the kurtosis parameters than the diffusion parameters. *MK*, K_r and *FA* showed strong yet systematic negative bias, while *MD* and E_a appeared to have positive bias for various imaging schemes. Compared to the gold standard, which was averaged across four repetitions equivalent to doubling the SNR, the bias observed in the optimal schemes appear to be mainly noise related and is explored in greater detail in section 5.3.5.

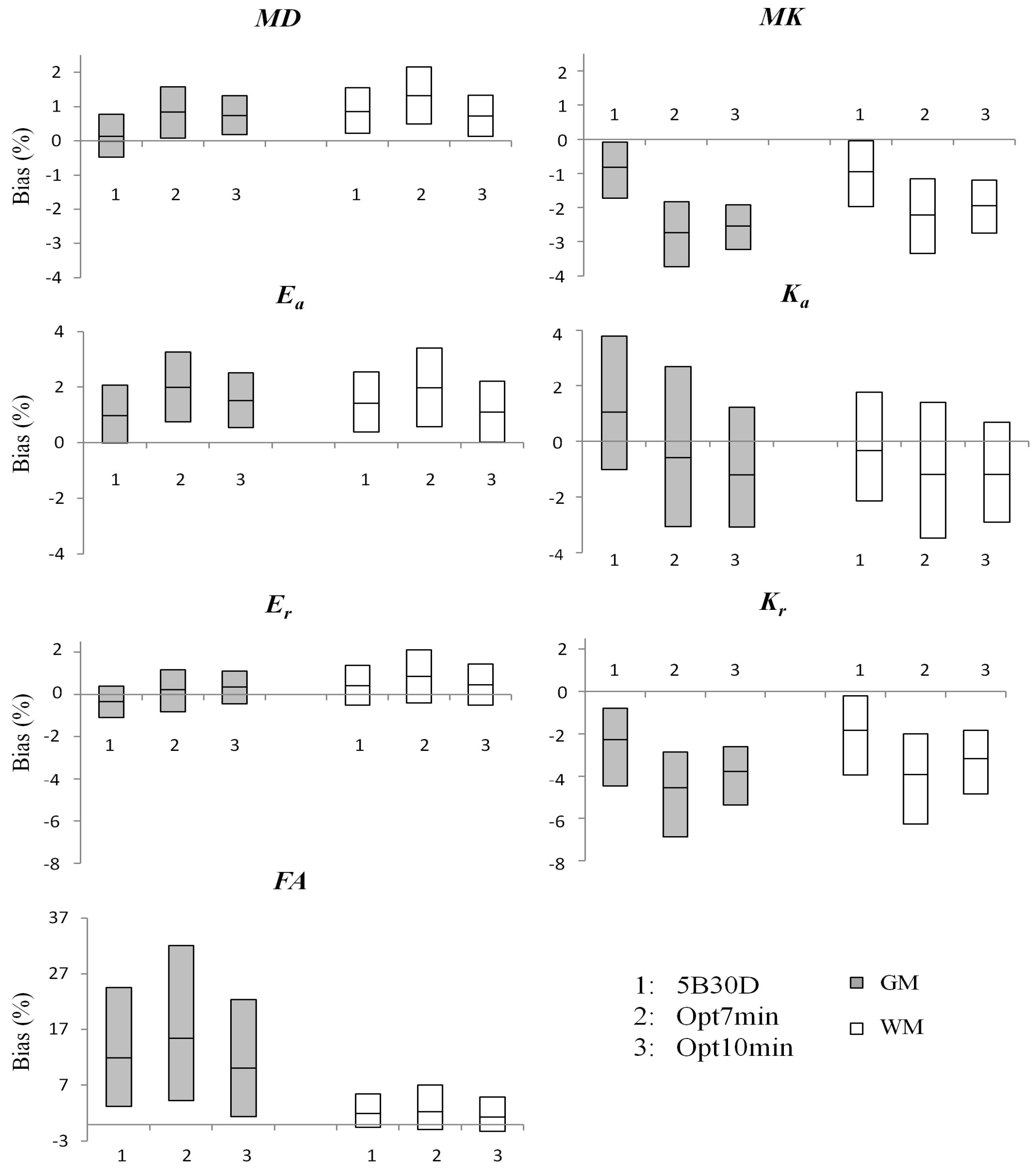

Figure 5.11. Average percent bias compared to the gold standard for four DKI acquisitions in GM and WM voxels, for all diffusion and kurtosis parameters using various imaging schemes. Boxes show the median, 25th and 75th percentile values of the bias.

5.3.4 Experiment#4: Effect of Reconstruction Methods on Parameter Estimates

Methods: Experiments 1-3 used the constrained least squares method (CLS) in estimating the parameters. CLS restricts the diffusion coefficient to be non-negative ($D_{app}(\mathbf{g}) \geq 0$, constraint 1), the diffusion kurtosis to be non-negative ($K_{app}(\mathbf{g}) \geq 0$, constraint 2), and the diffusion weighted signal to be a monotonically decaying function with increasing b-value, which is equivalent to kurtosis values not being too high ($K_{app}(\mathbf{g}) \leq K_{max}(\mathbf{g})$, constraint 3), for all diffusion directions **g**. In this experiment, the effect of constrained fitting is studied for the optimal imaging schemes (Opt7min and Opt10min schemes) and compared to the 5B30D and the 2B30D schemes. The susceptibility of the various imaging schemes to constraint violations (as described in section 5.2.3) is assessed by counting voxels violating the constraints when only LS is used. A voxel is considered as violating a constraint if the diffusion coefficient or kurtosis of any one of the diffusion directions violates the constraint. How constrained fitting affects the derived parameter variability and bias was further assessed by calculating the difference in CV and absolute Bias using CLS and LS voxel-wise:

$$\Delta CV_i = CV_i^{LS} - CV_i^{CLS} \qquad i = 1,\ldots,N \tag{5.12}$$

$$\Delta Bias_i = \left|Bias_i^{LS}\right| - \left|Bias_i^{CLS}\right| \qquad i = 1,\ldots,N \tag{5.13}$$

A positive ΔCV_i ($\Delta Bias_i$) indicates an improvement from using CLS, while a negative ΔCV_i ($\Delta Bias_i$) indicates a worse performance using CLS compared to LS.

Results: Unconstrained fitting (LS) can lead to erroneous results as shown in the *MK* maps (Figure 5.12). The *MK* and *FA* maps shown are from a same axial slice using the 2B30D scheme reconstructed with LS and CLS methods (no Gaussian smoothing was used to magnify the effect when these constraints are violationed). The unconstrained *MK* map shows many negative values (black holes) scattered in the corpus callosum and the frontal lobe WM (especially at the tissue junctions of WM and GM), where high kurtosis values are expected due to higher tissue complexity of the WM. These negative *MK* values in WM are mainly due to highly restricted diffusion along the radial direction of the axons, while negative *MK* values in GM/WM tissue junctions are thought to be due to the tissue misalignment across different diffusion directions. By using constrained fitting, these 'black holes' in *MK* map are avoided resulting in values closer to the surrounding tissues. The fitting errors are much less noticeable in the *FA* map as those unconstrained voxels typically end up (erroneously) as highly anisotropic voxels and is, consistent with the generally high *FA* observed in WM.

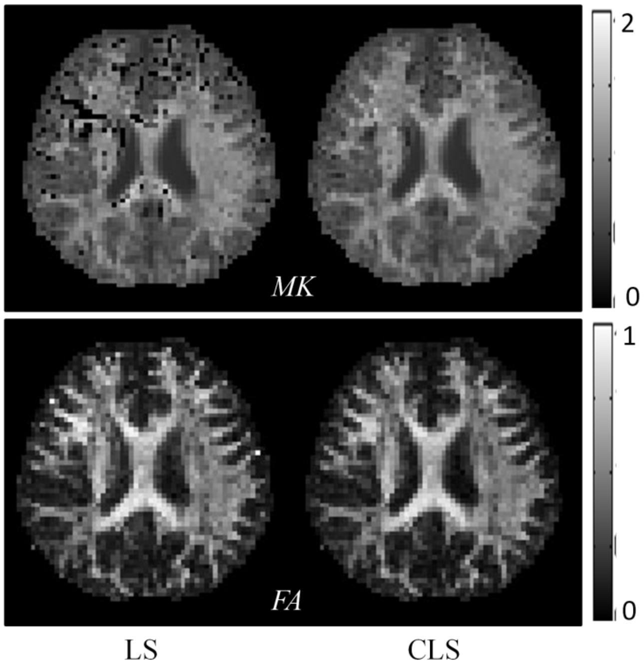

Figure 5.12. Representative *MK* and *FA* maps of a same axial slice using the 2B30D scheme reconstructed with LS and CLS methods. The effect of constraint violations was magnified by having the diffusion weighted volumes undergo all pre-processing steps except Gaussian smoothing, resulting in lower image SNR.

The effect of constraint violations as shown in Figure 5.12 is most noticeable and prevails with low SNR. Even with Gaussian smoothing, 6.35% of WM voxels and 2.65% of GM voxels still have negative kurtosis values (violations of constraint 2) using the 2B30D scheme (Table 5.2). Voxels with negative diffusion coefficient (violations of constraint 1) were rare (< 0.1% of all voxels) for any of the imaging schemes. Although several voxels had very high kurtosis (violations of constraint 3), it is difficult to observe them in the brain tissue. However, a significant number of voxels appeared to have high kurtosis in the CSF. This is most likely due to the high diffusion coefficient in CSF, as it is very similar to free water. Violations of constraint 3 were also observed in approximately 12% of GM voxels and approximately 19% of WM voxels even in the gold standard dataset when only LS was used. A comparison among different imaging schemes shows that the Opt10min scheme has the least number of voxels with negative kurtosis, followed by 5B30D, Opt7min, and 2B30D schemes. The 2B30d scheme had the least number of voxels with kurtosis values being fitted too high due to its lower maximum b-value (b_{max} = 2000 s/mm^2), compared to all other schemes that used a high b-value of 2500 s/mm^2. Among the other three schemes, the Opt10min scheme demonstrated to be less sensitive to erroneously fitting voxels to a high kurtosis value, followed by the 5B30D and then the Opt7min imaging schemes.

Constraint	**Percent voxel violations in GM (%)**				
	Gold Standard	**5B30D**	**2B30D**	**Opt7min**	**Opt10min**
#1	0	0.03 ± 0.06	0.06 ± 0.13	0.05 ± 0.10	0.05 ± 0.09
#2	0.23	0.76 ± 0.77	2.65 ± 1.52	0.93 ± 0.83	0.47 ± 0.32
#3	12.10	20.17 ± 2.95	8.18 ± 2.46	20.62 ± 2.98	16.73 ± 1.64
#1 ∪ #2 ∪ #3	12.33	20.68 ± 3.25	10.43 ± 3.37	21.22 ± 3.21	17.08 ± 1.82

Constraint	**Percent voxel violations in WM (%)**				
	Gold Standard	**5B30D**	**2B30D**	**Opt7min**	**Opt10min**
#1	0	0.01 ± 0.01	0.02 ± 0.05	0.02 ± 0.03	0.00 ± 0.00
#2	0.05	1.36 ± 0.88	6.35 ± 2.70	1.90 ± 1.12	0.75 ± 0.43
#3	19.46	30.88 ± 6.66	13.70 ± 3.74	31.57 ± 6.42	24.70 ± 3.08
#1 ∪ #2 ∪ #3	19.50	31.74 ± 6.68	19.02 ± 5.17	32.70 ± 6.59	25.21 ± 3.21

Constraint	**Percent voxel violations in CSF (%)**				
	Gold Standard	**5B30D**	**2B30D**	**Opt7min**	**Opt10min**
#1	0	0.00 ± 0.01	0.10 ± 0.20	0.04 ± 0.08	0.00 ± 0.01
#2	0.01	0.47 ± 0.94	0.53 ± 1.06	0.39 ± 0.78	0.41 ± 0.59
#3	82.31	89.25 ± 0.50	54.41 ± 5.80	89.91 ± 0.85	87.72 ± 1.02
#1 ∪ #2 ∪ #3	82.32	89.68 ± 1.09	54.75 ± 6.35	90.15 ± 1.18	88.02 ± 1.21

Table 5.2. Percent voxel violations of various constraints in different brain tissues (GM, WM, CSF) for different imaging schemes. Values shown are mean ± 1 standard deviation for the four DKI repetitions.

Using CLS, as opposed to LS, provides an overall lower CV and a lower averaged estimation bias across several repetitions of DKI acquisitions, for all parameters and using all imaging schemes. Figure 5.13 shows the reduction in CV and bias in all GM and WM voxels when CLS was used for the Opt10min scheme (plots for other schemes are similar and not shown here). The box plots show the median value and the 25th, 75th percentile ranges of the reduction in CV (ΔCV) or bias (ΔBias) across voxels within the GM and WM mask when CLS was used in comparison to LS method. Only voxels with constraint violations were considered here in arriving at these estimates. All diffusion parameters benefitted from the constrained fitting, indicated by a positive ΔCV and ΔBias. The kurtosis parameters demonstrated a general reduction in CV when using CLS.

However, there was little change in the estimation bias estimate whether using CLS or LS. Therefore, although CLS reduced the fitting variability for kurtosis parameters, the estimation accuracy was not affected. Possibility lays that while CLS generally serves to reduce fitting bias, it may also cause more bias for some voxels (as will be shown in the next section).

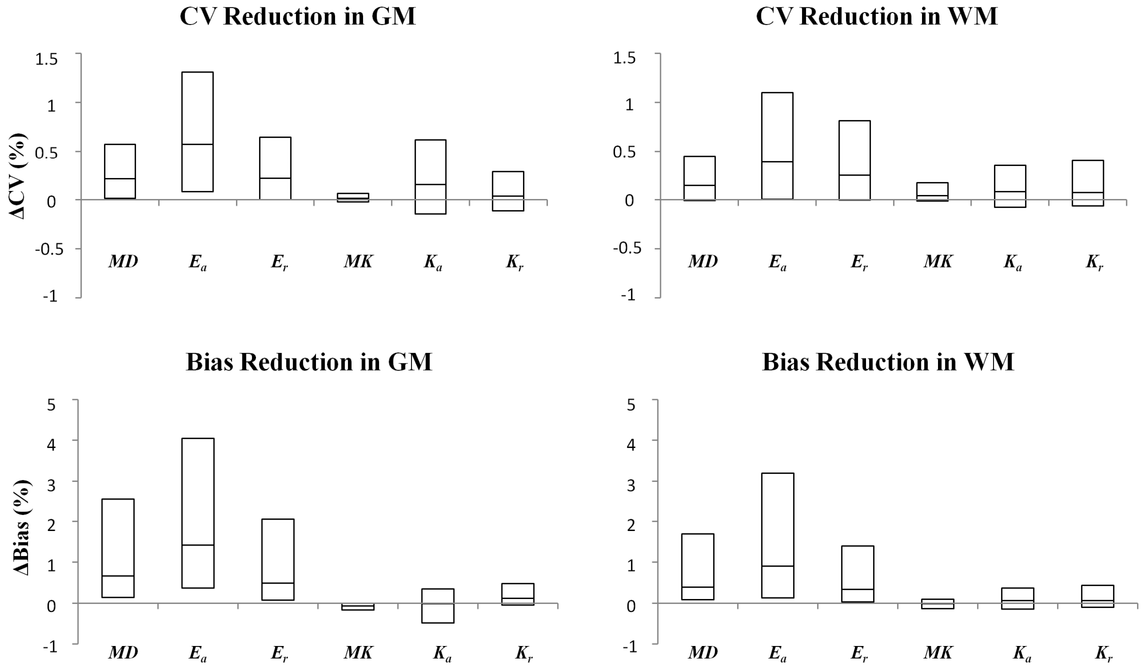
CV Reduction in GM

CV Reduction in WM

Bias Reduction in GM

Bias Reduction in WM

Figure 5.13. Reduction in CV and bias in all GM and WM voxels when constrained fitting (CLS) is used compared to the unconstrained fitting (LS) for the Opt10min scheme. Boxplots show the median value, the 25th and 75th percentile values of the difference in CV and bias (LS – CLS).

5.3.5 Experiment#5: Effect of Image Noise on DKI Estimates

Methods: Monte Carlo simulations were conducted to study the effect of noise in the acquired data for DKI estimation using various imaging schemes (5B30D, Opt7min and

Opt10min). Rician noise was added to the gold standard diffusion weighted signal from genu and thalamus (representative of WM and GM, respectively), with SNRs ranging from 5 to 40 (with a step size of 2.5). For each SNR level, 1000 runs of Monte Carlo simulations were conducted to generate Gaussian noise ($n \sim N(0,1/SNR)$). To simulate additive Rician noise to the gold standard data *(S)*, the noisy dataset *(S_n)* was generated as follows:

$$S_n = \sqrt{(S+n)^2 + n^2} \tag{5.14}$$

Diffusion and kurtosis tensors are then reconstructed from subsets of the noisy data using each of the imaging schemes. The effect of noise was assessed using both the CLS and LS reconstruction methods. The median parameter value from 1000 simulations for each SNR was compared to the gold standard to evaluate estimation bias. The estimation variability was assessed using a percentile based CV calculated as:

$$CV_p = \frac{Q_3 - Q_1}{2Q_2} \tag{5.15}$$

where Q_1, Q_2, Q_3 are the 16th, 50th, 84th percentile values for each parameter. $(Q_3 - Q_1)/2$ is analogous to the standard deviation, and Q_2 is analogous to the mean, in a Gaussian distribution. This percentile-based formula is chosen due to its robustness against outliers, i.e., huge erroneous values in the distribution.

Results: Noise in the data may lead to violation of the various constrains during DKI estimation. Figure 5.14 shows constraint violations under simulated additional Rician noise, with an SNR ranging from 5 to 40 in the genu (a) and the thalamus (b) for various imaging schemes. Violations of constraint 1 ($D_{app}(\mathbf{g}) < 0$) is almost non-existent (<1% from 1000 runs) when SNR is ≥ 10 for both the genu and the thalamus. Violations of constraint 2 ($K_{app}(\mathbf{g}) < 0$) was much more evident in the data with increased noise. Even at SNR of 20, more than 6.4% of the runs in the genu and 10.1% of the runs in the thalamus returned negative kurtosis values. The Opt7min scheme had the most violations of constraint 2, while the 5B30D and the Opt10min schemes performed similarly but with lesser number of violations. The SNR in the raw images plays an important role in causing negative kurtosis values as the rate of violation reduces sharply when SNR increases. Simulations reveal that SNR of 30 or greater can ensure minimal erroneous fitting that leads to negative kurtosis in pixels (<1%).

Runs related to violations of constraint 3 ($K_{app}(\mathbf{g}) \geq K_{max}(\mathbf{g})$) were persistently more than 93% for all imaging schemes in the genu, although fewer diffusion directions were affected when SNR increased. But, even at an SNR of 40, on average, approximately 10% of diffusion directions were still affected. This indicates that areas of free diffusion can erroneously be classified as regions of very high kurtosis regardless of the noise characteristics of the image. In the thalamus where diffusion is mildly restricted in all directions, violations of constraint 3 decreases with increased SNR. Violations of constraint 3 were more common than the other two constraints, but were least observed using the Opt10min scheme, followed by the 5B30D scheme and then the Opt7min scheme. Overall the Opt10min scheme appeared to be least susceptible to constraint violations. The Opt7min scheme had more violations than the 5B30D scheme (at a typical SNR level of 25 for Opt7min vs. 5B30D, violation of constraint 2 was: 2.8% vs. 1.4% in genu and 5.4% vs. 1.9% in thalamus; violation of constraint 3 was: 98.7% vs. 97.7% in genu and 30% vs. 20.1% in thalamus).

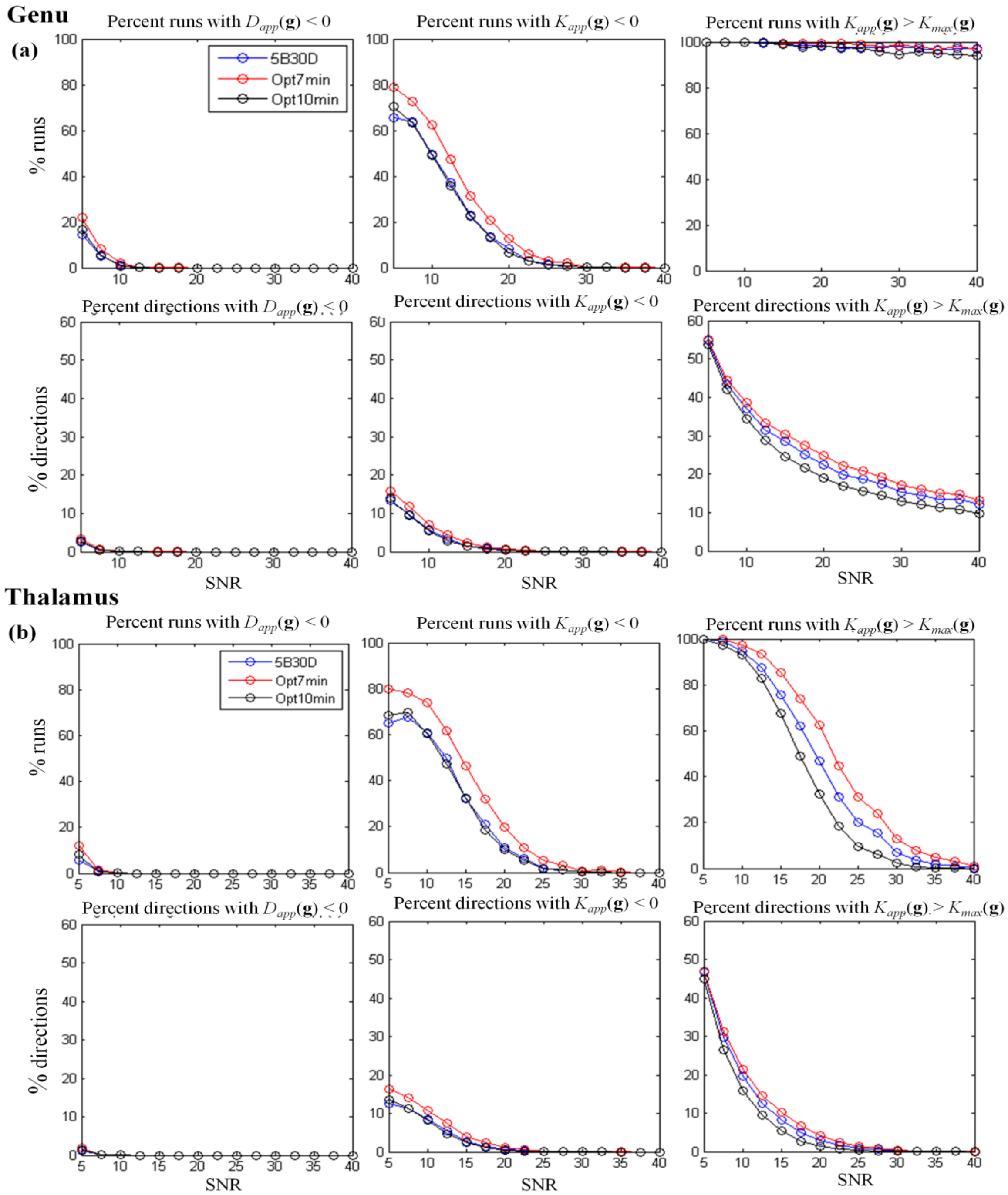

Figure 5.14. Comparison of different imaging schemes under simulated noise with an SNR of 5 to 40 in the genu (a) and the thalamus (b) in terms of constraint violations. Top row shows percent of iterations from the 1000 Monte Carlo simulations that violated the 3 constrains. Bottom row shows average percent directions that violated each constraint.

The effect of noise on the accuracy and variability in estimating kurtosis parameters is shown in Figure 5.15 for the genu (a) and the thalamus (b) with different imaging schemes (5B30D, Opt7min and Opt10min) and the two reconstruction methods used (LS and CLS). For both the genu and the thalamus, K_a appears to be overestimated, while K_r and MK appear to be underestimated as SNR decreases. The positive bias in K_a is mainly due to the kurtosis value being fitted too high (violations of constraint 3), since the axial direction is where the highest diffusion occurs. The negative bias in K_r is mainly due to negative kurtosis values (violations of constraint 2) where diffusion is highly restricted in the radial direction of the axons. As the negative kurtosis values can easily be huge, this also dominates the fitting bias for MK. In the thalamus, where the diffusion is largely isotropic, the error in fitting the radial or axial kurtosis can be quite large. The bias for MK and K_r may also change directions with extremely low SNR (<10), when the radial or axial direction becomes even more ambiguous and violations of constraint 3 dominate, leading to overestimated kurtosis values.

In general, CLS greatly reduces fitting errors, over LS, for all parameters, as indicated by a lower CV among the 1000 simulated runs, and by less error for fitted parameter values compared to the gold standard. In thalamus, where constraint violations reduce to zero when SNR increases, values fitted by CLS and LS also merge. In genu, on the other hand, due to the persistently high level of violations to constraint 3, values fitted by CLS and LS continue to be different even at SNR = 40. This leads to the increased bias for K_a in genu with CLS. Among the three imaging schemes, the Opt7min has the highest fitting variability (higher CVs), while the 5B30D scheme has the lowest bias for both genu and thalamus, consistent with previous findings in WM and GM voxels (section 5.3.3).

The effect of noise on diffusion parameters is shown in Figure 5.16. The estimation bias in the diffusion parameters is generally lower than the kurtosis parameters. The estimation bias exceeds beyond the 5% bound only when SNR is less than 15 for *FA* and λ_a in genu. For thalamus, λ_a, λ_r and *FA* are inherently erroneous due to the low diffusion anisotropy in thalamus. CLS again reduces estimation variability (lower CV) for the diffusion parameters than LS, although to a lesser degree than for kurtosis parameters. The difference between the different imaging schemes in estimating diffusion parameters is very small in terms of both the fitting variability (CV) and bias. Interestingly though CLS changes the direction of bias in λ_a, *MD* and *FA* in genu toward low SNR compared to LS. Toward low SNR, λ_a, *MD* and *FA* in genu tend to be overestimated using LS but underestimated using CLS.

(a) Genu

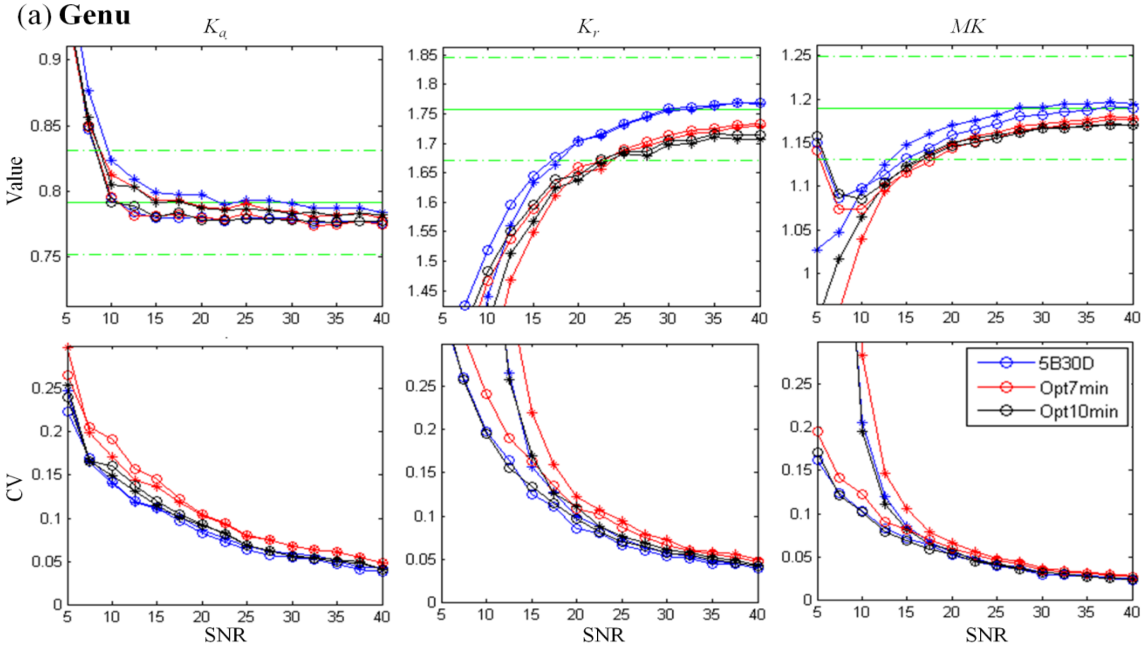

(b) Thalamus

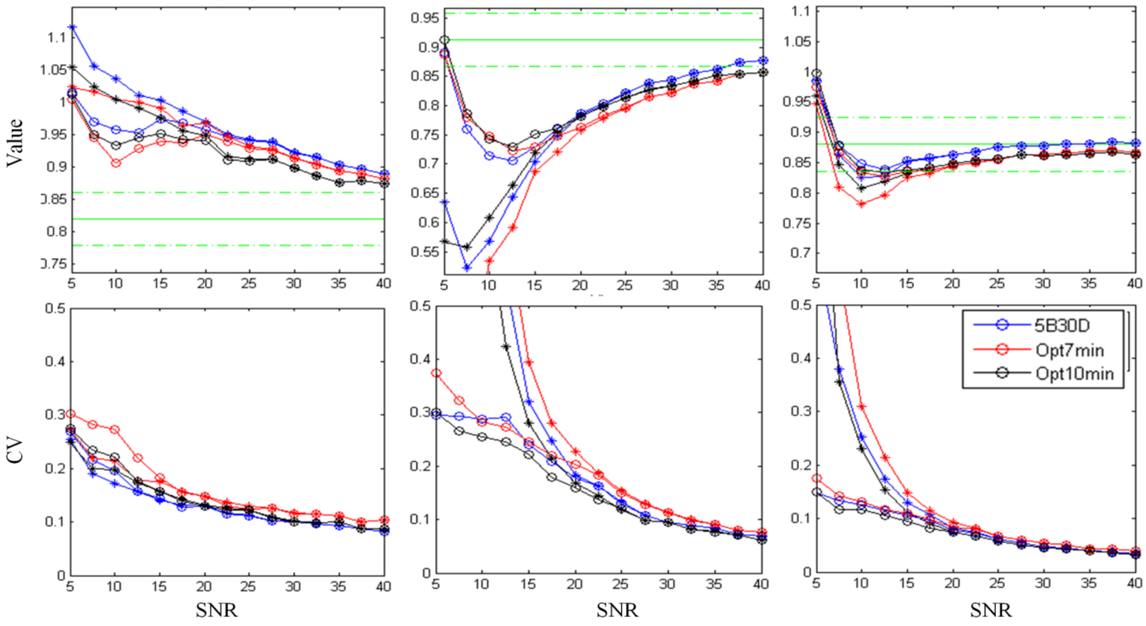

Figure 5.15. Comparison of different imaging schemes (5B30D, Opt7min and Opt10min) and reconstruction methods (LS = * and CLS = ○), under simulated noise with SNR of 5 to 40 in genu (a) and thalamus (b), for kurtosis parameters. The top row is the median values and the bottom row is the coefficient of variation (CV) from 1000 simulations. The green line is the gold standard value, and the dotted line is ±5% of the gold standard value.

(a) **Genu**

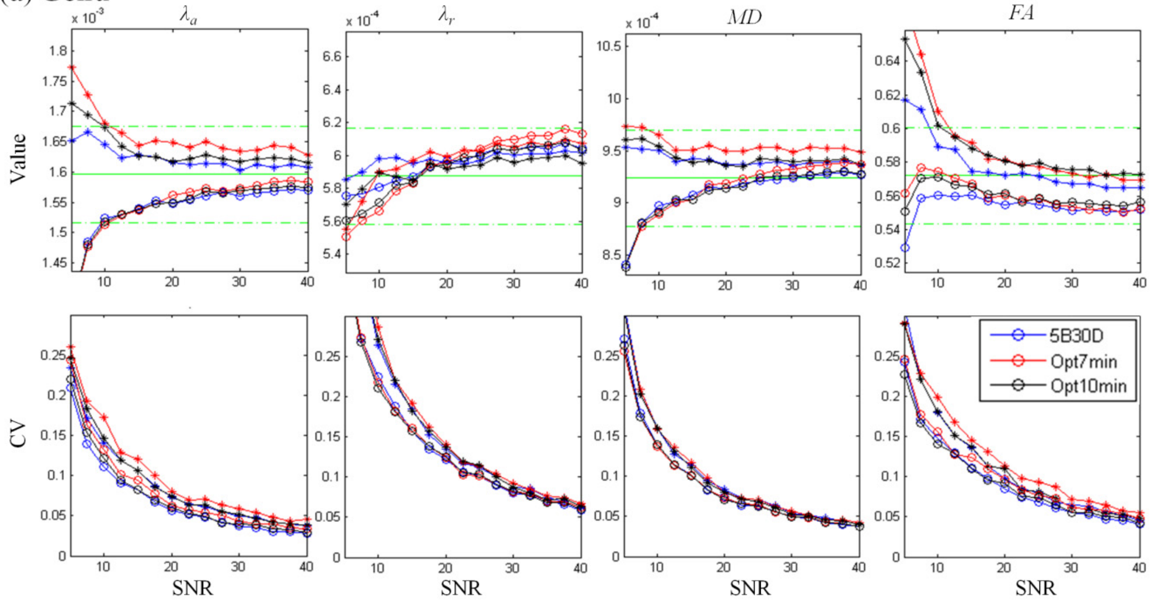

(b) **Thalamus**

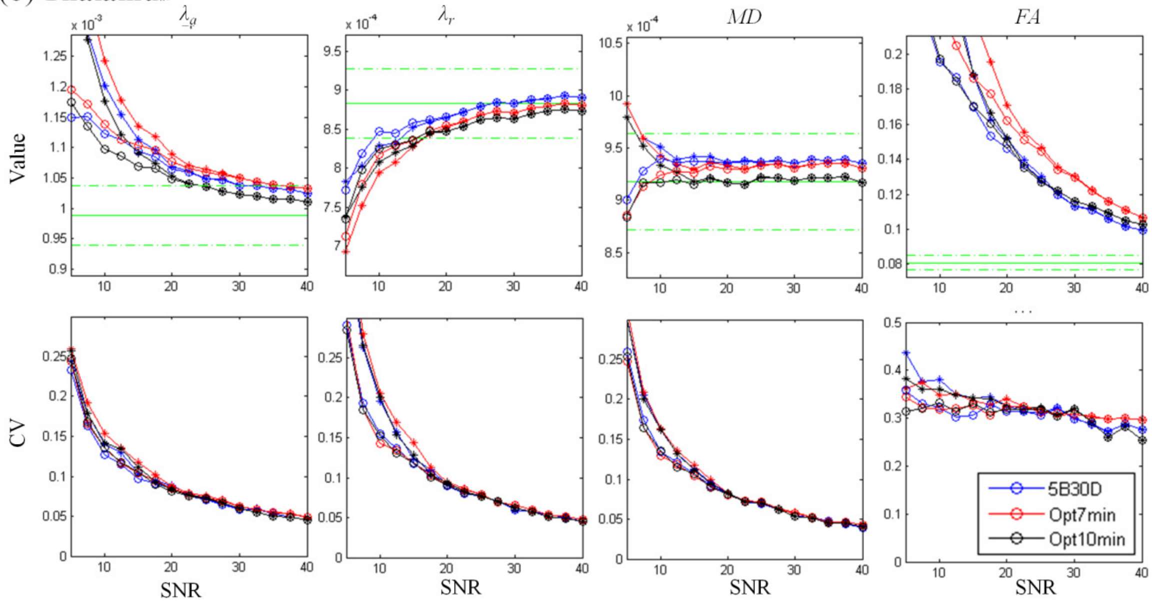

Figure 5.16. Comparison of different imaging schemes (5B30D, Opt7min and Opt10min) and reconstruction methods (LS = * and CLS = ○) under simulated noise with an SNR of 5 to 40 in genu (a) and thalamus (b) for the diffusion parameters. The top row is the median values and the bottom row is the CV from 1000 simulations. Green line is the gold standard value and the dotted line showed ±5% of the gold standard value. Values for *MD*, λ_a and λ_r are of unit mm^2/s.

5.4 Discussion

The use of very high diffusion-weighting (b-values) in a diffusion weighted imaging sequence allows the probing of water diffusion over very short molecular distances and hence can be sensitive to the tissue microstructure. However, the signal received from such sequences is inherently starved for signal to noise. Diffusion kurtosis relies on multiple diffusion weightings, including the use of very high diffusion weighting or very high b-values. The scans can be very long due to the use of multiple diffusion weightings and multiple directions and sometimes are clinically impractical. However, the wealth of information that it can provide regarding the tissue microstructure begs for a better understanding of the technique and ways to minimize the scan time so that it can be clinical useful and yet be accurate.

The experiments performed in this study demonstrate that an efficient DKI imaging scheme with only two nonzero b-values can provide comparable bias and variability in estimating diffusion and kurtosis parameters as that obtained from a 64 direction scheme employing 5 separate diffusion weighting (or 5 b-values). This amounts to a 60% decrease in acquisition time, which allows for the practical application of DKI acquisitions on clinical patients. Although unproven until now, this study also confirms a prior suggestion of the feasibility of an efficient DKI acquisition scheme for whole brain coverage (Jensen and Helpern, 2010; Tabesh et al., 2010). Both the regional and whole-brain analysis indicate that more b-values have little effect on reducing the variability in the estimated DKI parameters. However, this comes with a cost of losing some estimation accuracy compared to data obtained with five b-values. The maximum b-value

(b_{max}) used appears to have a direct impact on the estimation of DKI parameters. The kurtosis parameters (K_a, K_r, MD) estimated with a b_{max} of 2000 s/mm^2 showed a positive bias compared to the ones estimated with a b_{max} of 2500 s/mm^2, as well as a higher estimation variability. On the other hand, even though diffusion parameters (λ_a, λ_r, MD) are b-value dependent in DTI (Jones and Basser, 2004; Andersson et al, 2008), their estimation was not affected by the choice of b_{max} in DKI. This confirms the findings by Veraart et al., who observed that diffusion tensor parameters were more accurately estimated using the DKI model (Veraart et al., 2011). Although a b_{max} of 2500 s/mm^2 is preferred over 2000 s/mm^2, diffusion weighted images at b-value of 2500 s/mm^2 are of lower signal intensity and are more susceptible to noise. The SNR for our data in the unsmoothed b_0 images is mostly more than 20 (about 20-35 in WM and 20-50 in GM). If lower SNR would be expected from a given acquisition, a b_{max} of 2000 s/mm^2 should be recommended for DTI estimation Lu et al. (Lu et al., 2006).

The number of diffusion directions was found to have a significant effect on the variability in DKI estimation. In order to estimate the kurtosis tensor, a 4th order tensor with 15 independent elements, a minimum of 15 diffusion directions is required (Lu et al., 2006). But, with such a minimal diffusion direction number, the estimated kurtosis parameters are highly variable. A significant reduction in estimation variability was observed when 30 diffusion directions were used compared to 15. A further extension to 45 diffusion directions provided even lower estimation variability. This led to an extended imaging scheme with 45 diffusion directions that can still fit in the 10 min clinically feasible acquisition time (with 2 nonzero b-values). The findings that kurtosis tensor estimation benefits more from increased number of diffusion directions than the increased number of b-values is analogous to a general understanding in diffusion tensor estimation, where a single nonzero b-value and an abundance of diffusion directions are recommended over limited diffusion directions and many b-values (Jones et al., 1999; Landman et al., 2008). Even though 30 diffusion directions are only twice as many as the independent elements in the kurtosis tensor, it provides reasonable accuracy in estimating the kurtosis parameters in our experiments. One important aspect of this finding is the formula used to calculate the kurtosis parameters is already based on elliptical integration (Tabesh et al., 2010), where MK is the average kurtosis integrated over the whole sphere, and K_r is the average kurtosis integrated over a 2D plane perpendicular to the principle direction of the diffusion tensor. More diffusion directions are required if a full characterization of the 4th order kurtosis tensor is desired. The different diffusion directions used had very little affect on the derived diffusion parameters, because even the minimal set of 15 directions and 2 nonzero b-values provided enough redundancy for the 6 parameter diffusion tensor estimation.

Overall the most efficient imaging scheme for both diffusion and kurtosis parameter estimation was found to be the two nonzero b-value (b = 1000, 2500 s/mm^2) and 30-diffusion-direction scheme (the Opt7min scheme), which requires an acquisition time of approximately 7 min for whole brain coverage. This acquisition is 2.5 times shorter in duration compared to the frequently used imaging scheme of 5 nonzero b-values and 30 diffusion directions (the 5B30D scheme), and yet provides only a marginal increase in variability and bias in its diffusion and kurtosis estimates. A slightly longer imaging scheme uses the same 2 b-values and 45 diffusion directions (the Opt10min scheme), requires 10 minutes to acquire the data and lowers the estimation variability than the 5B30D scheme, but with a slightly higher bias in the estimated parameters. But the bias in the Opt10min scheme appeared to be systematic, with a lower spatial variability across WM and GM voxels than the 5B30D scheme. This lower inherent variability in DKI estimation with the Opt10min scheme may be preferred when conducting studies that seek to compare group-wise parametric values with the same imaging scheme (i.e. at the same level of systematic bias).

For DKI reconstruction, constraints play an important role in ensuring that the diffusion and kurtosis parameters are physically meaningful in the context of the microstructure of the underlying tissue (Tabesh et al., 2010; Veraart et al., 2011). Among the three types of constraints applied in this study, negative diffusion coefficient (violations of constraint 1) was rare (less than 0.2% brain voxels). Negative kurtosis values (violations of constraint 2) were observed in as much as 7% and averaged about 1-2% of whole brain voxels. Kurtosis values over the maximum limit (violations of constraint 3) were observed in as many as 30% of WM, 20% of GM and 90% of CSF voxels. Violations of constraints 1 and 2 usually reduces in number when SNR increases, as indicated from a low number of violations found in the gold standard data and from the Monte Carlo simulation for SNR. However, violations of constraint 3 appeared to be inevitable, even in the gold standard dataset or with high SNR. Note that the numbers of voxels that violated these constraints are much lower than reported in Veraart et al. (Veraart et al., 2011). The reason may be that our data were smoothed prior to DKI reconstruction. A Gaussian smoothing with a FWHM (3mm) of only 110% of the voxel size (2.7mm) increased the image SNR by approximately 70% by reducing the noise standard deviation.

Although constrained DKI fitting (CLS) improved the accuracy and reduced variability in estimating diffusion and kurtosis parameters, some caution needs to be exercised when interpreting results from CLS. Constrained fitting mainly replaces erroneous parameter values with the upper or lower bound set for that parameter. To replace a negative diffusion coefficient with zero is probably reasonable, because negative diffusion coefficient appears where diffusion is highly restrictive and has very low diffusion coefficient. However, it is not entirely correct to replace a negative kurtosis with zero when the real kurtosis should be higher, as is typical in directions exhibiting high diffusion restriction and complex cellular structures. Nor is it correct to replace too high a kurtosis value with the maximum value when the real kurtosis should be almost zero, as is typical in directions with free diffusion. These simplistic but insufficient corrections for kurtosis values produce large negative bias in K_r and MK in white matter when SNR is low, because negative kurtosis values are only corrected to approximately zero instead of a high value more representative of the generally high complexity in white matter. They also result in the positive bias in K_a in white matter, where kurtosis values along the axons are estimated to be falsely high instead of the near zero value that is more representative of free diffusion. Our study clearly depicts that correcting for these three constraints significantly increases the accuracy and bias in the estimates. Further, it also favors schemes with more diffusion directions (the 2B45D scheme), which produce the least number of constraint violations, over schemes with more b-values (the 5B30D schemes).

Overall kurtosis parameters are more susceptible to noise than diffusion parameters, mainly in estimation bias. Bias in estimating diffusion parameters only becomes significant (>5% change from value at SNR=40) when SNR is 15 or lower. High bias also only appears in the radial diffusivity (λ_r) in white matter like genu, which is inherently more variable due to the low diffusivity perpendicular to the axons. Bias in estimating kurtosis parameters was significant for K_r (with SNR < 20) and *MK* (with SNR < 15). Interestingly, CLS changed the bias behavior *FA*, *MD* and λ_a compared to LS. The positive bias in *FA* using LS, and negative bias in *FA* using CLS at very low SNR (<20), is similar to that observed by Landman et al. (Landman et al., 2008). For *MD* and λ_a, the CLS fitted values showed a similar trend of bias with lower SNR as other DTI studies (Farrel et al., 2007; Landman et al., 2007).

The reconstruction methods considered in this study are restricted to linear least squares fitting only. Although non-linear least squares method was originally used for DKI model fitting (Jensen et al., 2005; Lu et al., 2006), they are time inefficient for image reconstruction (~90 min for a typical brain data set) and do not necessarily offer a significant benefit over the linear least squares method (as described in Chapter 3). Nevertheless, if image SNR is extremely poor (<20), it is possible that the non-linear methods may offer some advantages. Furthermore, although constrained fitting is important, the unconstrained linear least squares (LS) method has a computation time comparable to the normal DTI reconstruction and hence can be a good option if real-time reconstruction is required in a typical clinical setting.

5.5 Conclusion

In this study, an optimally efficient DKI imaging scheme was determined (b = 1000, 2500 s/mm^2 and 30 diffusion directions) to require only 7 min to obtain data from the whole brain. A slightly longer imaging scheme of the same two b-values but with 45 diffusion directions was shown to provide less variable parameter estimates than the most frequently used DKI imaging scheme (5 b-values and 30 diffusion directions), with a 50% reduction in acquisition time (~10 min). Kurtosis parameters are more prone to noise and fitting bias than the diffusion parameters, and an SNR of at least 20 (in the b_0 volume) is desired to obtain reliable estimates of DKI parameters. Constrained DKI reconstruction was shown to provide more accurate estimates compared to standard least square estimation of DKI parameters.

Chapter 6. Summary and Future Directions

There were two main goals for this dissertation. The first was to assess the value of Diffusion Kurtosis Imaging (DKI), a recently developed imaging technique, in detecting tissue microstructure change post brain injury (e.g., Traumatic Brain Injury). If DKI does prove to be valuable, then the question becomes one of understanding the performance characteristics of the technique so that it may be optimally used in clinical diagnostic imaging. So the second goal of this dissertation was to develop the necessary imaging and image reconstruction tools for practical use in the clinic, while still preserving as much information from the technique as possible. As an extension to the second goal, we also wanted to understand how DKI-derived parameters are affected by different factors: for example, different imaging schemes, reconstruction methods or data signal-to-noise ratios (SNR).

6.1 Clinical Values of DKI

In Chapter 3, we investigated the changes in water diffusion and kurtosis parameters in several white and grey matter regions, in a controlled cortical impact (CCI) injury rat model, at both the acute (2 hours) and sub-acute (7 days) stages. Our results indicated changes in standard diffusion tensor parameters, including fractional anisotropy (*FA*) and mean diffusivity (*MD*) that normalized by the sub-acute stage. However, mean kurtosis (*MK*) was significantly elevated and remained elevated at 7 days in the ipsilateral regions of the hippocampus, cortex and the external capsule. Further, at 7 days, increased *MK* was also observed in the contralateral regions, indicating a spread of injury to remote regions, while no changes were observed with *MD* and *FA*. Immunohistochemical examination demonstrates that the increase in *MK* is associated with increased reactive astrogliosis in the cortex, hippocampus, corpus callosum and external capsule. Our study suggests that DKI is sensitive to microstructural changes resulting from increased astrocytotic activity that may be missed by standard diffusion tensor imaging (DTI) parameters. Monitoring changes in *MK* allows the investigation of molecular and morphological changes *in vivo* due to reactive astrogliosis and may complement information available from standard DTI parameters. To date the use of DTI has been limited to study changes in white matter integrity following traumatic insults. The sensitivity of DKI to detect microstructural changes even in the gray matter *in vivo,* allows the extension of the technique to understand patho-morphological changes in the whole brain following a traumatic insult.

6.2 DKI Reconstruction Methods

In Chapter 4, we introduced an improved fast DKI reconstruction method (fDKI_T). The conventional way of DKI reconstruction is by fitting the diffusion and kurtosis along each diffusion direction ($D_{app}(\mathbf{g})$ and $K_{app}(\mathbf{g})$) using the nonlinear least squares method first, and then reducing them to the diffusion tensor **D** and the kurtosis tensor **W** by the linear least squares method, as a second step. This method, although intuitive, is not only time consuming (due to the nonlinear fitting), but also error prone (due to the over-fitting problem). Therefore, we proposed a tensor-based formula that fit the 21 tensor parameters directly. The tensor-based formula can further be transformed to linear equations and be solved by linear least squares fitting. fDKI_T reduces the DKI reconstruction time for a whole brain dataset to 2-3 seconds, compared to ~90 minutes using the non-linear method. This reduced reconstruction time is comparable to standard DTI reconstruction and would be strongly preferred in a clinical scenario. We further compared fDKI_T and the corresponding non-linear least squares version (NLS_T), to the conventional non-linear reconstruction method (NLS) and a previously proposed fast DKI reconstruction method (fDKI). Both whole brain analysis and regional analysis showed an improved accuracy and reduced variability in estimating DKI parameters using the tensor-based methods (fDKI_T and NLS_T). Furthermore, fDKI_T preformed comparable to the more time-consuming nonlinear fitting (NLS_T). In summary, the linear least squares fitting using a tensor-based approach should be the method of choice for faster and more efficient DKI reconstruction.

Even with the improved tensor-based reconstruction, DKI estimation is still highly susceptible to fitting errors. In order to ensure that estimated diffusion and kurtosis parameters are physically meaningful, three constraints were introduced in Chapter 5: 1. Nonnegative diffusion coefficient ($D_{app}(\mathbf{g}) \geq 0$); 2. Nonnegative kurtosis values ($K_{app}(\mathbf{g}) \geq 0$); 3. Monotonically decreasing diffusion weighted signal for increasing b-value, which translates to an upper bound for kurtosis values ($K_{app}(\mathbf{g}) \leq 3/(D_{app}(\mathbf{g}) \cdot b_{max})$). Only 0.2% of the voxels in the brain violated constraint 1 in our study, yet, as much as 7% of the brain voxels violated constraint 2, and more than 30% of the brain voxels violated constraint 3. At a cost of increased reconstruction time (~40 minutes for a whole brain dataset), constrained fitting showed improved accuracy and reduced variability in estimating DKI parameters than the unconstrained fitting. Therefore, the unconstrained linear least squares method is a good option if real-time DKI reconstruction is desired, in which case caution must be taken when physically irrelevant DKI parameter values are encountered. If time permits, constrained DKI reconstruction should always be used.

6.3 Effect of Diffusion Weighted Imaging Schemes and Signal-to-Noise Ratio (SNR) to DKI parameters

In Chapter 5, we studied how different diffusion weighting imaging schemes and image SNRs, as well as reconstruction methods, affect the accuracy and variability in DKI parameters. Number of diffusion weightings (b-values) appeared to have little effect for DKI estimation. Rather, the choice of b-values, especially the maximum b-value, determines the value of estimated kurtosis parameters. On the other hand, more diffusion directions greatly improved the kurtosis tensor estimation, especially going from a minimum of 15 diffusion directions to 30. We found the optimally efficient DKI imaging scheme to be with 30 diffusion directions and two nonzero b-values (b = 1000, 2500 s/mm^2), which requires ~7 min for a whole brain acquisition (the Opt7min scheme). An extended imaging scheme was also examined, with 45 diffusion directions and the same b-values, with a scan time of ~10 min for whole brain acquisition (the Opt10min scheme). The performance of these two optimal imaging schemes was compared to a frequently used DKI imaging scheme (the 5B30D scheme, ~17min) and a previously suggested efficient imaging scheme (the 2B30D scheme, ~7min). Between the two schemes with acquisition time of seven minutes, the Opt7min scheme performed better than 2B30D schemes in all categories (estimation accuracy and variability, as well as erroneous fitting results that violated any of the three constraints). With a 40% reduction in time compared to the 5B30D scheme, the Opt10min scheme had the least estimation variability and resulted in least erroneous fitting results among all imaging schemes. These experiments confirmed that DKI estimation benefits more from more diffusion directions than diffusion weightings.

The effect of noise to DKI estimation appeared to be mainly due to an increased chance of erroneous fitting with low SNR. Kurtosis parameters are more susceptible to noise than diffusion parameters because it is easier to violate the kurtosis value constraints. K_r and MK tend to be underestimated, while K_a is overestimated as SNR is reduced. Caution is advised when low SNR images are used for DKI (SNR < 20).

6.4 Future Directions

The DKI imaging technique is currently being applied in a new human TBI study. Patients with different levels of injury (mild, moderate, severe) are being recruited and all are undergoing MRI scans at different time points (visit 1: within 10 days post injury; visit 2: ~ 1 month; visit 3: ~ 6 months; visit 4: ~ 18 months). During each visit, their cognitive functions are also assessed through a battery of neuropsychological tests. The goal of the study is to find imaging markers that may have prognostic values. Initial findings from 22 mildly injured patients have suggested a similar trend of temporal pattern in DKI parameters in patients as our animal study in Chapter 3. Kurtosis values in thalamus and internal capsules have also shown correlations with reaction time in the cognitive tests. Eventually, we will determine whether DKI can be useful in the diagnosis of patients' clinical status, as well as long-term recovery. We also want to know whether diffusion and kurtosis parameter values at the acute stage can be predictive of patents' cognitive function recovery. At the same time, we also hope to do more animal studies to better understand the association of increased kurtosis with tissue pathological changes. It would be of great interest to see how *MK* correlates with histological findings, for example, the density of astrocytes within the injured tissue and the relationship with behavior and size of the contusion. Other tissue microstructure change may also affect kurtosis values, for example, neuronal degeneration, microglia activation, etc., and we would like to better understand how these changes may affect diffusion kurtosis.

In terms of clinical applications of DKI, there are still several challenges ahead. DKI reconstruction can be done linearly within 2-3 seconds, which is ideal for clinical applications. But more than 30% of all voxels may suffer from erroneous fitting if unconstrained. Constrained reconstruction can significantly reduce fitting error, but requires substantially increased reconstruction time (~40 min). So developing better and faster DKI reconstruction methods is still of great interest. Moreover, better visualization of kurtosis data that can more clearly illuminate individual patients' injuries is also critical to making DKI a more clinically practical tool. Clinicians typically focus on an individual patient, rather than trying to assess group trends, so individual patient analysis is of great interest. One possible route is to compare a patient’s kurtosis values to normative values (after gathering large scale normative data) and highlight the abnormal regions (e.g., more than 2 standard deviations from normal) to indicate possible injured sites.

As an extension to studies in Chapter 5, we plan to measure the test/re-test reproducibility of the diffusion and kurtosis parameters estimated from the DKI model. This will be conducted on a group of healthy normal volunteers; each will be scanned multiple times. Both inter-subject and inter-session reliability will be determined. This will provide an understanding of the baseline variability in estimated DKI parameters and may help to better interpret group comparison results between patients and normal controls.

Bibliography

Alexander AL, Lee JE, Lazar M, Field AS (2007). Diffusion tensor imaging of the brain. Neurotherapeutics. 4(3):316-29.

Alexander DC, Barker GJ (2005). Optimal imaging parameters for fiber-orientation estimation in diffusion MRI. Neuroimage. 2005; 15;27(2):357-67.

Allen NJ, Barres BA (2009). Neuroscience: Glia - more than just brain glue. Nature. 5; 457(7230): 675-7.

Anderson AW (2001). Theoretical analysis of the effects of noise on diffusion tensor imaging. Magn Reson Med. 46(6):1174-88.

Arfanakis K, Haughton VM, Carew JD, Rogers BP, Dempsey RJ, Meyerand ME (2002). Diffusion tensor MR imaging in diffuse axonal injury. AJNR Am J Neuroradiol. 23(5):794-802.

Armitage PA, Bastin ME, Marshall I, Wardlaw JM, Cannon J (1998).Diffusion anisotropy measurements in ischaemic stroke of the human brain. MAGMA. 6(1):28-36.

Assaf Y, Cohen Y (1998). Non-mono-exponential attenuation of water and N-acetyl aspartate signals due to diffusion in brain tissue. J. Magn. Reson. 131(1): 69–85.

Assaf Y, Cohen Y (2000). Assignment of the water slow-diffusing component in the central nervous system using q-space diffusion MRS: implications for fiber tract imaging. Magn Reson Med. 43: 191-199.

Barmpoutis A, Zhuo J (2011), Diffusion Kurtosis Imaging: Robust estimation from DW-MRI using homogeneous polynomials. Proceedings of IEEE international Symposium on Biomedical Imaging, pp. 262-265.

Basser PJ, Mattiello J, LeBihan D (1994). "Estimation of the effective self-diffusion tensor from the NMR spin-echo". Journal of Magnetic Resonance Series B 103 (3): 247–254.

Basser PJ, Pierpaoli C (1996). Microstructural and physiological features of tissue elucidated by quantitative-diffusion tensor MRI. J Magn Reson B 111:209-219

Basser PJ, Ozarslan E (2009). Diffusion MRI: From quantitative measurement to in vivo neuroanatomy. (Editors: Johansen-Berg H, Behrens TEJ). Elsevier Inc. ISBN: 978-0-12-374709-9. pp 3-9.

Bazarian JJ, Zhong J, Blyth B, Zhu T, Kavcic V, Peterson D (2007). Diffusion tensor imaging detects clinically important axonal damage after mild traumatic brain injury: a pilot study. J Neurotrauma. 24:1447–1459.

Bennett KM, Schmainda KM, Bennett RT, et al (2003). Characterization of continuously distributed cortical water diffusion rats with a stretched-exponential model. Magn. Reson. Med. 50(4): 727-734.

Benson RR, Meda SA, Vasudevan S, Kou Z, Govindarajan KA, Hanks RA, Millis SR, Makki M, Latif Z, Coplin W, Meythaler J, Haacke EM (2007). Global white matter analysis of diffusion tensor images is predictive of injury severity in traumatic brain injury. J Neurotrauma. 24(3):446-59.

Blumbergs PC, Scott G, Manavis J, et al (1994). Staining of amyloid precursor to study axonal damage in mild head injury. Lancet; 344:1055-1056.

Bozzali M, Falini A, Franceschi M, Cercignani M, Zuffi M, Scotti G, Comi G, Filippi M (2002). White matter damage in Alzheimer's disease assessed in vivo using diffusion tensor magnetic resonance imaging. J Neurol Neurosurg Psychiatry. 72(6):742-6.

Bulakbasi N, Kocaoglu M, Ors F, Tayfun C, Uçöz T (2003). Combination of single-voxel proton MR spectroscopy and apparent diffusion coefficient calculation in the evaluation of common brain tumors. AJNR Am J Neuroradiol. 24(2):225-33.

Carlson BC (1979). Computing elliptic integrals by duplication. Numer. Math. 33: 1-16.

Cercignani M, Bozzali M, Iannucci G, Comi G, Filippi M (2001). Magnetisation transfer ratio and mean diffusivity of normal appearing white and grey matter from patients with multiple sclerosis. J Neurol Neurosurg Psychiatry. 70(3):311-7.

Chen S, Pickard JD, Harris NG (2003). Time course of cellular pathology after controlled cortical impact injury. Exp Neurol. 182(1):87-102.

Chen Y, Swanson RA (2003). Astrocytes and brain injury. J Cereb Blood Flow Metab. 23:137–149

Cheung MM, Hui ES, Chan KC, Helpern JA, Qi L, Wu EX (2009). Does diffusion kurtosis imaging lead to better neural tissue characterization? A rodent brain maturation study. Neuroimage. 45:386-92.

Chu Z, Wilde EA, Hunter JV, et al (2009). Voxel-based analysis of diffusion tensor imaging in mild traumatic brain injury in adolescents. AJNR Am J Neuroradiol Epub

Cohen Y, Assaf Y (2002). High b-value q-sapce analyzed diffusion-weighted MRS and MRI in neuronal tissues – a technical review. NMR Biomed. 15:516-542.

Conturo TE, McKinstry RC, Akbudak E, Robinson BH (1996). Encoding of anisotropic diffusion with tetrahedral gradients: a general mathematical diffusion formalism and experimental results. Magn Reson Med. 35(3):399-412.

Cordobes F, Lobato RD, Rivas JJ, et al (1986). Post-traumatic diffuse axonal brain injury. Analysis of 78 patients studied with computed tomography. Acta Neurochirurgica. 81:27–35.

Cox, R.; Glen, D (2006). Efficient, Robust, Nonlinear, and Guaranteed Positive Definite Diffusion Tensor Estimation. International Society for Magnetic Resonance in Medicine, 14th Scientific Meeting, Seattle, Washington, p. 349

Dixon CE, Clifton GL, Lighthall JW, Yaghmai AA, Hayes RL (1991). A controlled cortical impact model of traumatic brain injury in the rat. J Neurosci Methods. 39:253-62.

Edgar JM, Griffiths IR (2009). White Matter Structure: a Microscopist's View. In Diffusion MRI-From quantitative measurements to in vivo neuroanatomy (Johansen-Berg H, Behrens TEJ eds). pp 75-103. Elsevier Inc. ISBN: 978-0-12-374709-9

Einstein A (1956). Investigations on the theory of the brownian movement. New York, NY: Dover.

Falangola MF, Jensen JH, Babb JS, Hu C, Castellanos FX, Di Martino A, Ferris SH, Helpern JA. (2008) Age-related non-Gaussian diffusion patterns in the prefrontal brain. J Magn Reson Imaging. 28:1345-50.

Farrell JA, Landman BA, Jones CK, Smith SA, Prince JL, van Zijl PC, Mori S (2007). Effects of signal-to-noise ratio on the accuracy and reproducibility of diffusion tensor imaging-derived fractional anisotropy, mean diffusivity, and principal eigenvector measurements at 1.5 T.J Magn Reson Imaging. 26(3):756-67.

Finch CE (2003). Neurons, glia, and plasticity in normal brain aging. Neurobiol Aging. 24 Suppl 1:S123-7

Gentry LR (1994). Imaging of closed head injury. Radiology. 191:1-17.

Greve MW, Zinc BJ (2009). Pathophysiology of Traumatic Brain Injury. Mout Sinai J of Med. 76:97-104.

Grossman EJ, Ge Y, Jensen JH, Babb JS, Miles L, Reaume J, Silver JM, Grossman RI, Inglese M (2011). Thalamus and cognitive impairment in Mild Traumatic Brain Injury: A Diffusional Kurtosis Imaging Study. J Neurotrauma. 2011 Jun 3. [Epub ahead of print]

Guo AC, Cummings TJ, Dash RC, Provenzale JM (2002). Lymphomas and high-grade astrocytomas: comparison of water diffusibility and histologic characteristics. Radiology. 224(1):177-83.

Hahn EL (1950). Spin Echoes. Phys. Rev. 80:580-594.

Hall ED, Sullivan PG, Gibson TR, Pavel KM, Thompson BM, Scheff SW (2005). Spatial and temporal characteristics of neurodegeneration after controlled cortical impact in mice: more than a focal brain injury. J Neurotrauma. 22(2):252-65.

Hasan KM, Parker DL, Alexander AL (2001). Comparison of gradient encoding schemes for diffusion-tensor MRI. J Magn Reson Imaging. 13(5):769-80.

Helpern JA, Adisetiyo V, Falangola MF, Hu C, Di Martino A, Williams K, Castellanos FX, Jensen JH (2011). Preliminary evidence of altered gray and white matter microstructural development in the frontal lobe of adolescents with attention-deficit hyperactivity disorder: a diffusional kurtosis imaging study. J Magn Reson Imaging. 33(1):17-23.

Hirano A, Llena JF (1995). Morphology of central nervous system axons. In: The Axon. (Waxman SG, Kocsis JD, Stys PK eds). pp. 49-67. New York Oxford: Oxford University Press.

Hui ES, Cheung MM, Qi L, Wu EX (2008).Towards better MR characterization of neural tissues using directional diffusion kurtosis analysis. Neuroimage. 2008;42:122-34.

Immonen RJ, Kharatishvili I, Niskanen JP, Gröhn H, Pitkänen A, Gröhn OH (2009). Distinct MRI pattern in lesional and perilesional area after traumatic brain injury in rat--11 months follow-up. Exp Neurol. 215:29-40.

Jansen JF, Stambuk HE, Koutcher JA, Shukla-Dave A (2010). Non-gaussian analysis of diffusion-weighted MR imaging in head and neck squamous cell carcinoma: A feasibility study. AJNR Am J Neuroradiol.31:741-8.

Jensen JH, Helpern JA, Ramani A, Lu H, Kaczynski K (2005). Diffusional kurtosis imaging: the quantification of non-gaussian water diffusion by means of magnetic resonance imaging. Magn Reson Med.53:1432-40.

Jensen JH, Helpern JA (2010). MRI quantification of non-Gaussian water diffusion by kurtosis analysis. NMR Biomed. 23(7):698-710.

Jiang Q, Qu C, Chopp M, Ding GL, Davarani SP, Helpern JA, Jensen JH, Zhang ZG, Li L, Lu M, Kaplan D, Hu J, Shen Y, Kou Z, Li Q, Wang S, Mahmood A (2011). MRI evaluation of axonal reorganization after bone marrow stromal cell treatment of traumatic brain injury. NMR Biomed. 2011 Mar 23. doi: 10.1002/nbm.1667. [Epub ahead of print]

Jones DK, Horsfield MA, Simmons A (1999). Optimal strategies for measuring diffusion in anisotropic systems by magnetic resonance imaging. Magn Reson Med. 42(3):515-25.

Jones DK (2004). The effect of gradient sampling schemes on measures derived from diffusion tensor MRI: a Monte Carlo study. Magn Reson Med. 51(4):807-15.

Karagulle Kendi AT, Lehericy S, Luciana M, Ugurbil K, Tuite P (2008). Altered diffusion in the frontal lobe in Parkinson disease. AJNR Am J Neuroradiol. 29(3):501-5. Epub 2008 Jan 17.

Kiselev VG, Il'yasov KA (2007). Is the “biexponential diffusion” biexponential. Magn Reson Med. 57(3):464–9.

Koay CG, Chang LC, Carew JD, Pierpaoli C, Basser PJ (2006). A unifying theoretical and algorithmic framework for least squares methods of estimation in diffusion tensor imaging. J Magn Reson. 182(1):115–125.

Kraus MF, Susmaras T, Caughlin BP, Walker CJ, Sweeney JA, Little DM (2007). White matter integrity and cognition in chronic traumatic brain injury: a diffusion tensor imaging study. Brain. 130(Pt 10): 2508-19.

Landman BA, Farrell JA, Jones CK, Smith SA, Prince JL, Mori S (2007). Effects of diffusion weighting schemes on the reproducibility of DTI-derived fractional anisotropy, mean diffusivity, and principal eigenvector measurements at 1.5T. Neuroimage. 36(4):1123-38.

Landman BA, Farrell JA, Huang H, Prince JL, Mori S (2008). Diffusion tensor imaging at low SNR: nonmonotonic behaviors of tensor contrasts. Magn Reson Imaging. 26(6):790-800.

Langlois JA, Rutland-Brown W, Wald MM (2006). The epidemiology and impact of traumatic brain injury: a brief overview. J Head Trauma Rehabil. 21(5):375-8.

Laird MD, Vender JR, Dhandapani KM (2008). Opposing roles for reactive astrocytes following traumatic brain injury. Neurosignals. 16(2-3):154-64.

Le Bihan D, Breton E, Lallemand D, Grenier P, Cabanis E, Laval-Jeantet M (1986). MR imaging of intravoxel incoherent motions: application to diffusion and perfusion in neurologic disorders. Radiology.161(2):401-7.

Lebel C, Walker L, Leemans A, Phillips L, Beaulieu C (2008). Microstructural maturation of the human brain from childhood to adulthood. Neuroimage. 40(3):1044-55.

Lu H, Jensen JH, Ramani A, Helpern JA (2006). Three-dimensional characterization of non-gaussian water diffusion in humans using diffusion kurtosis imaging. NMR Biomed. 19:236-47.

Maas AI, Stocchetti N, Bullock R.(2008) Moderate and severe traumatic brain injury in adults. Lancet Neurol. 7(8):728-41.

Mac Donald CL, Dikranian K, Bayly P, Holtzman D, Brody D (2007). Diffusion tensor imaging reliably detects experimental traumatic axonal injury and indicates approximate time of injury. J Neurosci. 27:11869-76.

Maier SE, Vajapeyam S, Mamata H, et al (2004). Biexponential diffusion tensor analysis of human brain diffusion data. Magn Reson Med. 51(2):321–30.

Maier SE, Mulkern RV (2008). Biexponential analysis of diffusion-related signal decay in normal human cortical and deep gray matter. Magn Reson Imaging. 26:897-904.

Mayer AR, Ling J, Mannell MV, et al. (2010). A prospective diffusion tensor imaging study in mild traumatic brain injury. Neurology. 74: 643–650.

Morell P (1984). Myelin. New York and London: Plenum Press.

Myer DJ, Gurkoff GG, Lee SM, Hovda DA, Sofroniew MV. Essential protective roles of reactive astrocytes in traumatic brain injury. Brain. 2006;129:2761-72.

Mori S (2007). Introduction to Diffusion Tensor Imaging. Elsevier Science. ISBN-10: 0444528288

Mulkern RV, Gudbjartsson H, Westin CF, et al (1999). Multicomponent apparent diffusion coefficients in human brain. NMR Biomed. 12:51–62.

Newcombe VF, Williams GB, Nortje J, Bradley PG, Harding SG, Smielewski P et al (2007). Analysis of acute traumatic axonal injury using diffusion tensor imaging. Br J Neurosurg. 21(4): 340-8.

Niendorf T, Dijkhuizen RM, Norris DG, van Lookeren Campagne, M, Nicolay K (1996). Biexponential diffusion attenuation in various states of brain tissue: implications for diffusion-weighted imaging. Magn Reson Med 1996;36:847–857.

Niogi SN, Mukherjee P, Ghajar J, Johnson C, Kolster RA, Sarkar R, Lee H, Meeker M, Zimmerman RD, Manley GT, McCandliss BD (2008). Extent of microstructural white matter injury in postconcussive syndrome correlates with impaired cognitive reaction time: a 3T diffusion tensor imaging study of mild traumatic brain injury. AJNR Am J Neuroradiol. 29(5):967-73.

Ozarslan E, Mareci TH (2003). Generalized diffusion tensor imaging and analytical relationships between diffusion tensor imaging and high angular resolution diffusion imaging. Magn. Reson. Med. 50(5):955-965.

Parizel PM, Ozsarlak O, Van Goethem JW, et al (1998). Imaging findings in diffuse axonal injury after closed head trauma. Eur Radiol. 8:960–965.

Paxinos G, Watson C (1986). The Rat Brain in stereotaxic coordinates. Academic Press Inc.

Pierpaoli C, Jezzard P, Basser PJ, Barnett A, Di Chiro G (1996). Diffusion tensor MR imaging of the human brain. Radiology. 1996; 201:637– 648.

Pfefferbaum A, Adalsteinsson E, Sullivan EV (2005). Frontal circuitry degradation marks healthy adult aging: Evidence from diffusion tensor imaging. Neuroimage. 26(3):891-9.

Poot DH, den Dekker AJ, Achten E, Verhoye M, Sijbers J (2010). Optimal experimental design for diffusion kurtosis imaging. IEEE Trans Med Imaging. 29(3):819-29.

Qi L, Wang Y, Wu EX (2008). D-eigenvalues of diffusion kurtosis tensors. Journal of Computational and Applied Mathematics. 221:150-157.

Raab P, Hattingen E, Franz K, Zanella FE, Lanfermann H (2010). Cerebral gliomas: diffusional kurtosis imaging analysis of microstructural differences. Radiology. 254:876-81.

Reese TG, Heid O, Weisskoff RM, Wedeen VJ (2003). Reduction of eddy-current-induced distortion in diffusion MRI using a twice-refocused spin echo. Magn Reson Med. 49(1):177-82.

Robertson CL, Puskar A, Hoffman GE, Murphy AZ, Saraswati M, Fiskum G (2006). Physiologic progesterone reduces mitochondrial dysfunction and hippocampal cell loss after traumatic brain injury in female rats. Exp Neurol. 197:235-43.

Schmierer K, Altmann DR, Kassim N, Kitzler H, Kerskens CM, Doege CA, Aktas O, Lünemann JD, Miller DH, Zipp F, Villringer A (2004). Progressive change in primary progressive multiple sclerosis normal-appearing white matter: a serial diffusion magnetic resonance imaging study. Mult Scler. 10(2):182-7.

Sidaros A, Engberg AW, Sidaros K, Liptrot MG, Herning M, Petersen P et al (2008). Diffusion tensor imaging during recovery from severe traumatic brain injury and relation to clinical outcome: a longitudinal study. Brain. 131(Pt 2):559-72.

Shanmuganathan K, Gullapalli RP, Mirvis SE, Roys S, Murthy P (2004). Whole-brain apparent diffusion coefficient in traumatic brain injury: correlation with Glasgow Coma Scale score. AJNR Am J Neuroradiol. 25: 539-44.

Skare S, Li T, Nordell B, Ingvar M (2000). Noise considerations in the determination of diffusion tensor anisotropy.Magn Reson Imaging. 18(6):659-69.

Shaw G (2010). New Imaging Captures the Brain’s Complexity. Neurology Now, 9-10.

Smith SM, Jenkinson M, Woolrich MW, et al (2004). Advances in functional and structural MR image analysis and implementation as FSL. NeuroImage, 23(S1):208-219.

Sofroniew MV (2009). Molecular dissection of reactive astrogliosis and glial scar formation. Trends Neurosci. 32:638–647

Sofroniew MV, Vinters HV (2010). Astrocytes: biology and pathology. Acta Neuropathol. 119(1):7-35.

Song SK, Sun SW, Ramsbottom MJ, Chang C, Russell J, Cross AH (2002). Dysmyelination revealed through MRI as increased radial (but unchanged axial) diffusion of water. Neuroimage. 17(3):1429-36.

Song, S.K., Sun, S.W., Ju, W.K., Lin, S.J., Cross, A.H., Neufeld, A.H. (2003). Diffusion tensor imaging detects and differentiates axon and myelin degeneration in mouse optic nerve after retinal ischemia. NeuroImage. 20, 1714–1722.

Sosin DM, Sniezek JE, Thurman DJ. Incidence of mild and moderate brain injury in the United States, 1991. Brain Injury 1996;10:47-54.

Stejskal EO (1965). "Use of spin echoes in a pulsed magnetic-field gradient to study anisotropic, restricted diffusion and flow". Journal of Chemical Physics 43 (10): 3597–3603.

Steyerberg EW, Mushkudiani N, Perel P, et al (2008). Predicting outcome after traumatic brain injury: development and international validation of prognostic scores based on admission characteristics. *PLoS Med.*5(8):e165.

Tabesh A, Jensen JH, Ardekani BA, Helpern JA (2011). Estimation of tensors and tensor-derived measures in diffusional kurtosis imaging. Magn Reson Med. 65(3):823-36.

Veraart J, Van Hecke W, Sijbers J (2011). Constrained maximum likelihood estimation of the diffusion kurtosis tensor using a Rician noise model. Magn Reson Med. 66(3):678-86

Terry, R.D., DeTeresa, R., Hansen, L.A.(1987). Neocortical cell counts in normal human adult aging. Ann. Neurol. 21 (6), 530–539.

Trampel R, Jensen JH, Lee RF, Kamenetskiy I, McGuinness G, Johnson G (2006). Diffusional kurtosis imaging in the lung using hyperpolarized 3He. Magn Reson Med. 56:733-7.

Thibault LE, Gennarelli TA (1990). Brain injury: an analysis of neural and neurovascular trauma in the nonhuman primate. Annu Proc Assoc Adv Automot Med. 34:337-351

Wang JJ, Lin WY, Lu CS, Weng YH, Ng SH, Wang CH, Liu HL, Hsieh RH, Wan YL, Wai YY (2011). Parkinson Disease: Diagnostic Utility of Diffusion Kurtosis Imaging. Radiology. 2011 Jul 19. [Epub ahead of print]

Wilde EA, Chu Z, Bigler ED, Hunter JV, Fearing MA, Hanten G, Newsome MR, Scheibel RS, Li X, Levin HS (2006). Diffusion tensor imaging in the corpus callosum in children after moderate to severe traumatic brain injury. J Neurotrauma. 23(10):1412-26.

Wilde EA, McCauley SR, Hunter JC, et al. (2008). Diffusion tensor imaging of acute mild traumatic brain injury in adolescents. Neurology. 70: 948-955.

Wilson JT, Wiedmann KD, Hadley DM, Condon B, Teasdale G, Brooks DN (1988). Early and late magnetic resonance imaging and neuropsychological outcome after head injury. J Neurol, Neurosurg, Psychiatry. 51:391–396.

Wu EX, Cheung MM (2010). MR diffusion kurtosis imaging for neural tissue characterization. NMR Biomed. 23(7):836-48.

Zelaya F, Flood N, Chalk JB, Wang D, Doddrell DM, Strugnell W, Benson M, Ostergaard L, Semple J, Eagle S (1999). An evaluation of the time dependence of the anisotropy of the water diffusion tensor in acute human ischemia. Magn Reson Imaging. 17(3):331-48.

Zhang J, Evans A, Hermoye L, Lee SK, Wakana S, Zhang W, Donohue P, Miller MI, Huang H, Wang X, van Zijl PC, Mori S (2007). Evidence of slow maturation of the superior longitudinal fasciculus in early childhood by diffusion tensor imaging. Neuroimage. 38(2):239-47.

Zhang Y, De Stefano N, Brady JM, and Matthews PM (2004). Advances in functional and structural MR image analysis and implementation as FSL. NeuroImage, 23(S1):208-219

Zhuo J, Simon JZ, Gullapalli R (2011). Diffusion kurtosis imaging (DKI) reconstruction – linear or non-linear. Proceedings: International Society for Magnetic Resonance in Medicine, 19th Scientific Meeting, Montreal, Quebec, Canada. pp. 4539.

Barmpoutis A, Zhuo J (2011). Diffusion Kurtosis Imaging: Rogust Estimation from DW-MRI Using Homogeneous Polynomials. IEEE International Symposium on Biomedical Imaging, 262-265

Zhuo J, Su X, Hazelton J, Mullins RJ, Simon JZ, Fiskum G, Gullapalli RP (2012), Diffusion Kurtosis as an in vivo imaging marker for reactive astrogliosis in traumatic brain injury, NeuroImage, 59(1):467-77